LBNL-41206
UC-411

ERNEST ORLANDO LAWRENCE BERKELEY NATIONAL LABORATORY

The Study of Contact, Adhesion and Friction at the Atomic Scale by Atomic Force Microscopy

Robert W. Carpick

Materials Sciences Division
Center for Advanced Materials

December 1997

Ph.D. Thesis

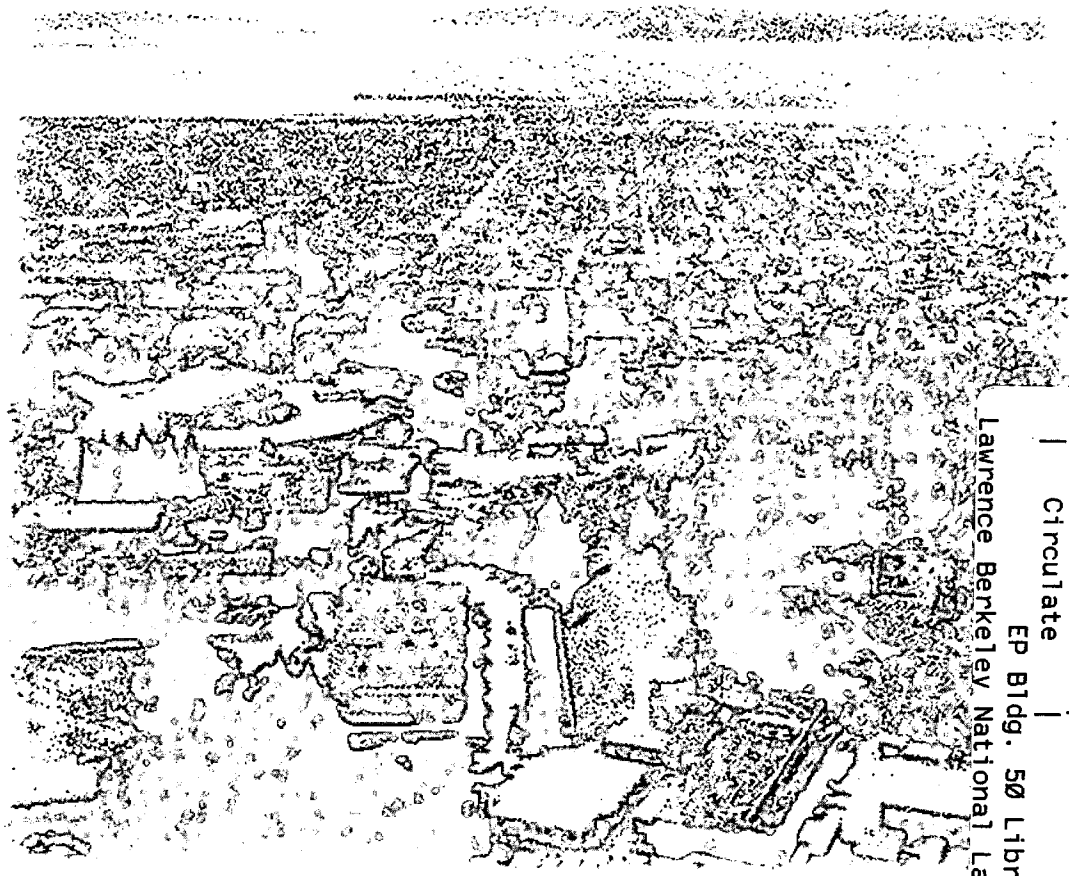

REFERENCE COPY
Does Not
Circulate
EP Bldg. 50 Library - Ref.
Lawrence Berkeley National Laboratory
LBNL-41206
Copy 1

DISCLAIMER

This document was prepared as an account of work sponsored by the United States Government. While this document is believed to contain correct information, neither the United States Government nor any agency thereof, nor the Regents of the University of California, nor any of their employees, makes any warranty, express or implied, or assumes any legal responsibility for the accuracy, completeness, or usefulness of any information, apparatus, product, or process disclosed, or represents that its use would not infringe privately owned rights. Reference herein to any specific commercial product, process, or service by its trade name, trademark, manufacturer, or otherwise, does not necessarily constitute or imply its endorsement, recommendation, or favoring by the United States Government or any agency thereof, or the Regents of the University of California. The views and opinions of authors expressed herein do not necessarily state or reflect those of the United States Government or any agency thereof or the Regents of the University of California.

LBNL-41206
UC 411

The Study of Contact, Adhesion and Friction at the Atomic Scale by Atomic Force Microscopy

Robert William Carpick
Ph.D. Thesis

Department of Physics
University of California

and

Materials Sciences Division
Lawrence Berkeley National Laboratory
University of California
Berkeley, California 94720

December 1997

This work was supported by the Director, Office of Energy Research, Office of Basic Energy Sciences, Materials Science Division, of the U.S. Department of Energy under Contract No. DE-AC03-76SF00098.

The Study of Contact, Adhesion and Friction at the Atomic Scale by Atomic Force Microscopy

by

Robert William Carpick

B.Sc. (University of Toronto) 1991
M.A. (University of California, Berkeley) 1993

A dissertation submitted in partial satisfaction of the
requirements for the degree of
Doctor of Philosophy

in

Physics

in the

GRADUATE DIVISION

of the

UNIVERSITY OF CALIFORNIA, BERKELEY

Committee in charge:
Professor Daniel S. Chemla, Chair
Dr. Miquel B. Salmeron, Co-Chair
Professor Zi Qiang Qiu
Professor Roya Maboudian

Fall 1997

The Study of Contact, Adhesion and Friction at the Atomic Scale by Atomic Force Microscopy

Copyright © 1997

by

Robert William Carpick

The U.S. Department of Energy has the right to use this document
for any purpose whatsoever including the right to reproduce
all or any part thereof

Abstract

The Study of Contact, Adhesion and Friction at the Atomic Scale
by Atomic Force Microscopy

by

Robert William Carpick

Doctor of Philosophy in Physics

University of California, Berkeley

Professor Daniel S. Chemla, Chair
Dr. Miquel B. Salmeron, Co-Chair

The physical behavior of materials in contact with one another is generally not understood at the atomic level. In an attempt to quantitatively elucidate the fundamental mechanisms involved in contact, friction, and adhesion, atomic force microscopy (AFM) studies in ultrahigh vacuum (UHV) were performed with various single crystal samples. With low applied loads, the sharp tip on the end of the AFM cantilever forms a nanometer-sized single asperity contact with a sample. Adhesion, loading, and friction forces acting between the tip and each sample were measured for these ideal contacts.

To perform the experiments, a novel UHV AFM was designed, built and characterized. The instrument is the first variable temperature UHV AFM, and allows flexibility for sample exchange, AFM measurement positioning, and surface science investigations of the sample.

Standard methods of force calibration for AFM have not yet emerged.

Furthermore, the microfabricated cantilever probes typically utilized can possess varying and uncertain physical dimensions and mechanical properties. As well, several instrumental factors of the AFM can significantly alter the force detection sensitivity. In order to calibrate AFM measurements accurately, a novel technique was developed for the calibration of lateral forces and was applied whenever possible. The relative lateral to normal force sensitivity is determined by measuring these forces on surfaces which are tilted with respect to the scanning plane. The predicted geometrical coupling of forces is compared with the output signals to determine the relative sensitivity of the instrument.

The occurrence of atomic-scale stick-slip friction forces was investigated with a number of samples. Atomic-scale stick-slip is observed to be a general phenomenon. Consideration of instrumental effects reveals that the apparent topography displayed in these measurements is in fact due to two-dimensional frictional forces. The observations raise important questions regarding interfacial commensurability, and energy dissipation.

Friction between the mica(0001) surface and various tips was measured as a function of applied load in UHV. At low applied loads, friction is observed to deviate from the macroscopic law of Amonton. Instead of being proportional to the applied load, friction is proportional to the area of contact predicted by the theory of elastic contact mechanics. Utilizing contact mechanics to calculate the contact area allows the determination of fundamental interfacial properties, namely the interfacial shear strength and the adhesion energy. The interface between mica(0001) and silicon nitride tips possessed constant interfacial shear strengths and adhesion energies. Platinum-coated tips exhibited substantially stronger adhesion and higher shear strengths initially, but both decreased progressively in proportion to the amount of tip-sample sliding contact. This behavior, due to changes of the tip structure or chemistry, indicates that friction and adhesion depend dramatically upon interfacial composition. Also, contact area depends upon the geometry of the contacting materials. Therefore, a tip-shape measurement

technique was utilized. The variation of friction with applied load was observed to depend upon the tip shape in accordance with the theory of contact mechanics. This result demonstrates that quantitative knowledge of the tip shape is crucial for extracting meaningful and reproducible results from AFM measurements.

A new instrumental technique was developed which allowed the measurement of the lateral contact stiffness. This measurement provides further insight into the properties of the tip-sample contact, as it is proportional to the contact radius and the elastic shear modulus. A comparison between measurements in ambient and vacuum on mica samples with silicon nitride tips produces dramatically contrasting friction and contact area behavior, due to the presence of a water meniscus in ambient conditions. The silicon nitride/NaCl(001) interface in UHV was observed to possess smaller contact areas, adhesion energies and shear strengths than the silicon nitride/mica interface in UHV.

A series of alkali halides were studied to compare their frictional properties. KF(001), KCl(001) and KBr(001) samples were cleaved and probed in UHV with a silicon nitride tip. The surfaces exhibit atomically flat terraces with predominantly monatomic steps. With these materials, tip-sample contact creates higher friction domains on the terraces. The structure, topography and degree of friction force contrast of these domains is material dependent. The dependence of friction upon load generally does not coincide with the behavior expected for an elastic contact. We propose that the observed domains result from surface structural changes created by low load tip-sample contact on these relatively soft materials and that this behavior is an example of the initial stages of wear at the atomic scale.

Dedicated to

my parents

Patricia Jean and Victor Carpick

Table of Contents

List of Figures vii
List of Tables x
List of Symbols (except Chapter 3) xi
List of Symbols (Chapter 3) xii
Acknowledgments xiv
1. Introduction 1
1.1 Overview: The Study of Friction 1
1.2 Atomic Force Microscopy 4
1.2.1 A Tool for Nanotribology 4
1.2.2 Instrumental Ingredients 7
1.2.3 Operation Modes 9
1.3 Outstanding Issues 11
2. Instrumentation 17
2.1 Overview 17
2.2 Design Concepts 18
2.3 Design 19
2.3.1 UHV System 19
2.3.2 Vibration Isolation 21
2.3.3 Microscope Head Arrangement 22
2.3.4 Sample Temperature Variation at the AFM Stage 25
2.4 Performance 29
2.4.1 Room Temperature 29
2.4.2 Above Room Temperature (430 K) 31
2.4.3 Below Room Temperature (110 K) 31
2.5 Summary 32
3. Force Calibration 35
3.1 Introduction 35
3.2 Optical Beam FFM 36
3.3 Spring Constant Estimates 40
3.4 Normal Force Calibration 43
3.5 Lateral Force Wedge Calibration 44
3.6 Wedge Calculations 46
3.7 Experimental Difficulties 49

3.8 Experimental Lever Calibration 50
3.9 Error Analysis 55
3.10 Summary 56
3.11 Appendix 57
3.11.1 Photodiode Response 57
3.11.2 Z Calibration and Tilt Measurement 57
3.11.3 Two Slope Calibration 58
4. Atomic-Scale Stick-Slip 62
4.1 Macroscopic Stick-Slip 62
4.2 Stick-Slip at the Atomic Scale: Overview 63
4.3 Instrumental Effects and Tip Trajectories 66
4.4 Theoretical Approaches 68
4.5 Experiments 72
4.5.1 Layered Materials 73
4.5.2 Alkali Halides 74
4.6 Conclusions and Outstanding Issues 76
5. Contact, Friction and Adhesion with Mica Substrates 80
5.1 Introduction 80
5.2 Theoretical Background - Continuum Contact Mechanics 80
5.2.1 Hertz Theory 81
5.2.2 JKR Theory 83
5.2.3 DMT Theory 85
5.2.4 The JKR-DMT Transition 85
5.2.5 The Relation to Friction 86
5.3 Experiment 88
5.3.1 Sample and Tip Preparation 88
5.3.2 Tip Shape Determination 89
5.3.3 Data Acquisition 90
5.4 Results and Discussion 91
5.4.1 Friction *vs.* Load 91
5.4.2 Variation of Shear Strength and Adhesion 98
5.5 Summary 104
5.6 Appendix - Extended JKR Model 105
6. The Lateral Stiffness Measurement Technique 110
6.1 Introduction 110

6.2 Theoretical Framework 110
6.3 Lateral Stiffness Experimental Technique 114
6.3.1 Instrumental Setup 114
6.3.2 Data Analysis 116
6.4 Lateral Stiffness Measurements 118
6.4.1 Si_3N_4 tip/Mica in Air 118
6.4.2 Si_3N_4 tip/Mica in UHV 120
6.4.3 Si_3N_4 tip/NaCl in UHV 122
6.5 Deriving an Effective Modulus from Stiffness Measurements 124
6.6 Correct Measurement of Friction 125
6.7 Summary 128
7. Frictional Properties and Surface Modification of Potassium Halide Substrates 132
7.1 Introduction 132
7.2 Properties of Potassium Halides 133
7.3 Experimental Section 135
7.4 Results 136
7.4.1 Sample Topography 136
7.4.2 Friction: Domains and Load Dependence 138
7.5 Summary 151
8. Concluding Discussion 155
8.1 Macroscopic Friction: Is There a Connection? 155
8.2 Summary of Results 161
8.3 Future Directions 164

List of Figures

Figure 1.1 Contacts viewed at different magnifications 3
Figure 1.2 AFM detection set-up and a typical approach curve 6-7
Figure 1.3 Scanning electron micrograph of a cantilever 8
Figure 2.1 Schematic of the major components of the UHV AFM chamber 19
Figure 2.2 Details of the AFM head and the sample holder 21
Figure 2.3 Schematic representation of the AFM cryogenic arrangement 25
Figure 2.4 Temperature *vs.* time of the various AFM components during cooling 27
Figure 2.5 Topographic images of NaCl in UHV 30
Figure 2.6 Topographic images of MoS_2 at ~430K 30
Figure 2.7 Topographic and lateral force images of mica at ~110K 32
Figure 3.1 Schematic of cantilever and deflection sensor for the optical beam deflection FFM 37
Figure 3.2 Scanning electron micrographs of a cantilever 42
Figure 3.3 Calculated lever response curves 42
Figure 3.4 Topographic image of the $SrTiO_3$(305) 45
Figure 3.5 Forces exerted on the surface by the AFM tip while scanning up or down a sloped surface 46
Figure 3.6 Schematic "friction loops" for flat, positively sloped and negatively sloped surfaces 48
Figure 3.7 Experimental topography and lateral deflection signals measured on the facets of the $SrTiO_3$(305) surface for each direction at a given load 52
Figure 3.8 Lateral deflection signals, friction loop width and friction loop offset measured as a function of load 53
Figure 3.9 Uncertainty in the measurement of α/β as a function of the friction coefficient μ for the wedge calibration technique 56
Figure 4.1 Lateral force image and line trace of the mica(0001) surface showing atomic-scale stick-slip forces 63
Figure 4.2 The surface structure of mica 64
Figure 4.3 Schematic of normal and longitudinal forces acting on a tip 67
Figure 4.4 Lateral and longitudinal force images, line trace, and reconstructed tip trajectory for NaCl(001) in UHV 69
Figure 4.5 A one-dimensional "atomic Tomlinson model" 71

Figure 4.6 The rocksalt surface structure 74
Figure 4.7 Lateral force image of KF(001) 75
Figure 5.1 Interaction forces (normalized per unit area) for the Hertz, JKR, and DMT models, compared to a realistic interaction..... 81
Figure 5.2 The Hertz area-load curve, and the JKR-DMT transition 82
Figure 5.3 Contact stresses (dotted lines) and contact profile (solid lines) for the Hertz, DMT, and JKR models 84
Figure 5.4 Friction *vs.* load plots, and tip profiles for a Pt-coated tip in contact with mica in UHV before and after blunting the tip..... 92-93
Figure 5.5 Friction *vs.* load measurement for a Si_3N_4 tip on mica in UHV..... 94
Figure 5.6 Series of friction *vs.* load plots for a Pt-coated tip in contact with mica in UHV showing scanning-induced reduction of adhesion energy and shear strength 99
Figure 5.7 Plot of the values of F_C and L_C measured from the measurements in Figure 5.6.....103
Figure 6.1 Elastic model of the cantilever : contact system for normal and lateral displacement.....112
Figure 6.2 Lateral force signal *vs.* lateral displacement 114
Figure 6.3 Block diagram of the experimental set-up for measuring lateral stiffness.....115
Figure 6.4 Lateral force response of the cantilever for varying lateral modulation displacement amplitudes 116
Figure 6.5 Lateral stiffness and friction *vs.* load for a Si_3N_4 tip on mica in air.....118
Figure 6.6 $F_f/k^2_{contact}$ *vs.* load for the Si_3N_4 tip on mica in air, calculated from the stiffness and friction data in Figure 6.5.....119
Figure 6.7 Lateral stiffness and friction *vs.* load data for a Si_3N_4 tip on mica in UHV...121
Figure 6.8 $F_f/k^2_{contact}$ *vs.* load for the Si_3N_4 tip on mica in UHV, calculated from the stiffness and friction data in Figure 6.7 121
Figure 6.9 Stiffness *vs.* load measurement for a Si_3N_4 tip on NaCl(001) in UHV before and after data filtering 123
Figure 6.10 Friction *vs.* load measurement for a Si_3N_4 tip on NaCl in UHV 123
Figure 6.11 $F_f/k^2_{contact}$ *vs.* load for the Si_3N_4 tip on NaCl in UHV, calculated from the friction and filtered stiffness data 123
Figure 6.12 Schematic diagram and measurements of the lateral force response at low and high loads.....127
Figure 6.13 Maximum friction, F_f, and average friction, F_{ave}, measured as a function of load for a Si_3N_4 tip on mica in air.....128

Figure 7.1 The rocksalt structure.....134
Figure 7.2 Topographic images of KCl(001) and KBr(001) showing atomically flat terraces and monatomic steps.....136
Figure 7.3 Topographic image of KCl(001) showing three screw dislocations.....137
Figure 7.4 Topographic image of a highly stepped region of KF(001) 137
Figure 7.5 Topographic and lateral force images of KBr 139
Figure 7.6 Topographic image of KBr, and series of lateral force images showing growth of friction domains.....140
Figure 7.7 Topographic and lateral force images of KCl showing a friction domain.....141
Figure 7.8 Topographic and lateral force images of KF showing friction domains.....142
Figure 7.9 Topographic and lateral force images of KBr showing friction domains located preferentially at step edges and kinks.....146
Figure 7.10 Friction *vs.* load plot for KBr within a low load regime.....150
Figure 7.11 Friction *vs.* load plot for KCl for a wide load regime.....151
Figure 8.1 Sketch of a rough surface.....157
Figure 8.2 The ratio of the integrals, *I*, plotted *vs.* non-dimensional load units on a logarithmic scale 158

List of Tables

Table 3.1 Experimental lever calibration results and estimates based on calculations..... 54
Table 4.1 Periodicity of atomic-scale stick-slip measurements 73
Table 5.1 Adhesion energy and shear strength measurements for mica in UHV..... 96
Table 5.2 Tip-sample contact size at the critical load..... 98
Table 6.1 Bulk and derived values of G^* 124
Table 7.1 Properties of potassium halide crystals.....133
Table 7.2 Properties of friction domains 142

List of Symbols (except Chapter 3)

a	contact radius
a_0	size of conventional unit cell in rocksalt structure
A	contact area
A_c	contact area at critical point (pull-off)
d	lattice spacing of rocksalt structure
E	Young's modulus
E^*	reduced Young's modulus
F_{ave}	average friction force
F_f	friction force
G	shear modulus
G^*	reduced shear modulus
h	nearest-neighbor distance in rocksalt structure
H	hardness
I	ratio of load and area integrals in GW model
$k_{contact}$	lateral contact stiffness
k_{lever}	lateral lever stiffness
k_{tot}	total lateral system stiffness
K	elastic modulus ($= \frac{4}{3}E^*$)
L	load (external loading force)
L_c	critical load (pull-off force)
R	tip radius, asperity radius
V	tip-sample interfacial potential energy
z_0	range of adhesion forces
γ	adhesion energy
δ	elastic compression of asperities
$d\varepsilon$	local strain
$d\sigma$	local stress
$\phi(z)$	asperity height probability function
$\kappa_{contact}$	normal contact stiffness
κ_{lever}	normal lever stiffness
σ	standard deviation of asperity height distribution
τ	shear strength
μ	friction coefficient
μ_T	Tabor's adhesion range parameter
ν	Poisson ratio
ψ	plasticity index
ψ_s	plasticity index in repeated sliding

List of Symbols (Chapter 3)

$1\text{-}2$	difference between left and right halves of photodiode signals
$A\text{-}B$	difference between top and bottom halves of photodiode signals
$A+B$	total photodiode signal
E	Young's modulus
$f(x),\ g(x),\ h(x)$	lever shape function for bending, twisting, buckling force
$F_f(N_\pm)$	friction force
G	shear modulus
$\mathcal{H}_{TIP}$	tip height
$k_{X,Y,Z}$	force constant for buckling, twisting, bending forces
$L,\ L_0$	lever load (Newtons, signal Volts)
$\mathcal{L}_L$	lever length
$N_\pm$	normal force (uphill, downhill)
$R_{DETECTOR}$	relative angular response of optical detection system
R_{LEVER}	relative angular response of lever
R_{tip}	tip radius
$S(\ldots)$	photodiode output signal
$T_\pm$	lever twist force (uphill, downhill)
$T,\ T_0$	lever twist force (Newtons, signal Volts)
$\mathcal{T}_L$	lever thickness
$W(L),\ W_0(L)$	friction loop width (geometrical prediction in Newtons, measured in Volts)
$W'(L),\ W_0'(L)$	slope of friction loop width *vs.* load (geometrical prediction, measured)
$W'_{101,103}(L)$	geometrical prediction for slope of friction loop width (in Newtons) *vs.* load on the (101), (103) facet
$W_0'(101,103)(L)$	measured slope of friction loop width (in Volts) *vs.* load on the (101), (103) facet
$\mathcal{W}_L$	lever arm width
X_{LASER}	laser spot position along lever's length
X_{TIP}	tip position along lever's length
$\alpha,\ \beta$	calibration factor (Newtons/Volt) for lever twisting, loading
γ	z piezo calibration correction factor

...continued

$\Gamma(y,z)$	intensity distribution of Gaussian beam
$\Delta(L)$, $\Delta_0(L)$	friction loop offset (geometrical prediction in Newtons, measured in Volts)
$\Delta'(L)$, $\Delta_0'(L)$	slope of friction loop offset *vs.* load (geometrical prediction, measured)
$\Delta'_{101,103}(L)$	geometrical prediction for slope of friction loop offset (in Newtons) *vs.* load on the (101), (103) facet
$\Delta_0'(101,103)(L)$	measured slope of friction loop offset (in Volts) *vs.* load on the (101), (103) facet
$\theta_{1,2}$	angle of (101), (103) facets with respect to (305) plane
$\theta_{101,103}$	experimental angle of (101), (103) facets with respect to the scanning plane projected onto the y-direction
$\Theta(x)$	angular deflection of lever due to twisting (lateral) force
$\mu_{101,103}$	friction coefficient on (101), (103) facet
ψ	macroscopic tilt angle of the sample with respect to the scanning plane projected onto the y-z plane
ν	Poisson ratio
$\Delta\omega$	angular half-width of optical field distribution

Acknowledgments

This thesis is the end result of a productive, enjoyable association with Dr. Miquel Salmeron. His undying optimism and continual encouragement both inspired and prodded me to reach this point. It was always a great pleasure to be a part of the remarkable research group he has put together. I am grateful for the support of my faculty sponsor, Prof. Daniel Chemla, whose help, especially at key times like my qualifying exam, was indispensable.

Dr. Frank Ogletree was also like an advisor to me. I am thankful for his encyclopedic knowledge, which he was always willing to patiently share. I would like to particularly acknowledge his contribution to our understanding of calibration issues and atomic-scale stick-slip phenomenon which is discussed herein.

I was assisted, inspired and challenged by many other members and associates of the Salmeron group, especially Prof. Heather Galloway, Prof. Scott Perry, Dr. Jim Dunphy, Dr. Alex Yoon, Dr. Anna Lio, Dr. Jun Hu, Prof. Xu Dong Xiao, Prof. James Batteas, Prof. Philippe Sautet, Dr. Stefan Behler, Dr. Peter Frantz, Dr. Alex Artsyukhovich, Mark Rose, Nikos Jaeger, Winnie Ling, David Schleef, Dr. Hendrik Bluhm, Dr. François Rieutord, Dr. Lei Xu, Dr. John Jensen, Monica Luna, and Dr. Marius Enachescu. I am particularly indebted to Dr. Qing Dai and Dr. Rudiger Völlmer, from whom I first learned the tricks of the UHV AFM trade. The results of this thesis were produced by the instrument which they primarily designed and built. Prof. Nicolas Agraït was a particularly inspiring friend and co-worker who was an integral part of the first exciting results that came out of these experiments. I thank Prof. K.L. Johnson who took an interest in this work, which was an honor and inspiration for me.

I do not want to imagine what it would have been like to attempt this feat without the outstanding professional support of our group administrative assistant, Mae Lum, and

the director of student services for the Department of Physics, Anne Takizawa. Eric Braeland and his team in the Department of Chemistry's machine shop, Alan Lyon in the vacuum coating lab, and Andrew Mei in the ceramic shop did great work for me, often on short notice.

My immediate and extended family gave me a great deal of encouragement and support throughout my graduate work. The musical inspiration of Dr. Sandra Soderlund provided a relaxing and enjoyable escape that was sorely needed. Finally, I would like to thank the many friends who kept me going even on the darkest days: Emily, Olivia, Mimi, Anthony, Steve, Arif, Stephanie, Carsey, Elizabeth, Saam, Mark, Joey, Ken, GAR, Charlie, Tatiana, Andrea, and Dahlia, and everyone else. Thanks to all!

I must acknowledge the financial support of the Natural Sciences and Engineering Research Council of Canada. This work was supported by the Director, Office of Energy Research, Basic Energy Sciences, Materials Division of the U.S. Department of Energy under contract number DE-AC03-76SF00098.

1. Introduction

1.1 Overview: The Study of Friction

Perhaps no physical phenomena is more common yet less understood than friction. We encounter and rely upon its effects every day of our lives - from the act of walking to the operation of machine parts. Economically, too, friction and related behavior have an impact: for industrialized nations, energetic and mechanical losses due to friction and wear are estimated to total 5 - 10% of their gross national products[1], a substantial portion of which could realistically be recouped with knowledge gained from research[2].

The study of friction and the related phenomena of adhesion, wear and lubrication from a macroscopic and practical perspective is known as *tribology* and while this term was coined in the 1960's, these ideas have been pursued for centuries[3].

The earliest known records of scientific experiments on friction come from Leonardo da Vinci (1452-1519)[3]. After conducting numerous experiments with sliding blocks, rolling weights and other items, the Renaissance master came to two important conclusions:

1. *"Friction produces double the amount of effort if the weight be doubled."*

2. *"The friction made by the same weight will be of equal resistance at the beginning of the movement although the contact may be of different breadths or lengths."*

In other words, the friction force resisting sliding was proportional to the load (normal force), and independent of the apparent area of contact between the sliding body and the surface. da Vinci noted the second observation with some surprise.

Amonton (1663-1705) confirmed these observations some two centuries later in 1699 with further experiments, from which came Amonton's Law of Friction:

$$F_f = \mu \cdot L \tag{1.1}$$

which states that the friction force F_f is proportional to the applied load L. The constant of proportionality, μ, is called the *coefficient of friction* and is a property of the pair of contacting materials. Nearly a century later in 1785, experiments by Coulomb (1736-1806) distinguished between friction during sticking and sliding. He observed that the coefficient of kinetic friction, μ_k, was generally smaller than the coefficient of static friction, μ_s. He also observed that μ was generally independent of sliding velocity. Coulomb also expressed surprise at the lack of dependence upon the apparent contact area. This comprises most of the physics that an undergraduate student will learn about friction. One can see that research in this field started off at a rather slow pace.

Research this century has mostly been performed in the domain of engineering because of the obvious practical importance of tribological issues for a wide range of industrial and indeed, societal applications. For example, the lifetime and efficiency of a car engine, the optimization of engine additives, the operation of car brakes, and the reliability of tires all involve many different tribological problems.

The main conclusion of this engineering work in fact confirms da Vinci's, Amonton's and Coulomb's observations: for a wide range of materials and conditions, friction between a pair of surfaces is proportional to load, independent of the apparent area of contact, and only weakly dependent on the relative sliding velocity. The lack of dependence upon the area of contact arises from the fact that the roughness of surfaces at the micrometer scale and below causes the real area of contact to be much smaller than the apparent area of contact. The true contact between the materials is comprised of a number of contacting asperities, or protrusions[4,5] (Figure 1.1). The linear or nearly-linear dependence of friction upon load is a result of the complicated and nearly random geometry of these asperities[4,5], and other complex phenomena at the interface including adhesion-induced deformation[6] and plowing of the surface asperities by each other and by wear particles[7]. While these observations are important, they fail to explain the behavior at the

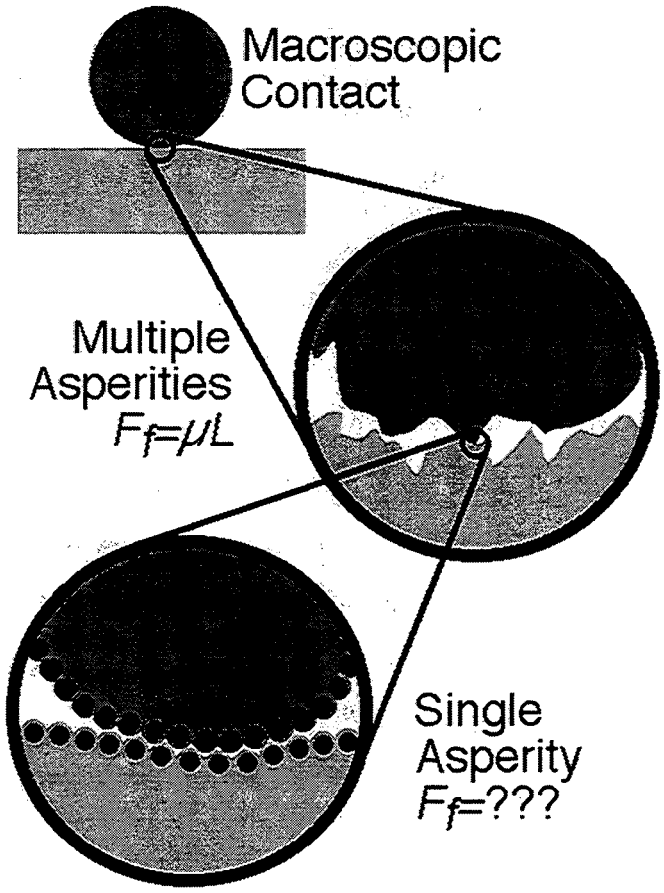

Figure 1.1 A macroscopic contact that appears conforming and continuous is usually composed of multiple contact points between many microasperities. The frictional behavior of such a contact follows Amonton's Law. The friction law for a single asperity contact is not known. The contact between an AFM tip and a sample is in fact a single asperity of atomic dimensions, whose properties can be studied.

atomic scale, and cannot be used for predictive analysis. In other words, the friction coefficient, μ, cannot be predicted for a given pair of untested materials.

Thus, despite generations of work by scientists and engineers[2,6,8-11], a fundamental understanding of frictional processes has eluded us (although a great number of practical successes have occurred). This is essentially because the buried interface between materials in sliding contact is inherently difficult to access by most surface science techniques. Furthermore, an exact understanding of the origin of friction necessitates exploring these interfaces with atomic resolution - a challenging experimental requirement.

Along with a desire to understand the macroscopic processes at a deeper level, novel problems have appeared which demand knowledge at the nanometer scale. The advent of small devices, triggered in part by the tremendous development of silicon microfabrication techniques[12], has brought tribological problems to small length scales. For example, the whole technology of information storage as exemplified by the case of

computer hard disks with coatings and lubricants that protect the stored information, with dimensions that are measured in nanometers[13]. Micrometer-sized actuators, sensors and motors are other examples of novel technology requiring such knowledge for performance optimization[14].

These problems are beginning to be addressed by the recent development of several experimental techniques[15,16]. Instruments such as the surface forces apparatus (SFA) [17-19], the quartz-crystal microbalance (QCM)[20-22], the atomic force microscope (AFM)[23,24] and others[25] are extending tribological investigations to atomic length and time scales. Furthermore, advances in computational power and theoretical techniques are now making sophisticated atomistic models and simulations feasible[26]. The emerging field of *nanotribology* attempts to use these techniques to establish an atomic-scale understanding of interactions between contacting surfaces in relative motion[9,11,16,27-30].

By using these techniques to address the questions outlined above, the knowledge gained could be used in combination with the highly developed fields of chemical engineering, materials processing/synthesis, and engineering design to produce machines and devices with optimal tribological performance. However, this panacea is far from realization. Not only does the atomic-scale knowledge remain to be discovered, but then the gap between this atomic-scale understanding and macroscopic application will need to be bridged. This is no small task and is beyond the scope of this thesis. However, we will return to this issue in our concluding discussion.

1.2 Atomic Force Microscopy

1.2.1 A Tool for Nanotribology

The atomic force microscope is an important instrument in the field of nanotribology, as it is capable of measuring interaction forces between tip and surface atoms at the atomic scale. These forces can reveal information about surface topography, lattice symmetry, adhesion, friction, elasticity, and wear with unprecedented spatial resolution. The AFM was invented by Binnig, Quate and Gerber in 1986[24]. In a typical

AFM setup, a small sharp tip (with a radius typically between 10-100 nm) is attached to the end of a compliant cantilever (Figure 1.2(a)). The tip is brought into close proximity with a sample. Forces acting between the AFM tip and the sample will result in deflections of the cantilever (Figure 1.2(b)). The cantilever bends vertically (*i.e.,* toward or away from the sample) in response to attractive and/or repulsive forces acting on the tip. The deflection of the cantilever from its equilibrium position is proportional to the normal load applied to the tip by the cantilever. The initial operation mode of the AFM measured the vertical topography of a surface by maintaining a constant repulsive contact force between tip and sample during scanning, akin to a simple record stylus. The deflection of the AFM cantilever was detected by positioning the tip of a scanning tunneling microscope (STM) above the cantilever. However, since its inception, a myriad of new operation modes and detection schemes have been developed which can measure, often simultaneously, various sample (and even tip) properties. Furthermore, the AFM tip-sample contact can in fact be a single asperity contact of nanometer dimensions (see Figure 1.1). Thus, for the first time, one can examine the atomic-scale properties of a well-defined interface.

Perhaps the most notable extension so far of AFM capabilities was the realization that lateral forces between the tip and sample could also be measured. Referring to Figure 1.2(b), we see that lateral forces result in a twisting of the cantilever from its equilibrium position. Usually described as friction force microscopy (FFM), the first experiments which attempted to measure such lateral forces were carried out by Mate *et al*[23]. Using a tungsten tip on a graphite surface in air, the authors observed lateral (frictional) forces that varied with the atomic lattice periodicity of the sample. It was thus recognized that the atomic-scale origins of friction and related phenomena could be probed with this technique.

(a)

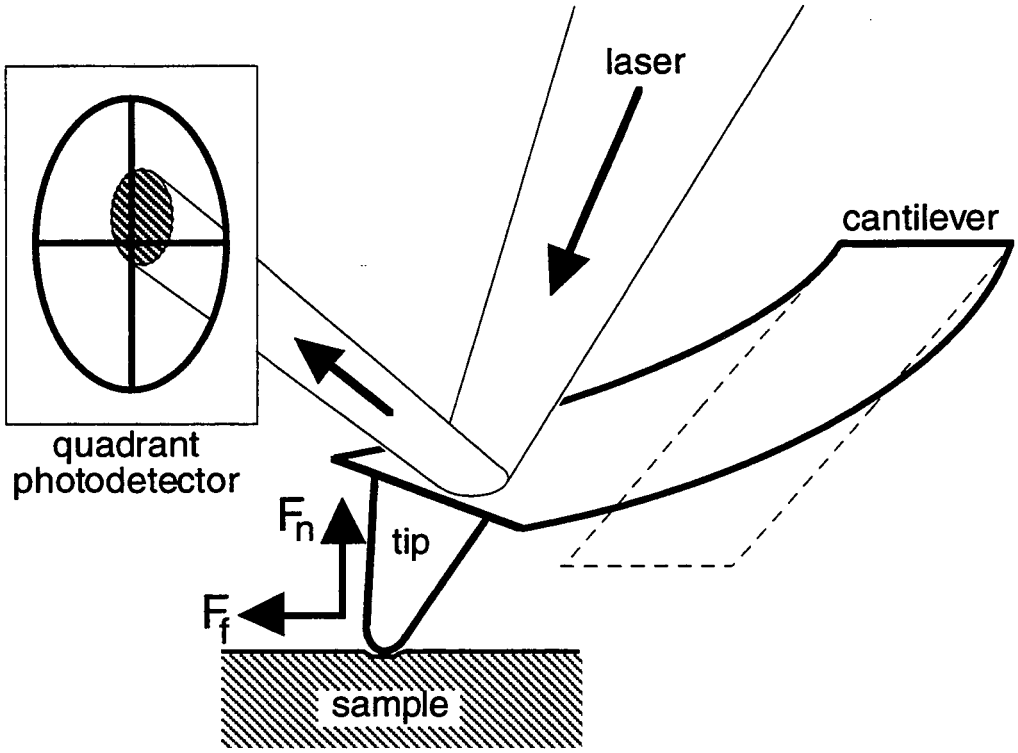
laser
cantilever
quadrant
photodetector
F_n
tip
F_f
sample

(b)

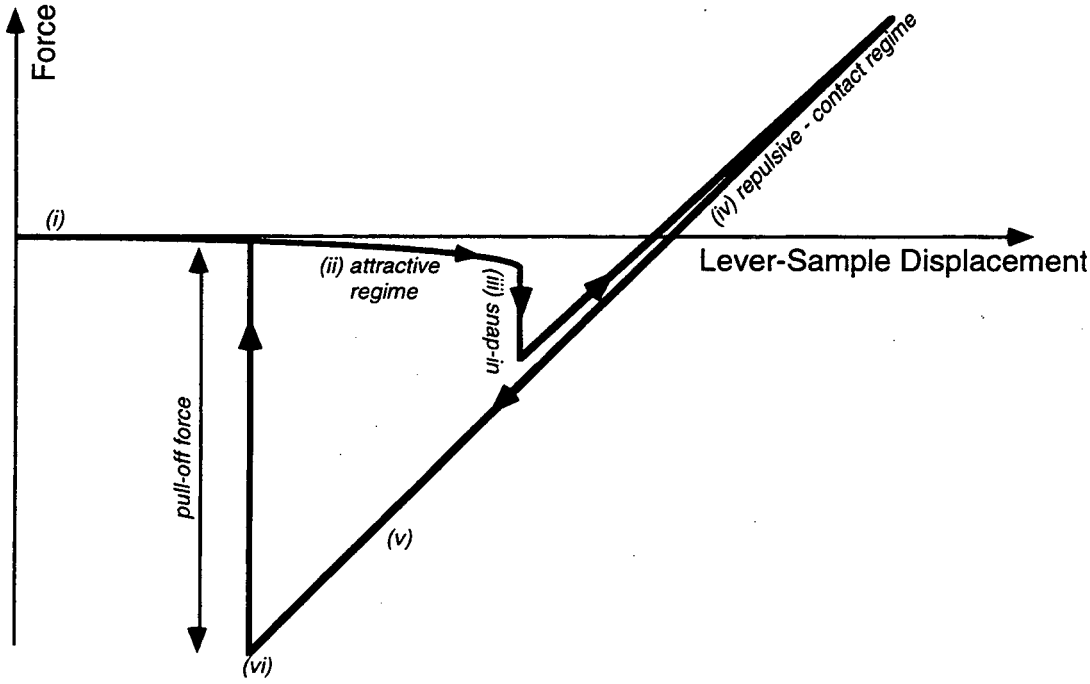
Force
(i)
(ii) attractive
regime
(iii) snap-in
(iv) repulsive - contact regime
Lever-Sample Displacement
pull-off force
(v)
(vi)

Figure 1.2 (previous page) (a) Diagram of the AFM set-up for the optical beam deflection method. The tip is in contact with a sample surface. A laser beam is focused on the back of the cantilever and reflects into a four-quadrant photodetector. Normal forces deflect the cantilever up or down, lateral forces twist the cantilever left and right. These deflections are simultaneously and independently measured by monitoring the deflection of the reflected laser beam. (b) An "approach curve" or "force-distance" curve displays the vertical cantilever bending *vs.* lever-sample displacement. This displacement is measured between the sample and the rigidly-held rear end of the cantilever (as opposed to the front end with the tip which will bend in response to interaction forces). (i) The lever and sample are initially far apart and no forces act. (ii) As the lever is brought close to the sample, the tip senses attractive forces which cause the end of the lever to bend downward, thus signifying a negative (attractive) force. (iii) The attractive force gradient exceeds the spring constant of the lever at this point, and this instability causes the tip to snap into contact with the sample. (iv) The lever-sample displacement can continue to be reduced. Since this tip is in repulsive contact with the sample, the front end of the lever is pushed further and further upward. The force corresponds to the externally applied load. (v) The motion is reversed. Adhesion between the tip and sample maintains the contact although there is now a negative (tensile) load. (vi) Finally the tensile load overcomes the adhesion or pull-off force and the tip snaps out of contact with the sample.

1.2.2 Instrumental Ingredients

As mentioned previously, the force F between the tip and sample surface is sensed by the bending of a compliant cantilever, and the deflection of this cantilever Δz is measured by some sort of deflection sensing scheme. The deflections are small compared to the cantilever dimensions then the response is linear and the force is then calculated from Hooke's law:

$$F = k \cdot \Delta z. \tag{1.2}$$

Forces are measured over a range of points on the sample surface by rastering the tip over the sample using piezoelectric tubes, described in more detail in Chapter 2. The time scale of the measurements is limited by the mechanical stability of the apparatus and is typically in the microsecond to millisecond regime. Therefore, AFM is best suited to examine tribological processes with timescales that are similar or longer.

The most commonly used cantilevers are microfabricated cantilevers made of silicon and silicon nitride which are commercially available (Figure 1.3). They are fabricated with a variety of force constants (anywhere from 0.01 to 100 N/m), high resonance frequencies, and with very small yet reasonably durable integrated tips[31-34]. These levers can be coated with films to allow experiments with various tip materials[35]. Other cantilevers, such as wires with chemically etched tips[23], parallel leaf-spring assemblies with diamond tips[36], and tips held by double cross-hair force sensors[37] are also in use and allow further choice of tip materials.

To measure both normal and lateral deflections simultaneously, the optical beam deflection method[38-40] has proven to be the simplest to implement and is currently in use by all commercially available instruments and several custom designs[41,42]. In this scheme, a laser beam is reflected from the back of the cantilever into a position-sensitive quadrant photodetector (Figure 1.2(a)). The difference between the signals from the upper and lower halves of the detector is proportional to the vertical deflection of the cantilever, and

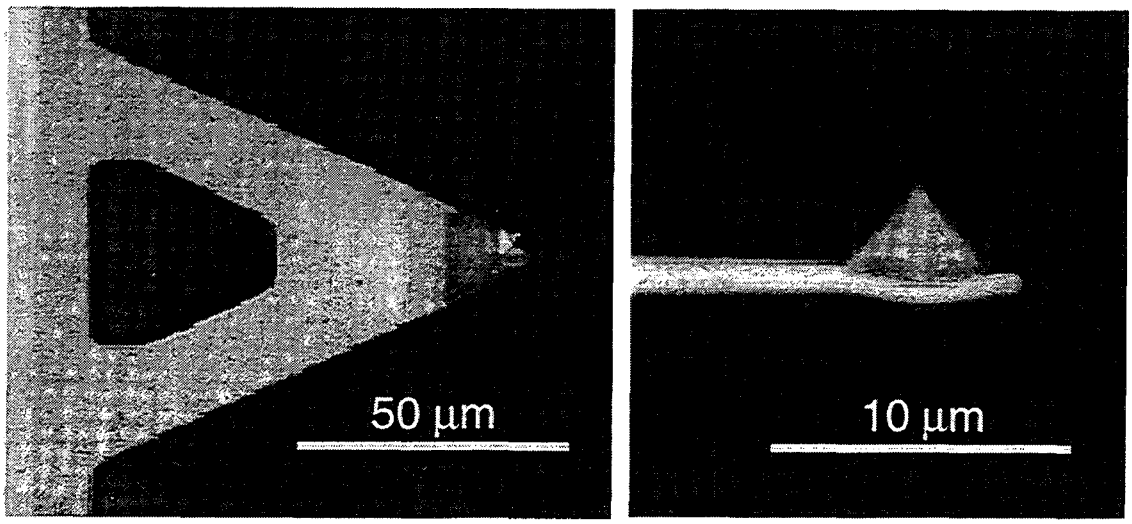

Figure 1.3 Scanning electron micrograph of a commonly used commercial V-shape silicon nitride cantilever. At left, a bottom view. The pyramidal tip at the end of the cantilever points toward the viewer. At right, a close-up side view of the tip. The cantilever thickness is nominally 0.6 μm.

the difference between the left and right halves is proportional to the lateral deflection. The method in fact measures the angles by which the cantilever is bent by applied forces, which for small angles is linearly proportional to the tip deflections. Other deflection sensing schemes can be utilized, such as fiber optic interferometry[43-45] and piezoresistive detection[46,47]. A force detection sensitivity of 10^{-10} N or better can be achieved. AFM measurements can be performed in a variety of environments: ambient air, controlled atmosphere, liquids[48], or ultrahigh vacuum (UHV)[38,49-51]. AFM is certainly the most versatile tool for nanotribology in terms of operating environment.

1.2.3 Operation Modes

There are different regimes in which forces can be measured with AFM. Figure 1.2(b) depicts in detail the normal force typically experienced by the tip as it is brought toward a sample surface. Two force regimes can be distinguished: the "attractive regime", where interaction forces (van der Waals, electrostatic, *etc.*) attract the tip to the sample but actual mechanical contact does not occur, and then the "repulsive" or "contact regime", where the outer electronic configuration of tip and sample atoms provide electrostatic and Pauli repulsive forces. On approach, these two regimes are separated by a snap-in instability which occurs when the attractive force gradient exceeds the spring constant of the cantilever. Interfacial surface forces between the tip and sample lead to adhesion during contact.

Surface topography is measured by enabling a feedback circuit to maintain a constant normal force by varying the relative vertical displacement as the tip is rastered across the sample. Such constant force images can be obtained in either the attractive or repulsive regimes. Several other methods such as AC modulation techniques can be used to image in the attractive regime, including a new "force modulation" technique[52] which has been demonstrated to achieve true atomic resolution on surfaces, but these techniques will not be discussed here as they are not directly employed for nanotribological applications.

The amount of force required to pull the tip out of contact with the sample is called the *pull-off force* or *adhesion force* and is measured directly by acquiring an *approach curve* like the one shown in Figure 1.2(b). SFA and AFM experiments have observed that the adhesion force varies with chemical identity of the interface[53,54]. Obviously, exploring the origins of this force is of interest and will be discussed in detail in forthcoming chapters.

The lateral twisting of the cantilever can be measured simultaneously with topography and often features that are not necessarily topographically distinct can show contrast in the lateral force signal due to different friction characteristics[54,55]. This suggests that friction imaging can have some degree of material or chemical sensitivity. Lateral force images often display atomic-scale stick-slip behavior with the periodicity of the atomic lattice of the sample[56]. This phenomenon will be discussed in detail in Chapter 4. The lateral force can be measured over a range of applied loads, and in fact examining the dependence of friction upon load reveals important information about the tip-sample contact and is examined in Chapters 5 and 6.

The response of the sample to a small, modulated force is dependent upon the local sample elastic properties. Normal force modulation[57-59] can thus be used to locally investigate the Young's modulus of the sample. However, the tip-sample contact area can also be probed by such a technique. In this thesis, a novel modulation technique using lateral forces for this purpose is described in Chapter 6.

In many ways, AFM techniques for quantitative, fundamental nanotribology are only in a nascent stage; certain key issues such as force calibration, tip characterization, and the effects of the experimental environment, are not fully resolved or standardized. Therefore, a substantial portion of this thesis is devoted to discussing and resolving some of these issues.

1.3 Outstanding Issues

Now that the capabilities of AFM have been briefly described, we need to consider what questions in nanotribology can be specifically addressed with AFM. By design, these will be very basic, fundamental questions. At the most fundamental level, friction, adhesion and wear need to be understood in terms of chemical bonding and of the elementary processes that are involved in the excitation and dissipation of energy modes. Several mechanisms have been proposed that we shall enumerate briefly here. One is due to coupling to the substrate (and tip) electron density that causes a drag force, similar to that causing an increase of resistance by the presence of surfaces in thin films[60-64]. The electronic time scales of these processes renders them extremely challenging for study with AFM. The QCM, which responds to dissipation in the nanosecond regime, is well suited to the examination of this mechanism.

Another mechanism is the excitation of surface phonon modes in atomic stick-slip events. Delocalization of the excited phonons by coupling to other phonon modes through anharmonic effects and transport of the energy away from the excited volume leads to efficient energy dissipation[65]. While AFM is too slow to observe dynamic phonon effects, it can sensitively measure the forces and distortions that lead to sudden energy dissipation events due to elastic relaxations. This will be discussed further in Chapter 4.

At high applied forces, wear processes leading to rupture of many atomic bonds, and displacement and creation of dislocations and debris particles, are important and are part of the wide topic of plastic deformation of materials. AFM is capable of producing this damage, and then imaging the after-effects. However, isolating the individual atomic motions that took place in such a process is very challenging. Measurements such as this were not the main emphasis of this thesis.

Recent theoretical and experimental results suggest another wear mechanism that might be playing an important role in energy dissipation, where the extent of the damage is restricted to the creation of point defects near the surface by rupture of bonds due to the

applied forces. Damage at this level is easily overlooked since, as we will discuss in Chapters 4 and 5, true atomic resolution is not usually achieved in contact AFM. Careful measurements are required to elucidate this mechanism, and a possible observation of such effects is reported in Chapter 7.

The next level of complexity in our understanding includes questions such as the nature of the relative motion between the two contacting bodies: is it continuous (smooth sliding) or discontinuous (stick-slip)? How does friction depend upon the actual area of contact between a pair of materials? Are friction and adhesion related? The results presented in this thesis, specifically Chapters 4, 5 and 6, address these questions for a few model systems.

Further questions involving lubrication are also extremely important. What is the behavior of lubricant molecules at an interface? How are they compressed and displaced during loading and shear? How does their behavior depend upon their molecular structure and chemical identity? AFM is also capable of addressing these questions, but investigations involving lubricant molecules were not a topic of this thesis.

Chapter 1 References

[1] H. P. Jost, Wear **136,** 1 (1990).

[2] I. M. Hutchings, *Tribology* (CRC Press, Boca Raton, 1992).

[3] D. Dowson, *History of Tribology* (Longman, London, 1979).

[4] J. A. Greenwood and J. B. P. Williamson, Proc. Roy. Soc. Lond. A **295,** 300 (1966).

[5] J. A. Greenwood, in *Fundamentals of Friction*, edited by I. L. Singer and H. M. Pollock (Kluwer, Dordrecht, 1992), p. 37.

[6] F. P. Bowden and D. Tabor, *Friction and Lubrication of Solids: Part I* (Oxford University Press, 1950).

[7] D. E. Kim and N. P. Suh, Wear **149,** 199 (1991).

[8] F. P. Bowden and D. Tabor, *Friction and Lubrication of Solids: Part II* (Oxford University Press, 1964).

[9] *Fundamentals of Friction: Macroscopic and Microscopic Processes*, edited by I. L. Singer and H. M. Pollock (Kluwer, Dordrecht, 1992).

[10] B. Bhushan, *Handbook of Micro/Nanotribology* (Chemical Rubber, Boca Rotan, 1995).

[11] Langmuir **12,** 4481 (1996).

[12] R. T. Howe, R. S. Muller, K. J. Gabriel, and W. S. N. Trimmer, IEEE Spectrum **27,** 29 (1990).

[13] E. Grochowski and R. F. Hoyt, IEEE Trans. Mag. **32,** 1850 (1995).

[14] R. Maboudian and R. T. Howe, J. Vac. Sci. Technol. B **15,** 1 (1997).

[15] I. L. Singer, J. Vac. Sci. Technol. A **12,** 2605 (1994).

[16] J. Krim, Sci. Am. **275,** 74 (1996).

[17] D. Tabor and R. H. S. Winterton, Proc. Roy. Soc. Lond. A **312,** 435 (1969).

[18] J. N. Israelachvili and D. Tabor, Proc. Roy. Soc. Lond. A **331,** 19 (1972).

[19] J. N. Israelachvili, P. M. McGuiggan, and M. L. Gee, Wear **136,** 65 (1990).

[20] J. Krim, E. T. Watts, and J. Digel, J. Vac. Sci. Technol. A **8,** 3417 (1990).

[21] E. T. Watts, J. Krim, and A. Widom, Phys. Rev. B **41,** 3466 (1990).

[22] J. Krim, D. H. Solina, and R. Chiarello, Phys. Rev. Lett. **66,** 181 (1991).

[23] C. M. Mate, G. M. McClelland, R. Erlandsson, and S. Chiang, Phys. Rev. Lett. **59,** 1942 (1987).

[24] G. Binnig, C. F. Quate, and C. Gerber, Phys. Rev. Lett. **56,** 930 (1986).

[25] N. Agraït, G. Rubio, and S. Vieira, Phys. Rev. Lett. **74,** 3995 (1994).

[26] J. A. Harrison and D. W. Brenner, in *Handbook of Micro/Nanotribology*, edited by B. Bhushan (CRC Press, Boca Raton, 1995), p. 397.

[27] B. Bhushan, J. N. Israelachvili, and U. Landman, Nature **374,** 607 (1995).

[28] J. Krim, Comm. Cond. Matt. Phys. **17,** 263 (1995).

[29] *Physics of Sliding Friction*, edited by B. N. J. Persson and E. Tosatti (Kluwer, Dordrecht, 1996).

[30] R. W. Carpick and M. Salmeron, Chem. Rev. **97,** 1163 (1997).

[31] Park Scientific Instruments Inc., Sunnyvale CA, USA.

[32] Digital Instruments Inc., Santa Barbara CA, USA.

[33] Nanosensors GmbH, Aidlingen, Germany.

[34] Olympus Optical Company, Japan.

[35] NT-MDT Inc., Moscow, Russia.

[36] C.-J. Lu, Z. Jiang, D. B. Bogy, and T. Miyamoto, Trans. ASME J. Tribology **117,** 244 (1995).

[37] M. Enachescu, S. A. Smallwood, R. J. Lad, and W. N. Unertl, (in preparation).

[38] G. Meyer and N. M. Amer, Appl. Phys. Lett. **56,** 2100 (1990).

[39] S. Alexander, L. Hellemans, O. Marti, J. Schneir, V. Elings, P. K. Hansma, M. Longmire, and J. Gurley, J. Appl. Phys. **65,** 164 (1989).

[40] O. Marti, J. Colchero, and J. Mlynek, Nanotechnology **1,** 141 (1991).

[41] W. F. Kolbe, D. F. Ogletree, and M. B. Salmeron, Ultramicroscopy **42-44B,** 1113 (1992).

[42] Q. Dai, R. Vollmer, R. W. Carpick, D. F. Ogletree, and M. Salmeron, Rev. Sci. Instrum. **66,** 5266 (1995).

[43] Y. Martin, C. C. Williams, and H. K. Wickramasinghe, J. Appl. Phys. **61,** 4723 (1987).

[44] D. Rugar, H. J. Mamin, and P. Güthner, Appl. Phys. Lett. **55,** 2588 (1989).

[45] C. Schonenberger and S. F. Alvarado, Rev. Sci. Instrum. **60,** 3131 (1989).

[46] M. Tortonese, R. C. Barrett, and C. F. Quate, Appl. Phys. Lett. **62,** 834 (1993).

[47] R. Linnemann, T. Gotszalk, I. W. Rangelow, P. Dumania, and E. Oesterschulze, J. Vac. Sci. Technol. B **14,** 856 (1996).

[48] O. Marti, B. Drake, and P. K. Hansma, Appl. Phys. Lett. **51,** 484 (1987).

[49] G. J. Germann, S. R. Cohen, G. Neubauer, G. M. McClelland, H. Seki, and D. Coulman, J. Appl. Phys. **73,** 163 (1993).

[50] L. Howald, E. Meyer, R. Lüthi, H. Haefke, R. Overney, H. Rudin, and H.-J. Güntherodt, Appl. Phys. Lett. **63,** 117 (1993).

[51] M. Kageshima, H. Yamada, K. Nakayama, H. Sakama, A. Kawau, T. Fujii, and M. Suzuki, J. Vac. Sci. Technol. B **11,** 1987 (1993).

[52] F. J. Giessibl, Science **267,** 68 (1995).

[53] J. N. Israelachvili, in *Fundamentals of Friction*, edited by I. L. Singer and H. M. Pollock (Kluwer, Dordrecht, 1992), p. 351.

[54] C. D. Frisbie, L. F. Rozsnyai, A. Noy, M. S. Wrighton, and C. M. Lieber, Science **265,** 2071 (1994).

[55] R. M. Overney, E. Meyer, J. Frommer, D. Brodbeck, R. Lüthi, L. Howald, H.-J. Güntherodt, M. Fujihara, H. Takano, and Y. Gotoh, Nature **359,** 133 (1992).

[56] S. Morita, S. Fujisawa, and Y. Sugawara, Surf. Sci. Rep. **23,** 3 (1996).

[57] P. Maivald, H. J. Butt, S. A. C. Gould, C. B. Prater, B. Drake, J. A. Gurley, V. B. Elings, and P. K. Hansma, Nanotechnology **2,** 103 (1991).

[58] M. Radmacher, R. W. Tillmann, M. Fritz, and H. E. Gaub, Science **257,** 1900 (1992).

[59] R. M. Overney, H. Takano, and M. Fujihira, Europhys. Lett. **26,** 443 (1994).

[60] C. Daly and J. Krim, Surf. Sci. **368,** 49 (1996).

[61] B. N. J. Persson, Comm. Cond. Matt. Phys. **17,** 281 (1995).

[62] J. B. Sokoloff, Phys. Rev. B **52,** 5318 (1995).

[63] B. N. J. Persson and A. I. Volokitin, J. Chem. Phys. **103,** 8679 (1995).

[64] B. N. J. Persson and A. Nitzan, Surf. Sci. **367,** 261 (1996).

[65] J. B. Sokoloff, Wear **167,** 59 (1993).

2. Instrumentation

2.1 Overview

All of the results presented in this thesis were acquired with a home-built AFM[1]. Therefore, the design of this microscope is described in detail in this chapter. To date, the majority of commercial and custom atomic force microscopes operate in air or liquid. However this limits the range of materials that can be studied. In addition, true surface and tip cleanliness is nearly impossible to obtain in air. This is important, for example, because frictional forces crucially depend upon the experimental environment. Liquid films condensed around the tip from ambient vapor can act as a lubricant between the tip and sample, causing friction and adhesive forces to vary with changes in humidity[2]. It is also necessary to isolate the effects of contamination, which can also significantly affect friction. The ideal conditions for fundamental nanotribological studies at the atomic level can only be achieved in ultra-high vacuum (UHV). Therefore, an AFM which operates in UHV was designed and built. The design and construction was primarily executed by Dr. Q. Dai and Dr. R. Völlmer, with performance testing and subsequent changes made by the author.

The design allows sample temperature variation from 100 - 450 K. The microscope head is capable of coarse x-y positioning over millimeter distances so that AFM images can be taken virtually anywhere upon a macroscopic sample. The optical beam deflection scheme is used for detection, allowing simultaneous normal and lateral force measurements. The sample can be transferred from the AFM stage to a Low Energy Electron Diffraction (LEED) / Auger Electron Spectrometer (AES) stage for surface analysis. The performance of this instrument is illustrated with measurements of NaCl, MoS_2 and mica surfaces in UHV.

2.2 Design Concepts

The force detection scheme used for this instrument is the optical deflection method, developed by Meyer *et al.*[3] and Alexander *et al.*[4], and improved by Marti *et al*[5]. In this detection scheme, as described in Chapter 1, a laser beam is reflected off the rear side of the cantilever and its deflection is measured by a position-sensing photodiode detector. Normal forces which bend the cantilever vertically, and lateral forces which twist the lever, can be independently and simultaneously measured.

The few UHV AFM systems developed so far operate only at room temperature[6-12] or additionally liquid helium temperature[13]. Imaging at different temperatures is not easily performed with these other designs. To allow variable temperature operation, the "walker" style microscope design is used, which is based upon the STM design by Fröhn *et al*[14]. The key feature of the design is that the sample does not need to be attached to any piezoelectric elements for scanning or positioning. Instead, all the AFM components are mounted on a separate base supported by three piezoelectric tubes (piezos for short). The light source (an optical fiber and lens), the cantilever, and the photodiode are scanned above the sample while the sample remains fixed. The sample then resides in a sample holder that can then be easily clamped to a thermal reservoir for heating and cooling. This also allows easy sample transferring, as well as a large range of coarse tip positioning.

With the beam deflection scheme, the optical alignment is critical. Since vacuum operation restricts mechanical access to an experiment, and since the fine positioning required for optical alignment would considerably complicate the apparatus, the design requires the optical alignment to be performed *ex-situ*. Optical misalignment after pumping and baking the chamber is small for Si levers[15,16], as well as levers that have been coated with films on both sides of the lever[17]. Thermal drift of these levers during sample heating and cooling (to be discussed further in section 2.3.4) is also reasonably small. This system has an airlock to allow microscope access for occasional lever replacement or optical re-alignment without venting the whole UHV chamber.

2.3 Design

2.3.1 UHV System

A schematic drawing of the UHV AFM system is shown in Figure 2.1. The chamber consists of two stages: the AFM stage and the surface preparation/analysis stage. The sample is mounted in a sample holder which is transferred between these two stages with a wobble stick. The sample holder functions as an approach ramp for the microscope and will be described in section 2.3.3. A load lock is included so that samples can be transferred in and out of the chamber without breaking vacuum. As well, an air-lock

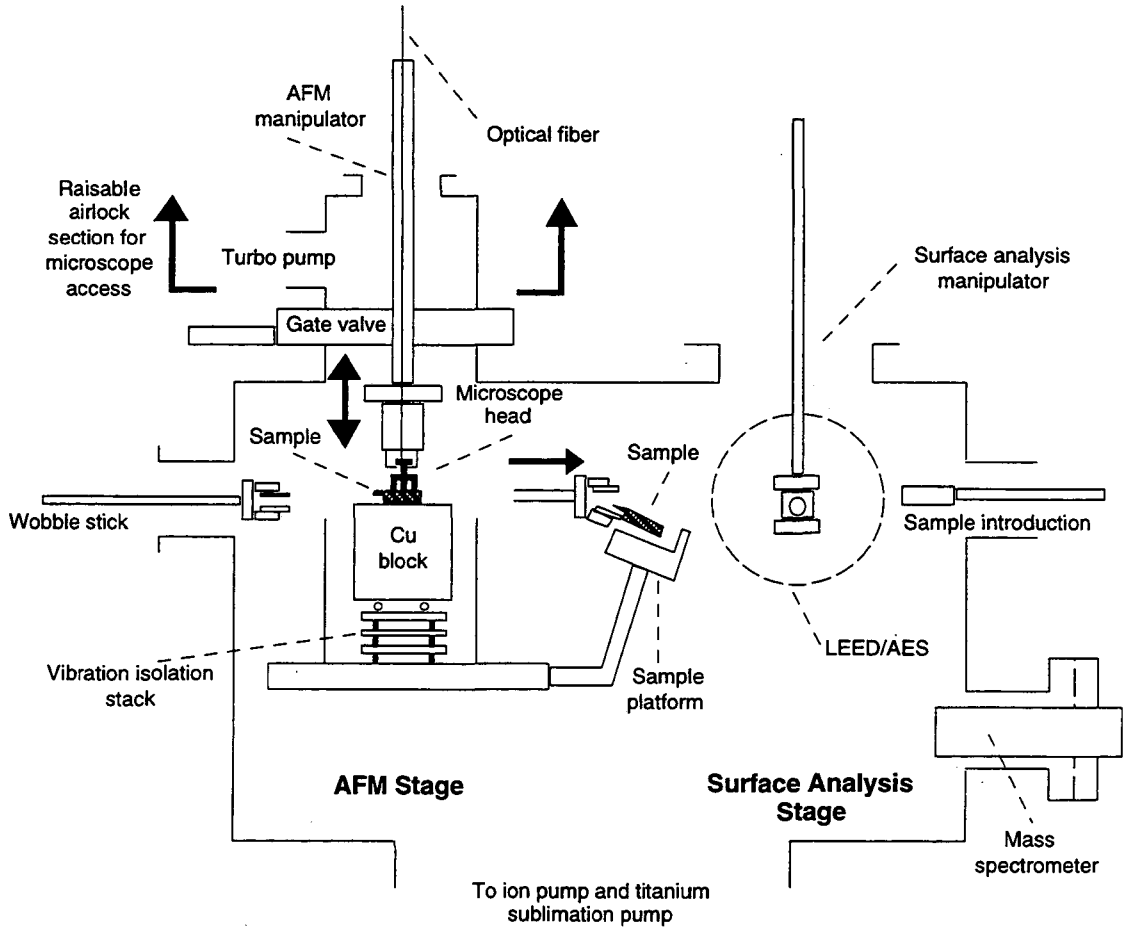

Figure 2.1 Schematic representation of the major components of the UHV AFM chamber.

system above the AFM stage allows the microscope to be taken to air, to change cantilevers for instance, without breaking vacuum inside the main chamber. The chamber is bolted onto a steel frame supported by a vibration isolation system described in the next section.

The surface preparation/analysis stage is equipped with conventional surface analysis techniques: an ion sputtering gun for sample cleaning, a quadrapole mass spectrometer, a gas doser and a LEED/AES optics system for sample preparation and characterization. The sample holder is clamped onto a manipulator. The sample is cooled by a liquid nitrogen cold finger which is connected to the manipulator with copper braids. The sample can also be heated through radiation and electron beam bombardment (for high temperature) by using a tungsten filament mounted within the sample manipulator. As such, the sample can be cooled below 100K or heated above 2000K.

The microscope head is attached to a second manipulator that can raise or lower the microscope over the AFM stage. The microscope can be raised through a gate valve to a five-way cross airlock system to allow microscope access (for cantilever replacement, *etc.*) without breaking vacuum in the rest of the chamber. When the microscope is lowered onto the AFM sample stage, its three piezo legs stand upon the sample holder, completely decoupled from the AFM manipulator (Figure 2.2).

The sample holder is held with two Be-Cu foil springs so that it can be inserted and removed with the wobble stick, yet is sufficiently clamped to prevent vibrations and ensure good thermal contact. Cooling and heating of the sample will be discussed in section 2.3.4.

The wobble stick is able to pick up and drop off a second sample from a platform located between the AFM and surface analysis stages. This allows a reference sample to be available at all times for immediate calibration and comparison.

The wobble stick can also be used to cleave samples *in-situ*. A modified sample holder can be used which has a slot for a guided knife-edge. Rapidly jerking the wobble stick forward while pushing on the knife-edge provides enough force to cleave samples.

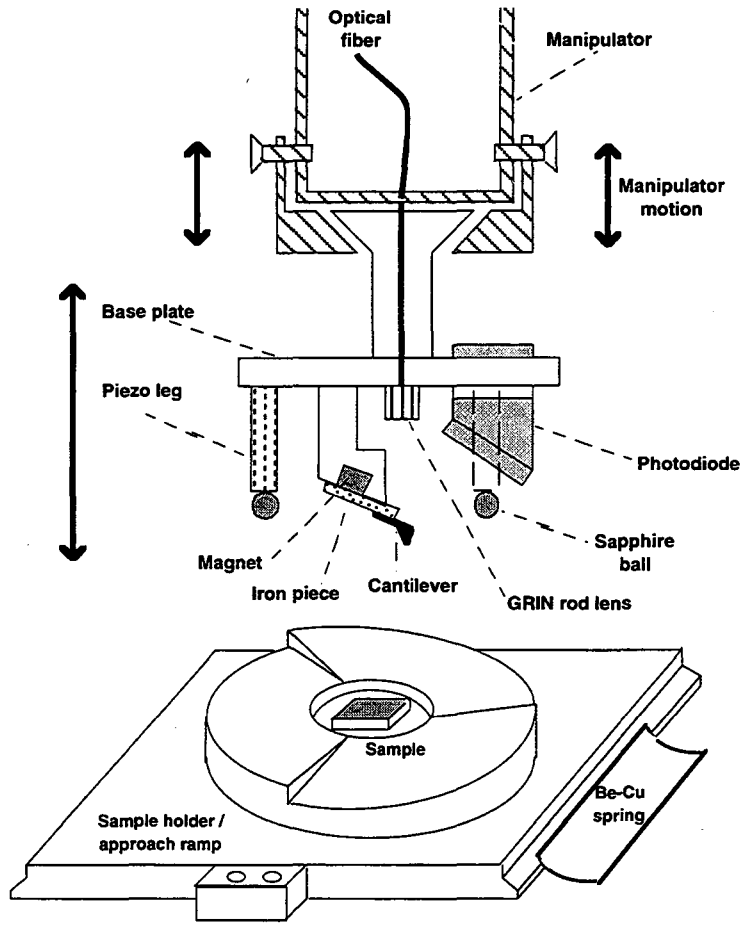

Figure 2.2 Details of the AFM head and the sample holder. Electrical connections to the photodiode and piezo sectors are made with 0.003" diameter wires running from a pin assembly above the manipulator (not shown).

2.3.2 Vibration Isolation

Isolating the experiment from vibrations is critical for any scanning probe microscope. Typical vibrations in buildings induced by elevators, stepping on the floor, or motion of the entire building itself can have amplitudes of a few micrometers. Without an effective damping system, this would eliminate the possibility of measuring surface features with sub-Ångstrom sensitivity. To accomplish this, the entire UHV chamber is

mounted on a rigid steel frame which is supported by four "air legs"; laminar flow vibration supports[18] with pressure regulators that maintain the chamber at a constant height. These elaborate shock absorbers effectively damp vibrations above 1 Hz. However, there is an important stability requirement for the effective operation of the vibration isolation system: the distance from the frame to the center of mass of the supported body must be less than half of the separation between the air legs. Unfortunately, the height of the chamber necessary to accommodate the airlock puts this distance slightly greater than preferred. Without any correction, the vibration isolation system is no longer in a critically damped regime and the chamber and frame will oscillate back and forth. A re-distribution of the weight by placing lead bricks on the chamber frame generally alleviates this problem. To allow the airlock to be opened for microscope access, a rope is attached to the top of the chamber and runs through a pulley above, which is attached to the laboratory wall. It is important to adjust the tension in this rope carefully as it also increases the chamber stability, although if too tight it will provide a means for building vibrations to be coupled into the system. Once properly set up, the system generally remains stable indefinitely. Some additional vibration isolation is provided inside the chamber itself by a stack of steel plates separated by rubber feet which supports the sample stage. This is described with the rest of the sample stage in section 2.3.4.

2.3.3 Microscope Head Arrangement

The microscope head and sample holder / approach ramp are depicted in Figure 2.2. The microscope consists of a base plate, three piezo tubes for approaching and scanning, an optical fiber and lens, the cantilever, and a four-quadrant photodiode detector.

The piezos are a lead-zirconate-titanate (PZT) ceramic material[19]. PZT materials possess a perovskite crystal structure. The non-centrosymmetric unit cell has a dipole moment which means that an applied electric field will distort the crystal. Specifically, the material will elongate in the direction of the applied field, and to preserve volume will contract perpendicular to the field. A response of 10 nm/Volt is typical for these materials.

Therefore, low-noise electronics can apply fields in the milliVolt range which distort the piezos with sub-Ångstrom position. Tube structures with sectored electrodes allow x, y, and z distortions and are described in detail by Chen[20].

The nickel-plated aluminum base plate which holds all the head components is 1.25" in diameter and 0.1" thick. The mass of the microscope head should be kept as small as possible to maximize its stiffness. Since laser diodes require massive heat sinks during operation, it is not practical to attach a laser diode to the microscope head directly. Furthermore, bakeout compatibility would involve non-trivial design considerations for the laser diode. Therefore, light is brought from an external laser diode into the chamber with a single-mode optical fiber. The single-mode fiber completely filters higher modes that are typically emitted from laser diodes. A well-directed, circular beam profile thus emerges from the fiber end. The fiber enters the chamber through a small hole drilled through a flange, sealed with Torr-Seal[21]. Outgassing from the fiber jacket in UHV is found to be negligible as the chamber base pressure is routinely below 5×10^{-10} Torr and has been as low as 7×10^{-11} Torr. Index-matching epoxy[22] attaches the fiber to a graded-index (GRIN) rod lens[23] on the microscope head which focuses the laser beam onto the cantilever.

Commercially available microfabricated cantilevers are used. For mounting in the microscope, they are attached to a small iron piece with low vapor pressure epoxy. The iron piece is in turn held onto the microscope by a magnet embedded in a central post as shown in Figure 2.2. This allows easy positioning of the cantilever by moving the iron piece with tweezers so that the incident laser beam will be properly positioned at the center of the back end of the lever. The position of the laser spot is checked with an optical microscope, as well as by examining the pattern of diffracted light beneath the cantilever. An asymmetric diffraction pattern indicates that the spot is not aligned on the center of the end of the lever. The end of the center post which contains the magnet is machined at a 22.5° angle, thus the reflected beam is at a 45° angle to the vertical incoming beam. With a

Si or Si_3N_4 cantilever coated with gold, roughly 70% of the incident light is reflected off the back of the lever and collected by the photodiode.

The photodiode is mounted on an aluminum block, which is held onto the base plate with a thin Be-Cu foil which functions as a spring clamp. The position of the photodiode can be adjusted by hand by moving the aluminum block within its slot until the beam is centered on the detector. The aluminum block is machined at a 45° angle so that the reflected laser beam will be normally incident.

The microscope is supported by three piezo tubes 0.5" long, 120° apart on a 1.0" diameter. The tubes are used for offsetting, scanning and inertial approaching/translating of the microscope. These tubes are 0.125" in diameter and have a wall thickness of 0.02". Sapphire balls are attached to their ends with low vapor pressure epoxy. The sapphire balls facilitate the inertial motion. The resulting static friction force is small enough to allow the sapphire balls to slide across the ramp when the voltage applied to the piezo is suddenly changed, but large enough to hold the microscope steady while it is being scanned.

The coarse approach mechanism is identical to that of the walker type STM[14]. A saw-tooth voltage wave deforms the piezo legs in such a way that the microscope rotates through inertial motion. The sample holder, as illustrated in Figure 2.2, consists of three sloped ramps machined along the circumference. Therefore, as the microscope head rotates, it slowly descends, approaching the tip gradually toward the sample. The electronics halts the approach when the lever makes contact with the sample. The microscope can be retracted by applying a reversed voltage signal so that the microscope will rotate up the ramp. Inertial motion can also translate the microscope laterally across the ramp to image different parts of the sample. The sample holder can accommodate a sample as large as 8×8 mm^2, all of which is accessible to the microscope. The lowest eigenfrequency of the microscope head is ~1.1 kHz. This limits the scan rate to less than 100 scan lines/second. The microscope is controlled by analog control electrons[24] interfaced to a PC. The photocurrents from the four segments of the quadrant detector are

preamplified separately. These signals are then fed into a home-made analog electronics system which performs the summation and subtraction of the four signals.

2.3.4 Sample Temperature Variation at the AFM Stage

The method for sample temperature variation was designed primarily for AFM operation at or below room temperature, and so the method and results of sample cooling will be described in detail next. However, the AFM can also be operated with the sample temperature substantially above room temperature.

The cryogenic arrangement is depicted in Figure 2.3. The sample holder is mounted on top of a massive (~3 kg) copper block, where it is held in place with two Be-

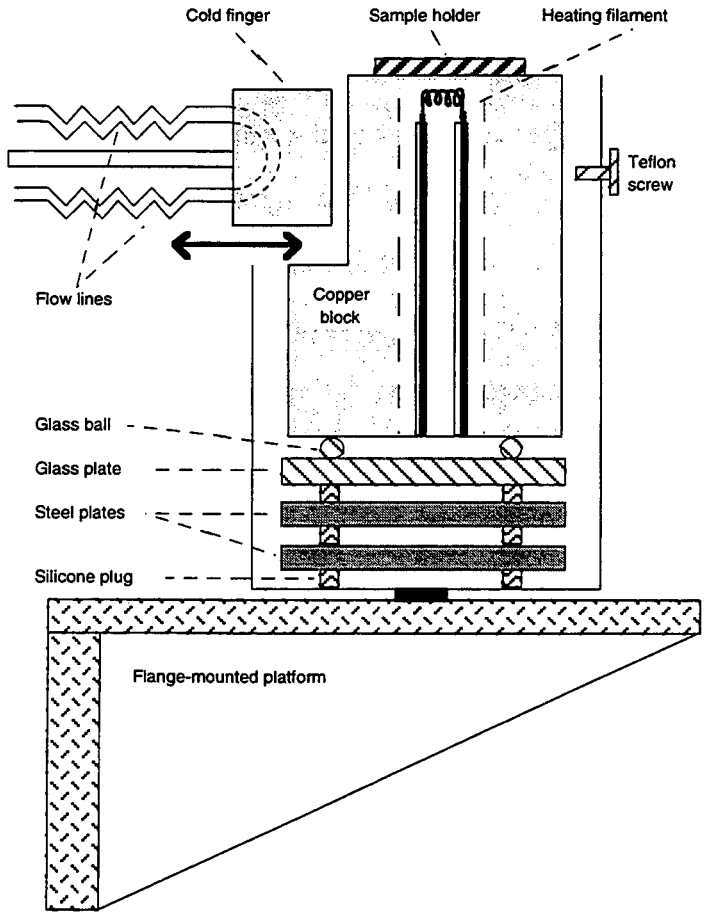

Figure 2.3 Schematic representation of the AFM cryogenic arrangement.

Cu spring clamps. Under the copper block there is a stack which consists of two stainless steel plates with silicone rubber plugs in between for additional vibration damping. The silicone[25] is preferable to Viton or other materials because it retains its elastic character over a large temperature range, and outgasses minimally. To reduce heat transfer, a glass plate separates the stack and copper block which sits on three 0.1" diameter glass balls. The copper block makes no other contact with the chamber.

The sample can be cooled with liquid nitrogen through a retractable cold finger to below 90K. The cold finger is made of copper, with dimensions approximately 2" × 1" × 1", mounted on a linear motion feedthrough. Two thin-wall stainless steel tubes are welded onto the cold finger, connected via a hole machined through it to allow liquid nitrogen flow. The sample is cooled by flowing liquid nitrogen through the cold finger while it is pressed against the copper block. The cold finger is retracted once the sample has reached the desired temperature, leaving the sample and copper block mechanically isolated. The copper block is surrounded by a stainless steel cylinder which holds three Teflon set screws, set very close to but not in contact with the copper block to prevent the block from tipping over when the cold finger is pressed against it.

To determine the temperatures of the various components of the AFM stage, thermocouples were attached to the copper block, the sample ramp, a mica sample, and four different parts of the microscope itself. The underside of the mica sample was attached to the sample holder with a thin layer of epoxy.

Figure 2.4 shows the various temperatures plotted *vs.* time. The first section of the plot is taken with the cold finger in contact with the copper block while liquid nitrogen is flowed through it. The block cools down from room temperature to 90K in less than 2 hours. At point A, the cold finger is retracted and the copper block is now thermally and mechanically isolated. The components slowly warm up due to radiative heat transfer with their room temperature surroundings. The initial warming up rate of the sample is ~3 K/hour. This is slow enough to allow several images to be acquired within a one degree

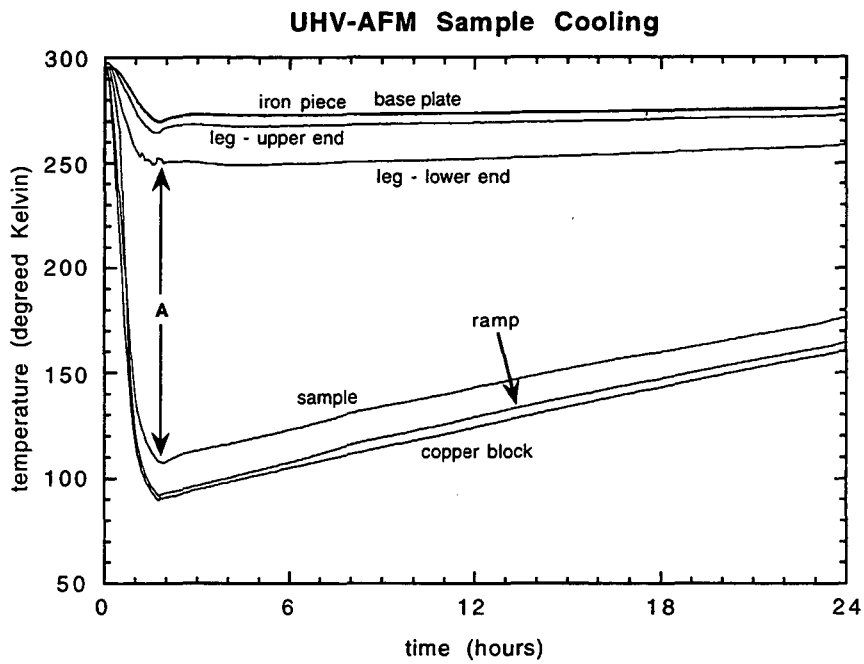

Figure 2.4 Temperature *vs.* time of the various AFM components during cooling. A mica sample is mounted in the sample holder. At t = 0, the cold finger is put in contact with the copper block. At point A (t = 1.5 hours), the cold finger is retracted. The sample has cooled to ~105 K at this point. The initial warm-up rate is ~3 K/hour. Various parts of the microscope itself do not cool substantially. The iron piece and microscope base plate curves nearly overlap.

Kelvin range. In this case, the sample remained ~15 degrees warmer than the sample holder due to the poor thermal conductivity of mica along its c-axis. However the removable sample holder is only ~2 degrees warmer than the copper block, showing that the spring clamping creates a good thermal contact between the sample holder and the copper block.

Piezo sensitivities vary significantly with temperature, so it is important to check if the piezos cool substantially. The lower end of the piezo leg only cools to ~250K with the copper block at 90K, indicating good thermal isolation. The upper part of the leg reaches a minimum temperature of ~265K. This demonstrates that over the entire low temperature

range of the experiment, the piezo gain will not change dramatically. Indeed, by comparing atomic lattice resolution images taken at room temperature and at low temperature, the change in gain due to piezo cooling can be measured. With T_{block}=100 K, the gain was only about 10% smaller than at room temperature. This is consistent with the sensitivity decrease expected for these piezos at approximately 250-260K, according to the manufacturer's data. The microscope base and the iron piece which holds the cantilever both reach a minimum temperature of ~270K. Therefore, the microscope is well insulated from the ramp.

All scanning probe microscopes are subject to some thermal drift. The thermal drift was measured with a Si cantilever[15] on a cooled mica sample in two separate experiments. Roughly 60 minutes after the cold finger was retracted, with T_{block}=100K, thermal drift rates of typically 0.05 - 0.1 nm/s in the lateral direction and 0.02 - 0.04 nm/s in the z-direction with the lever in contact with the sample were measured. These drift rates are not dramatically worse than the typical corresponding rates at 297K: 0.03 nm/s or less laterally, 0.01 nm/s or less in z. Overall, the drift at 100K is smooth and small enough so that it may be easily corrected for with image processing functions provided by the system software. The drift rates decrease with time as the microscope equilibrates further and the copper block warms up. Furthermore the lever will cool somewhat due to radiative exchange with the sample and conduction through the microscope body. With the lever out of contact, its equilibrium position drifted upward by approximately 100 nm compared to room temperature. Despite this change in alignment, the laser spot has not deviated far enough from the center of the photodiode to impair deflection sensing. This upward bending of the lever is most likely due to the thin gold coating on the top of the lever which will undergo more thermal contraction upon cooling than the lever material itself (Si or Si_3N_4)[26]. The lever relaxes to its original position when the AFM stage returns to room temperature.

Sample heating is conducted as follows. To temporarily heat the sample, a tungsten filament is mounted inside the copper block. The filament is buried inside ceramic shielding to reduce heat loss to the copper block, but is placed as close as possible to the sample to improve the heating efficiency. The sample can be heated to ~500K by radiation alone, or about 1500K through electron beam bombardment. However, to provide enough stability to acquire AFM images, the sample needs to be in thermal equilibrium with the copper block so that the rate of temperature decrease will be slow. To achieve this, the entire copper block can be heated; analogous to the cooling method, heated air can be flowed through the retractable copper block while it is in contact with the sample block to raise its temperature. Alternately, one can take advantage of the elevated temperature of the copper block after baking the chamber. An image acquired in this fashion is presented in the next section.

2.4 Performance

All of the following results were acquired in UHV with a chamber pressure of 4×10^{-10} Torr or less using Si cantilevers[15] with a nominal spring constant of 1.1 N/m.

2.4.1 Room Temperature

Figure 2.5 shows AFM images taken on a NaCl(001) surface, cleaved and imaged in UHV at room temperature in the topographic mode. Figure 2.5(a) is an atomic lattice resolution image of the NaCl(001) surface. The observed lattice spacing on NaCl(001) is 0.40 ± 0.01 nm, matching well with surface lattice constant, *i.e.* the nearest neighbor spacing between identical ionic species of 0.398 nm. Figure 2.5(b) is a large scale (1.2×1.2 μm) image, in which monatomic steps are clearly resolved.

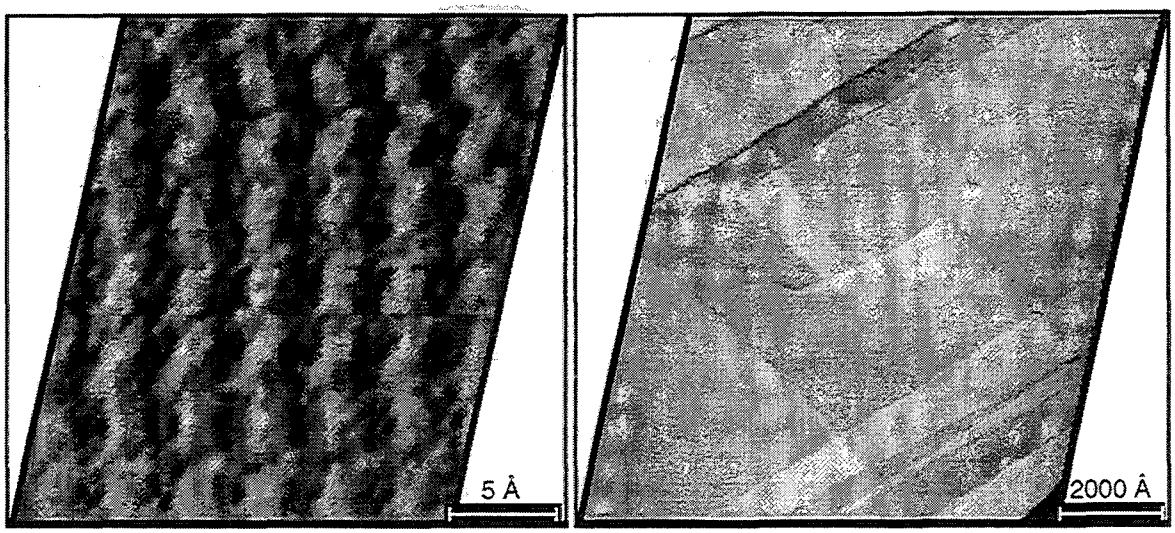

(a) (b)

Figure 2.5 Topographic images of NaCl(001) in UHV. (a) 3×3 nm^2 image showing atomic lattice resolution in UHV. The image was taken with an external loading force of ~5 nN. (b) Large scale (1.2×1.2 μm^2) topographic image showing monatomica steps. The non-rectangularity of the images is from a correction imposed to account for an asymmetric de-polarization of the piezo tubes that was later improved.

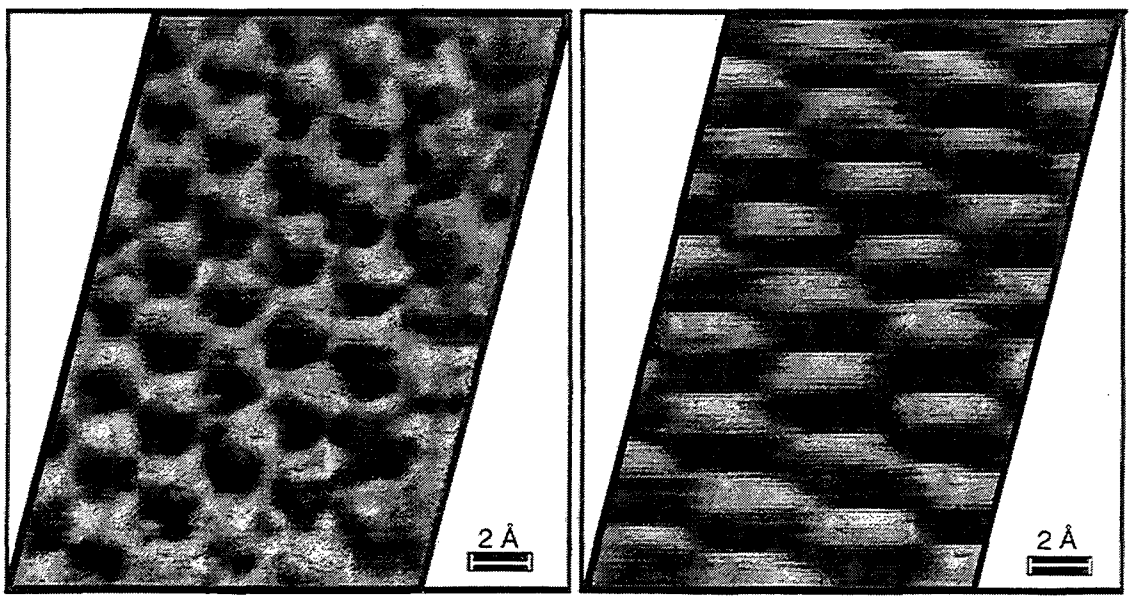

(a) (b)

Figure 2.6 Topographic images of MoS_2 at ~430K. (a) The usual lattice spacing (0.31 nm) is observed with weak contrast. (b) A greatly distorted lattice and enhanced contrast (~8 times greater) is temporarily imaged, possibly due to a sliding flake between the tip and surface. The non-rectangularity is explained in Figure 2.5.

2.4.2 Above Room Temperature (430 K)

Figure 2.6 shows a MoS_2 crystal cleaved in UHV and imaged at ~430K. In Figure 2.6(a), the measured atomic periodicity is 0.31 ± 0.01 nm, in agreement with nearest neighbor separation of 0.316 nm. During this particular experiment, the character of the image changed dramatically at one point. Figure 2.6(b) is an image that was subsequently obtained. The lattice is greatly distorted and the corrugation enhanced. This behavior is most likely due to the presence of a sliding flake between the tip and the sample, a phenomenon previously observed with scanning probe microscopy on other layered materials[27]. The flake slides between the tip and sample during scanning, and the periodicity along the scan direction is therefore reduced. By pulling the tip out of contact with the surface and then placing it in contact again, the images reverted back to the type shown in Figure 2.6(a), with the usual lattice spacing.

2.4.3 Below Room Temperature (110 K)

A mica sample was cleaved in UHV and then cooled until the sample block was at 90K. A 10×10 nm^2 atomic lattice resolution image is presented in Figure 2.7 showing simultaneous topographic and lateral force images. This image was acquired roughly 60 minutes after lowering the microscope onto the cooled ramp/block. From the aforementioned temperature measurements, the sample temperature is estimated to be ~110K for this image. The inset spatial Fourier transform of the image indicates that distortion due to drift is not dramatic. The error in the spot position in the Fourier transform is due to a roughly 10% decrease in the piezo gain due to slight cooling. The mica surface could be reproducibly imaged with atomic lattice resolution over the entire range of 110 - 296K.

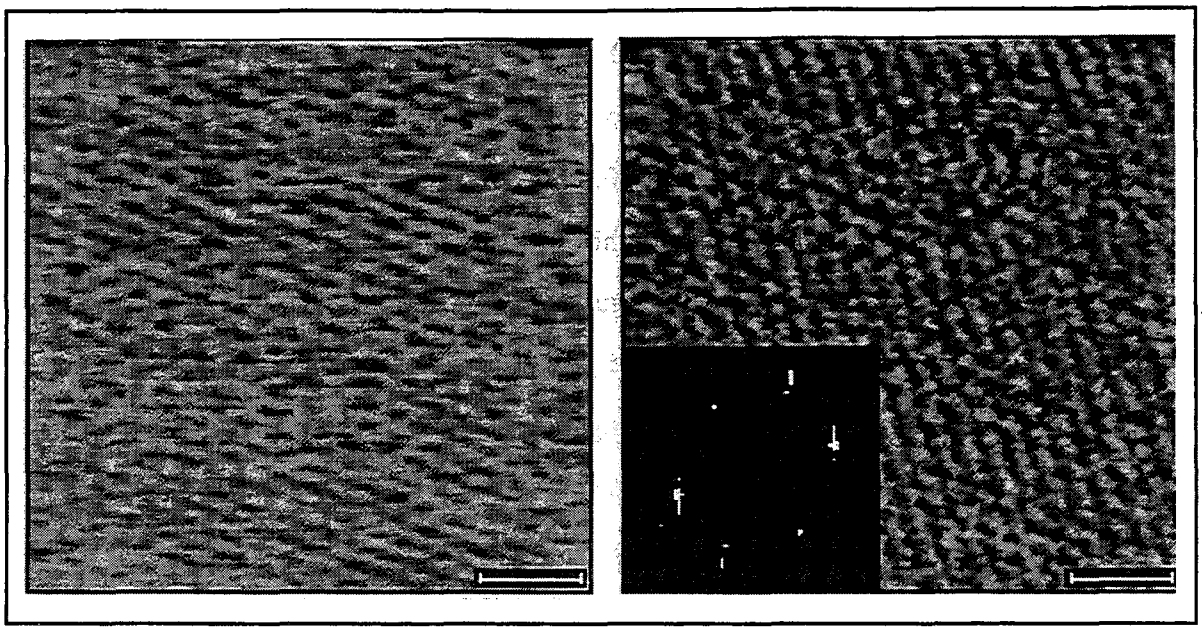

(a) (b)

Figure 2.7 Simultaneous (a) topographic and (b) lateral force images (10 x 10 nm^2) of mica at ~110K. The scale bar in the figures represents 2 nm. The contrast arises from atomic scale stick-slip behavior. The inset Fourier transform closely resembles the hexagonal pattern expected for mica. The spot locations differ from those measured at room temperature by ~10%, indicating a small decrease in piezo gain due to slight cooling. The spot angles (0°, 56°, 125°) indicate small distortion due to thermal drift during imaging. The images were acquired in approximately 30 seconds.

2.5 Summary

A UHV AFM has been constructed and tested. The instrument can measure atomic-scale variations in normal and lateral forces. The system provides a wider experimental temperature range, 100 - 450 K, than any other known UHV AFM in operation. The chamber is equipped with surface preparation and analytical instruments to take full advantage of the UHV environment.

Chapter 2 References

[1] Q. Dai, R. Vollmer, R. W. Carpick, D. F. Ogletree, and M. Salmeron, Rev. Sci. Instrum. **66,** 5266 (1995).

[2] M. Binggeli and C. M. Mate, Appl. Phys. Lett. **65,** 415 (1994).

[3] G. Meyer and N. M. Amer, Appl. Phys. Lett. **56,** 2100 (1990).

[4] S. Alexander, L. Hellemans, O. Marti, J. Schneir, V. Elings, P. K. Hansma, M. Longmire, and J. Gurley, J. Appl. Phys. **65,** 164 (1989).

[5] O. Marti, J. Colchero, and J. Mlynek, Nanotechnology **1,** 141 (1991).

[6] G. Neubauer, S. R. Cohen, G. M. McClelland, D. Horne, and C. M. Mate, Rev. Sci. Instrum. **61,** 2296 (1990).

[7] E. Meyer, H. Heinzelmann, D. Brodbeck, G. Overney, R. Overney, L. Howald, H. Hug, T. Jung, H.-R. Hidber, and H.-J. Guntherodt, J. Vac. Sci. Technol. B **9,** 1329 (1990).

[8] G. J. Germann, S. R. Cohen, G. Neubauer, G. M. McClelland, H. Seki, and D. Coulman, J. Appl. Phys. **73,** 163 (1993).

[9] L. Howald, E. Meyer, R. Lüthi, H. Haefke, R. Overney, H. Rudin, and H.-J. Güntherodt, Appl. Phys. Lett. **63,** 117 (1993).

[10] M. Kageshima, H. Yamada, K. Nakayama, H. Sakama, A. Kawau, T. Fujii, and M. Suzuki, J. Vac. Sci. Technol. B **11,** 1987 (1993).

[11] M. Ohta, Y. Sugawara, S. Morita, H. Nagaoka, S. Mishima, and T. Okada, J. Vac. Sci. Technol. B **12,** 1705 (1994).

[12] F. J. Giessibl and B. M. Trafas, Rev. Sci. Instrum. **65,** 1923 (1994).

[13] F. J. Giessibl, C. Gerber, and G. Binnig, J. Vac. Sci. Technol. B **9,** 984 (1991).

[14] J. Frohn, J. F. Wolf, K. Besocke, and M. Teske, Rev. Sci. Instrum. **60,** 1200 (1989).

[15] Ultralever, Park Scientific Instruments, Sunnyvale, CA.

[16] M. Radmacher, J. P. Cleveland, and P. K. Hansma, SCANNING **17,** 117 (1995).

[17] NT-MDT Inc., Moscow, Russia.

[18] Newport Corporation, Fountain Valley, CA.

[19] EBL 3, Stavely Sensors, East Hartford, CT.

[20] C. J. Chen, Appl. Phys. Lett. **60,** 132 (1992).

[21] Varian Vacuum Products, Sugar Land, TX.

[22] Epoxy Technology Inc., Billerica, MA.

[23] NSG America Inc., Somerset, NJ.

[24] RHK Inc., Rochester Hills, MI.

[25] Parker Seals, Lexington, KY.

[26] O. Marti, A. Ruf, M. Hipp, H. Bielefeldt, J. Colchero, and J. Mlynek, Ultramicroscopy **42-44B,** 345 (1992).

[27] M. Salmeron, D. F. Ogletree, C. Ocal, H.-C. Wang, G. Neubauer, W. Kolbe, and G. Meyers, J. Vac. Sci. Technol. B **9,** 1347 (1991).

3. Force Calibration

3.1 Introduction

In this chapter we consider a number of specific issues related to the calibration of force measurements using friction force microscopy (FFM). As discussed previously, FFM can provide information on the atomic level frictional properties of surfaces. However, reproducible quantitative measurements are in fact difficult to obtain for reasons we shall discuss below.

The most common experimental apparatus for FFM combines commercially available microfabricated silicon or silicon nitride cantilever-tip assemblies with an AFM using optical beam deflection sensing[1,2]. All commercially available scanning probe microscopes capable of FFM and many custom designed instruments use this combination[3,4].

Microfabricated cantilevers offer many advantages - they are available in a range of force constants, their small size leads to high resonant frequencies, they are relatively easy to use, and the tips are relatively sharp and durable. On the other hand, their small size makes it difficult to make direct measurements of mechanical properties such as the force constants of the cantilever. Calculation of cantilever force constants are also difficult as they depend on knowledge of critical dimensions such as lever thickness and tip height that are difficult to control in fabrication and difficult to measure accurately even with a good scanning electron microscope (SEM). The mechanical properties of silicon nitride cantilevers produced by chemical vapor deposition (CVD) can vary widely[5,6]. Levers are often metalized to increase optical reflectivity, but the thickness and mechanical properties of the coating (grain size, *etc.*) may not be known and the effect of metalization on the

cantilever force constants can be significant[7]. In general, calculations for the commonly used V-shaped levers require complex numerical methods[8,9].

The optical beam deflection sensor also has experimental advantages for FFM along with difficulties for quantitative friction measurements. One sensor can measure deflections due to both normal and lateral forces. The sensitivity and signal/noise ratio of this method are good and changing cantilevers is relatively easy. However, both the absolute values and the *ratio* of normal and lateral force sensitivity depends on the precise alignment of the laser beam with respect to the cantilever. Furthermore, the angular deflection of commercial cantilevers due to lateral forces is one to two orders of magnitude smaller than for normal forces, so small misalignments can cause significant errors in lateral force measurement due to cross-talk between normal and lateral deflections.

In general, discussion or even statements of uncertainties in AFM measurements is often neglected. A good introduction to aspects of error analysis with force microscopy is contained in the paper of Schwarz *et al.*[10] Here we will discuss some experimental aspects of the optical deflection FFM, present methods for estimating the normal and lateral response of microfabricated cantilevers, describe the "wedge" method of force calibration, and present experimental results for commercial V-shape cantilevers[11].

3.2 Optical Beam FFM

In the optical beam deflection method, a laser beam is reflected off the back of the AFM cantilever into a quadrant photodiode position sensitive detector. We define a coordinate system with X along the lever long axis, Z along the tip axis, and the origin at the base of the lever. The incident laser beam is in the X-Z plane, and the reflected beam is incident on a four-quadrant photodiode which is (ideally) oriented with one axis along the Y direction in the X-Z plane (Figure 3.1). For small deflections the difference in photocurrent between the upper and lower pairs of diodes (A-B) will be proportional to the slope of the lever in the X-Z plane at the point of reflection X_{LASER}. Similarly, the difference in photocurrent between the left and right pairs of diodes (1-2) is proportional to the lever

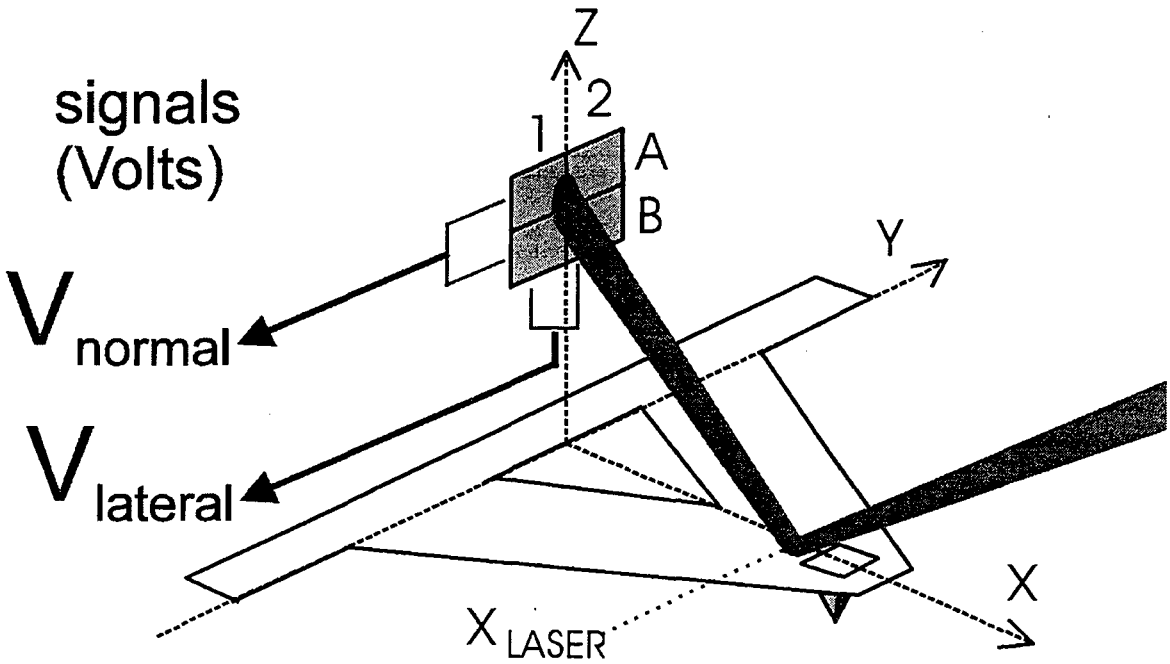

Figure 3.1 Schematic of cantilever and deflection sensor for the optical beam deflection FFM. The incident laser beam in the X-Z plane is deflected proportional to the slope (not the displacement) of the lever X-Z plane, and to the twist of the lever normal out of this plane, at the point where the laser beam hits the lever.

twist out of the X-Z plane at X_{LASER}.

The photodiode output signal S as a function of angular deflection φ can be calculated for a Gaussian beam if the total size of the photodiode is large compared to the laser spot and the "dead" area between the quadrants is neglected. In this case

$$S(\varphi) = \frac{A-B}{A+B} = 1 - \frac{1}{\Delta\omega}\sqrt{\frac{8}{\pi}}\int_{\varphi}^{\infty} e^{\frac{-2u^2}{\Delta\omega^2}}\,du \qquad (3.1)$$

where $\Delta\omega$ is the Gaussian half width (angular divergence) of the beam, A is the photocurrent on the upper two quadrants, and B is the photocurrent on the lower two quadrants. This expression cannot be integrated analytically, but it may be expanded around $\varphi = 0$ (see Appendix), with $x = \dfrac{\varphi}{\Delta\omega}$

$$S(x) = \sqrt{\tfrac{8}{\pi}}x[1 - \tfrac{2}{3}x^2 + \tfrac{2}{5}x^4 - \tfrac{4}{21}x^6 + \ldots] \qquad (3.2)$$

The term in square brackets describes the non-linearity of the detector response. For $S = 0.2$, the deviation from linearity is -1% and for $S = 0.5$ it is -6.1%. Under our typical

experimental conditions, a normal force of ~ 1 nN produces a deflection $S \sim 0.002$. The photodiode detector signal is quite linear in response to FFM lever deflection over a relatively wide range, which we have verified experimentally using a laser interferometer to independently monitor microscope displacement.

If the reflected laser beam is round, the angular sensitivity is equal for deflections due to normal and lateral forces. This is often not the case under experimental conditions. Most optical beam FFMs use diode lasers, which produce asymmetric beams. In addition, if the laser spot is not carefully focused and aligned on the cantilever, there may be significant diffraction effects where the reflected spot is cut off by the cantilever edge. Let

$$R_{DETECTOR} = \frac{dS_{NORMAL}}{d\vartheta} \Big/ \frac{dS_{LATERAL}}{d\phi} \tag{3.3}$$

describe the angular sensitivity ratio for normal and lateral angular deflections. If the beam is focused on the cantilever through a single-mode optical fiber, it is possible to have a radially symmetric and well focused Gaussian beam incident on the cantilever. In this case $R_{DETECTOR}$ can be very near 1.

Forces acting on the apex of the tip in the Z direction cause the lever to bend with a displacement z and tip spring constant k_Z of the form

$$z(F_Z, x) = F_Z f(x) \tag{3.4}$$

$$k_Z = 1 / f(X_{TIP}) \tag{3.5}$$

with the tip located at X_{TIP}. Microfabricated levers are generally planar, and quite stiff with respect to bending in the X-Y plane, and in any case such deformations cannot be detected by the optical beam method. The main effect of lateral forces (acting on the tip apex in the Y direction) is to twist the lever, with an angular deflection Θ and resulting tip spring constant k_Y of the form:

$$\Theta(F_Y, x) = F_Y g(x) \tag{3.6}$$

$$k_Y = 1 / \mathcal{H}_{TIP} g(X_{TIP}) \tag{3.7}$$

where $\mathcal{H}_{TIP}$ is the cantilever tip height. Longitudinal forces (acting on the tip apex in the X direction) are more complicated for the optical beam FFM. The in-plane compression of the lever is insignificant, so the main effect is to cause buckling of the lever in the X-Z plane

$$z(F_X) = F_X h(x) \quad . \tag{3.8}$$

The tip displacement Δx and associated spring constant k_X for the tip apex in the X direction due to cantilever buckling are

$$\Delta x = F_x \mathcal{H}_{TIP} \frac{\partial h(X_{TIP})}{\partial x} \tag{3.9}$$

$$k_X = 1 / \mathcal{H}_{TIP} \frac{\partial h(X_{TIP})}{\partial x} \tag{3.10}$$

Bending of the tip itself due to forces in the X or Y direction will not be detected by the optical beam method. Compression of the tip along its axis (Z direction) is insignificant.

We can define a lever deflection sensitivity ratio

$$R_{LEVER}(x) = \frac{\partial f(x)}{\partial x} \Big/ g(x) \tag{3.11}$$

as the ratio of angular deflections produced by normal and lateral forces.

For the "V-shape" cantilevers commonly used in FFM the functions $f(x)$, $g(x)$ and $h(x)$ that describe the lever response must be calculated numerically. Some insight into the general properties of the optical beam method can be gained by considering the form of these functions for a simple rectangular beam lever of width $\mathcal{W}_L$ and thickness $\mathcal{T}_L$ which is small compared to its length $\mathcal{L}_L$, with a tip of height $\mathcal{H}_{TIP}$ at the extreme end ($X_{TIP} = \mathcal{L}_L$). Using familiar continuum elasticity theory formulas[12]

$$f(x) = \frac{6\mathcal{L}_L x^2 - 2x^3}{E\mathcal{W}_L \mathcal{T}_L^3} \tag{3.12}$$

$$g(x) = \frac{3H_{TIP} x}{G\mathcal{W}_L \mathcal{T}_L^3} \tag{3.13}$$

$$h(x) = \frac{6H_{TIP}x^2}{E\mathcal{W}_L\mathcal{T}_L^3} \tag{3.14}$$

where E and G are the Young's and shear moduli of the cantilever. Notice that these functions do not have the same x dependence - the ratio as well as the absolute values of the angular sensitivities to normal and lateral forces depend on the laser spot position X_{LASER}. For the simple beam

$$R_{LEVER}(x) = \frac{2\mathcal{L}_L - x}{H_{TIP}(1+\nu)} \tag{3.15}$$

where

$$G = \frac{E}{2(1+\nu)} \tag{3.16}$$

defines the Poisson ratio ν.

Typical microfabricated cantilevers have tip heights ~ 3 - 4 μm and lengths ~ 80 - 300 μm, so the lateral force signals are ~ 20 to 80 times smaller than the normal force signals. Uncertainty in tip height will cause an error $\Delta R_{LEVER}/R_{LEVER}$ of $\sim\Delta H_{TIP}/H_{TIP}$, and uncertainty in laser spot position will cause an error of ~ $X_{LASER} / \mathcal{L}_L$ if the laser spot is near the end of the lever.

3.3 Spring Constant Estimates

An estimate of the response of a "V" lever has been made by treating it as a variable width beam. The curvature of a small solid element is proportional to the moment of torque acting on it and inversely proportional to the product of the elastic modulus and the moment of inertia around the bending axis[12]. Using this approach for the lever, the curvature at a distance x from the base of the lever is

$$\frac{\partial^2 z(x)}{\partial x^2} = \frac{F_Z \cdot (X_{TIP} - x)}{EI(x)} \tag{3.17}$$

where the moment of inertia $I(x) = \frac{1}{12}\mathcal{W}_L(x)\mathcal{T}_L^3$ depends on the projected width of the lever along the y axis. Likewise the curvature due to lateral forces is

$$\frac{\partial\Theta(x)}{\partial x} = \frac{F_Y H_{TIP}}{GI(x)} \tag{3.18}$$

These expressions can be integrated analytically for each section and combined, matching boundary conditions for continuity, to give $g(x)$ and $\partial f(x)/\partial x$ along the lever.

This approach is similar to the "parallel beam approximation" (PBA) analyzed in detail by Sader[13]. Warmack *et al.*[14] have also used this type of approach to analyze normal deflections and the effects of cantilever buckling on AFM response. Unlike Sader and references therein, we also calculate torsional and buckling force constants, and explicitly include the effect of the triangular "fillets" (a 10% effect for short levers) in the corners of the central area cut-out of the "V" lever (Figure 3.2). Our approach gives the same result as Sader's first order solution for the solid triangle region at the end of the lever. His analysis shows that using the actual arm width, instead of the arm width projected in the Y direction, is a better approximation for the normal force constant. Sader's analysis also shows that values for the normal force constant estimated by good PBA-type approximations are within 10-20% of the results of a detailed finite element calculation. The errors resulting from the approximations used in the force estimates are probably less than the errors due to uncertainty in the physical properties of the lever (thickness, modulus, tip height, metalization thickness, *etc.*).

The results of this calculation for a Park Scientific Instruments "F" lever that is displayed in Figure 3.2 are shown in Figure 3.3, assuming an elastic modulus of 155 GPa and a Poisson ratio of 0.27 for CVD silicon nitride[5]. If the laser beam is positioned in the center of the triangular region at the end of the lever, the estimated angular deflections produced by normal, lateral and buckling forces are 32.2, 1.26 and 1.99 μrad/nN, respectively. For this relatively short and stiff lever, the triangular fillets increase the normal stiffness by ~10%. Integrating the expressions for angular deflection a second time, we obtain estimates for the force constants of 0.508, 132 and 209 N/m. The nominal normal force constant for the "F" lever is 0.50 N/m. These calculation have not taken the tip offset into account (Figure 3.2), nor the effect of the gold coating.

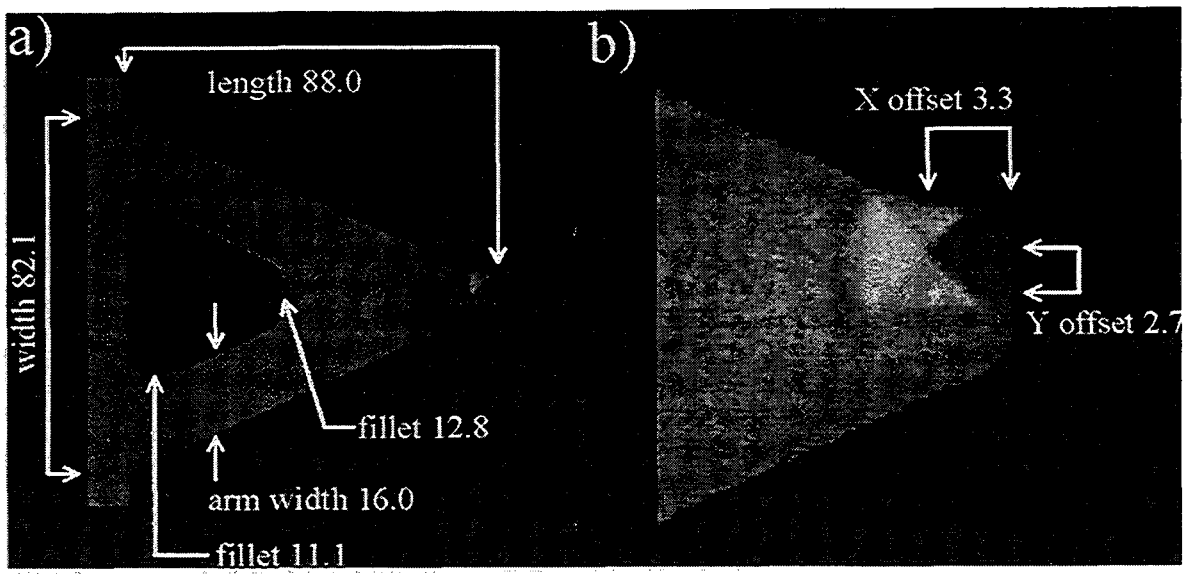

Figure 3.2 (a) A scanning electron micrograph of a gold coated Park Scientific Instruments "F" cantilever. The indicated dimensions are in micrometers. (b) A higher magnification view of the end of the lever, showing the position of the tip (at the apex of the pyramid) relative to the lever. The tip is off-axis by an amount close to its nominal height of 3 micrometers, which is an additional source of coupling between normal and lateral forces.

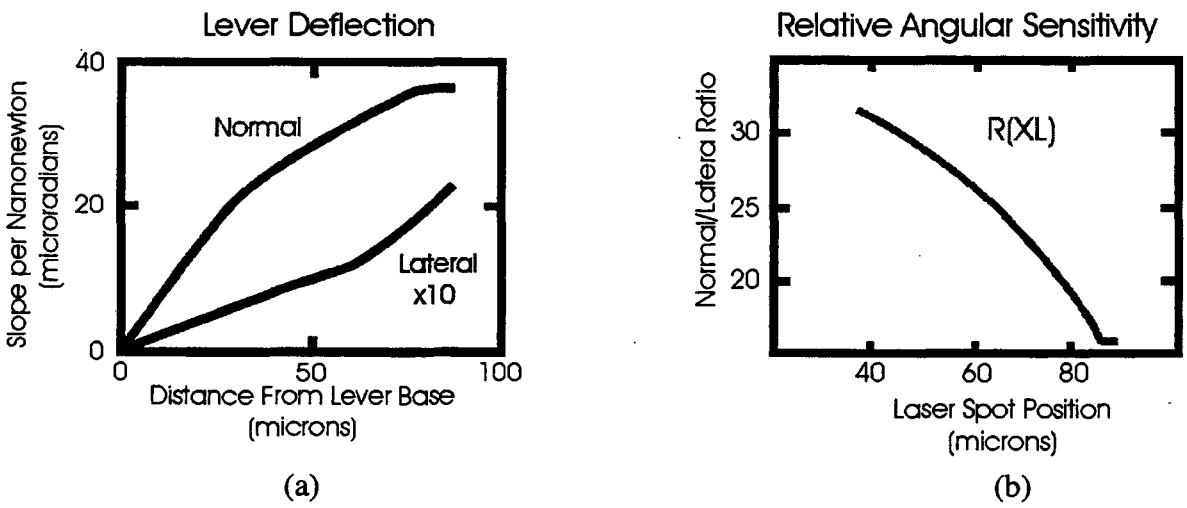

Figure 3.3 (a) Calculated curves showing the variation in slope (in micro-radians) along the length of the triangular region at the end of the cantilever shown in Figure 3.2 for a 1 nN normal or lateral force (lateral slope ×10). (b) The ratio of angular deflections for this lever in response to normal and lateral forces, as a function of the laser spot position. A ~10 μm uncertainty in laser spot position will give a 20% variation in measured friction coefficient.

The sensitivity ratio $R_{LEVER}(x)$ is plotted in Figure 3.3(b). This graph shows that R_{LEVER} is about 20% more sensitive to laser spot position for the "V" lever than for the simple beam of the same length and tip height. This is because the triangle at the end of the "V" lever twists more than any other part, while most of the bending takes place near the base of the cantilever, where the normal force lever moment is the greatest.

For any of these calculations, all the cantilever dimensions and the relevant moduli of elasticity (Young's modulus, shear modulus, Poisson ratio) are needed to calculate the force constants. The density is also needed to calculate the resonance frequency, which is a useful comparison because the free resonance frequency of these cantilevers is typically very easy to measure from the power spectrum of the cantilever's thermal vibrations. Such a measurement reduces the number of unknowns in the calculations[15]. In any event, the dimensions of the cantilevers are not easy to measure (a good scanning electron microscope is required, particularly to measure the sub-micrometer thickness of the cantilever which is a critical parameter), and the elastic moduli and density of the cantilever materials are uncertain.

3.4 Normal Force Calibration

While these formulae and calculations are useful to obtain estimates of the forces applied, clearly from the above discussion it is much more desirable to have an *in-situ* method of directly measuring cantilever force constants. Unfortunately, since the microfabricated levers are so small, non-destructive *in-situ* testing is difficult. Nonetheless, some methods for calibration of the normal force constant have been successfully implemented. These include: measuring deflections or resonance frequency shifts for levers loaded with known masses[16-18], and measuring the deflection of the cantilever when in contact with another lever of known spring constant[19,20]. Comparison of the cantilever's thermal noise with formulae can provide a calibration[21] although measurements of the cantilever's properties are still required. It is incorrect to use formulae which regard the cantilever as a point mass on the end of a massless spring, as was done in

one paper[22]. Currently, most AFM work has estimated forces from calculations like those mentioned above[15], including the work discussed in this thesis.

3.5 Lateral Force Wedge Calibration

In this section we describe an *in-situ* method of experimentally measuring the combined response of the lateral force transducer (the cantilever/tip combination) and the deflection sensor. Our method is based on comparing lateral force signals on surfaces with different slopes. The known geometrical contribution to the total lateral force, *i.e.* the product of the applied load and the tangent of the slope, gives a direct calibration of lateral force response in terms of the normal force response. If the normal force constant is known, then completely quantitative friction measurements can be made. Even if the normal force constant is uncertain, the ratio of normal to lateral forces can be determined quantitatively. An experimental force calibration is made by sliding the tip across a surface of known slope and measuring the lateral force signal as a function of applied load.

In principle, this could be carried out on any surface that is tilted with respect to the lateral scanning direction. In practice, this is difficult to realize because (a) if the surface is tilted by the experimenter, there will be some uncertainty in the tilt angle, (b) we will show that to accurately calibrate the lateral force response, *two* surfaces of different tilt angles must be used and (c) it may not be possible to contact the tip to a tilted surface without the surface touching the side of the cantilever chip or its holder, since microfabricated cantilever tips are usually very short.

These problems are resolved by using the faceted $SrTiO_3$ (305) surface proposed by Sheiko *et al.*[23] as a measure of tip sharpness. This sample is commercially available. When annealed in oxygen, $SrTiO_3$ (305) facets into a (101) and (103) planes which form extended ridges along the [010] direction. The (101) and (103) planes are respectively tilted -14.0° and +12.5° with respect to the original (305) surface. The ridges are typically 5 to 20 nm high and are spaced 10 to 100 nm apart (Figure 3.4). We thus have a test sample that provides two sloped surfaces with exactly known relative angles. Furthermore,

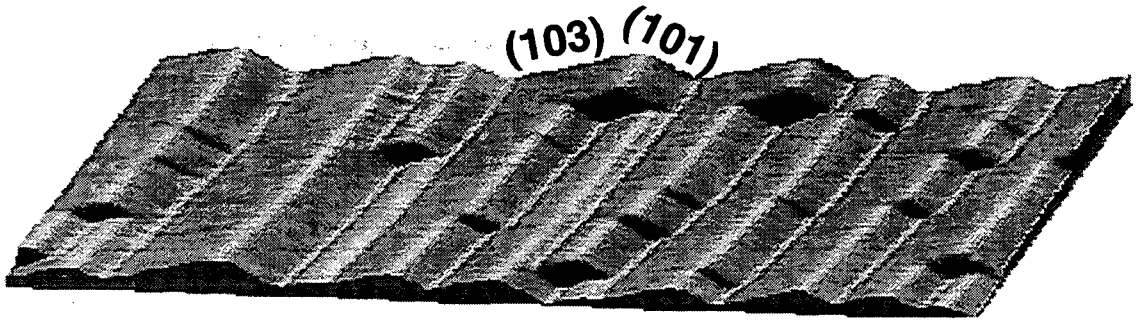

Figure 3.4 A 410×410 nm^2 topographic AFM image (light shaded) of the $SrTiO_3$ surface showing (103) and (101) facets. The apparent rounding of the ridge crests is due to the ~40 nm radius of the AFM tip used for this image. The widest facets are used to measure lateral signals as a function of load for the cantilever lateral force calibration.

as demonstrated by Sheiko *et al.*, the top of the $SrTiO_3$ ridges are extremely sharp, and a topographic AFM scan over the ridge produces an image of the tip. This is also quite important, as accurate knowledge of the tip shape is also required for quantitative FFM experiments[24].

The wedge method has some additional advantages. It can be used to determine the absolute orientation of the sample while confirming the microscope Z calibration. Even though the angle between the two $SrTiO_3$(305) facets is known, the average surface normal may be tilted by a small angle relative to the microscope Z axis. Calibrating the AFM XY displacement is usually not too difficult. Crystal lattices can be used for nanometer scale standards, and lithographically patterned standards work on the μm scale. We calibrate Z displacement in terms of XY displacement by making a topographic image of the $SrTiO_3$ sample, and adjusting Z until the angle between the facets is 26.5°. Now that XY and Z are calibrated, the overall slope of the surface can be directly determined from the image (in practice we solve for the slope and Z calibration simultaneously, see the Appendix for details).

To get an accurate force calibration with the wedge method, the tip must slide across one facet for a reasonable distance before reaching the next facet or ridge crest. This is not possible unless $2R_{tip} \sin\theta$ is significantly smaller than the spacing between ridge

crests. It is difficult to calibrate tips with radii greater than ~ 100 nm even using the widest facets on our $SrTiO_3$ sample. The procedure is straightforward for tip radii ~ 50 nm or less. It may be possible to prepare a similar sample with larger facets for calibrating blunt tips.

3.6 Wedge Calculations

The vector diagrams in Figure 3.5 show the forces acting on the end of the tip while scanning up or down a sloped surface. The two forces applied by the tip on the surface, the vertical load L (down is positive) and the horizontal tractive force T (right is positive) must be balanced by a reaction force from the surface acting on the tip. This can be divided into two components, a friction component F_f parallel to the surface and a second component N normal to the surface. When the tip slides across the surface, these forces are in equilibrium. At a given load, the tractive, friction and normal forces depend on the direction of motion, so

$$N_{\pm} = L\cos\theta \pm T_{\pm}\sin\theta \tag{3.19}$$

$$F_f(N_{\pm}) = T_{\pm}\cos\theta \mp L\sin\theta \quad . \tag{3.20}$$

In these equations '+' denotes uphill motion and '-' downhill motion. N, L and T

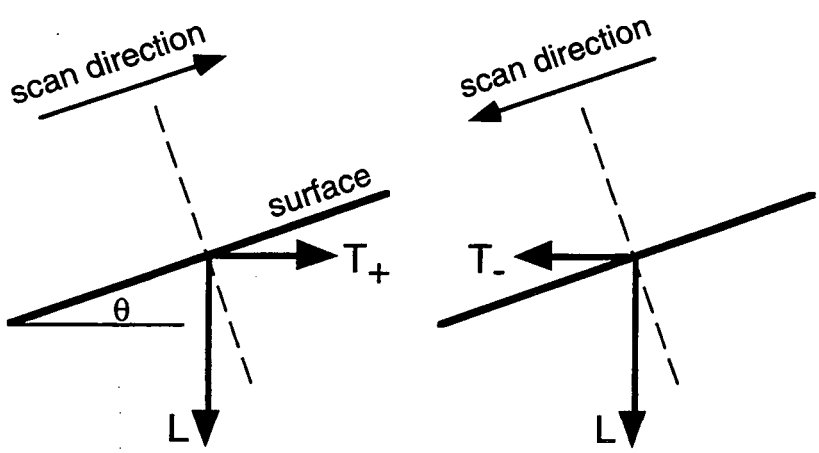

Figure 3.5 Forces exerted on the surface by the AFM tip while scanning up or down a sloped surface.

are signed quantities, while F_f is the positive magnitude of the frictional force acting against the direction of motion.

We experimentally measure the voltage output from the lateral force transducer T_o where $\alpha T_o = T$ (the 'o' subscript will be used to indicated a force measured in transducer output volts rather than Newtons). If we can find α (Newtons per volt) we have a direct calibration of the lateral force response of the FFM. The calibration constant α is a product of all the factors of the experiment - the lever lateral force constant, the deflection of the reflected laser beam as a function of lateral tip displacement, and the photodiode angular sensitivity. This method will work equally well for other types of lateral force transducers, including optical interferometry and piezoresistive detection.

To solve the calibration problem we need a functional form for the frictional force $F_f(L)$. This can be an empirical fit from measuring friction on a flat surface, or a theoretical form from the Hertz or JKR theories[24]. These shall be discussed in detail in Chapter 5. Tip-surface adhesion usually has a significant effect on $F_f(L)$ in FFM experiments. When friction is linearly dependent on load, adhesion is often treated as a force offset. We find experimentally that the friction-load relation for silicon or silicon nitride tips on the strontium titanate surface in air is well represented by a linear form $F_f(N_\pm) = \mu \bullet (N_\pm + A)$ where A is the adhesion or pull-off force. In this case

$$N_+ = \frac{L + \mu A \sin\theta}{\cos\theta - \mu \sin\theta} \tag{3.21}$$

and

$$N_- = \frac{L - \mu A \sin\theta}{\cos\theta + \mu \sin\theta} \tag{3.22}$$

Note that the normal force depends on the friction and on the direction of motion.

On a flat surface, the "frictional force" is determined by taking half the difference between the left-to-right and right-to-left lateral deflection forces, *i.e.* the half width of the friction loop $W(L)$. In this case, since the surface is tilted, the effective load is direction-dependent, and the expression for $W(L)$ is more complicated. Furthermore, the offset of

the friction loop $\Delta(L)$ is not zero and depends on load. This is illustrated in Figure 3.6, where bi-directional lateral force loops are drawn for flat, positively tilted, and negatively tilted surfaces respectively and the measured quantities W_o and Δ_o are indicated.

Experimentally, we measure lateral forces for a range of applied loads, and use the slopes $\Delta' \equiv \partial\Delta/\partial L$ and $W' \equiv \partial W/\partial L$ in calculations, which are independent of L due to the assumption of linearity. This eliminates the pull-off force from the equations, as well as any DC offset in the lateral force sensor. These slopes are given by:

$$\alpha\Delta_o' = \Delta' = \frac{(1+\mu^2)\sin\theta\cos\theta}{\cos^2\theta - \mu^2\sin^2\theta} \tag{3.23}$$

and

$$\alpha W_o' = W' = \frac{\mu}{\cos^2\theta - \mu^2\sin^2\theta} \tag{3.24}$$

In the limiting cases of no friction, $\Delta' \to \tan\theta$ and $W' \to 0$, and for no slope $\Delta' \to 0$ and $W' \to \mu$ as expected. Using these two equations, we can calculate the tip-surface

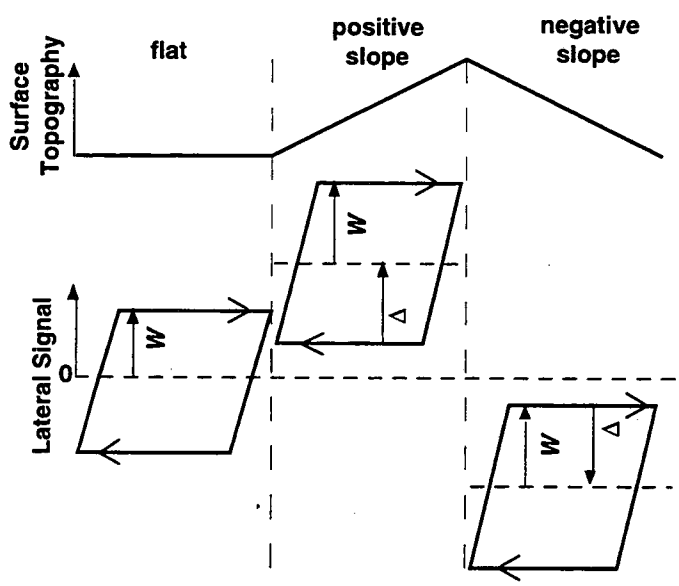

Figure 3.6 Schematic "friction loops" (lateral signals for back and forth scans) for flat, positively sloped and negatively sloped surfaces at the same applied load. The friction loop half-width W is slightly different for the three cases, while the loop offset Δ is substantially different and is indicative of the overall tilt of each surface. The values of W and Δ are measured over a range of applied loads for known slopes and used to calibrate the lateral force response of the cantilever.

friction coefficient and lateral force calibration constant. The ratio of these expressions gives μ:

$$\mu + \frac{1}{\mu} = \frac{2\Delta_o'}{W_o' \sin 2\theta} \tag{3.25}$$

From the form of this expression, there is an ambiguity in the problem, since μ and $1/\mu$ are equally good mathematical solutions which give different results for α. This ambiguity may be resolved by choosing the appropriate root using an estimate for α from the type of calculation described in section 3.3, or if μ is assumed to be less than one. Once μ is determined, α can be found from the equations defining W' or Δ'. Experimentally, it is best to solve for α using data from two different slopes, as discussed below.

3.7 Experimental Difficulties

In the ideal case, the lateral force response of the cantilever and deflection sensor has now been calibrated. However there can be significant "cross talk" between normal and lateral cantilever deflections. As discussed above, the response of the optical beam FFM deflection sensor is 20-80 times greater for normal forces than for lateral forces. In addition, the normal forces are often larger than the lateral forces. A small misalignment of the laser or cantilever with respect to the quadrant photodiode, for example a rotation of the photodiode by ~ 2°, can mean that the normal force contribution to the lateral deflection output is as large as the actual lateral force contribution. In normal FFM experiments this problem is avoided by measuring friction loop width, or $W(L)$, since the "cross talk" primarily effects the friction loop offset $\Delta(L)$. Cross talk is a concern in the wedge calibration experiment since the lateral force offset $\Delta(L)$ is important in the calibration calculation.

In our experiment, we compensate for the cross talk electronically, by adding or subtracting a fraction of the normal force output from the lateral force output. The compensation is adjusted by taking an approach curve, or by oscillating the cantilever out of contact with the surface, where there should be no "real" lateral forces, and adjusting the

compensation to null the lateral force output. Such compensation is also available on some commercial FFM electronics[25]. Even with careful compensation, the residual cross talk may be too large to neglect in the calibration calculations.

The effect of cross talk can be minimized by measuring Δ_0' and W_0' on the (103) and (101) facets of the $SrTiO_3$ surface and then using $\Delta_0'(103)-\Delta_0'(101)$, $W_0'(101)$ and $W_0'(103)$ for the calibration calculation. These quantities all involve *differences* between lateral signals for the same applied load, so cross talk has been subtracted out to first order. The details of the two-slope calibration are given in the Appendix.

The above discussion has assumed that the applied load L is known. Since the direct experimental calibration of normal spring constants is also difficult, in some cases only an experimental signal L_o proportional to the normal load, $L = \beta L_o$, is known. In this case it is not possible to get the absolute lateral force calibration, but only

$$R_{DETECTOR} \bullet R_{LEVER}(X_{LASER}) = \alpha/\beta. \tag{3.26}$$

It is still possible to get the friction coefficient μ if friction is proportional to load, since on a flat surface $\mu = R_{DETECTOR} \bullet R_{LEVER}(X_{LASER}) \bullet T_o/L_o$. It is not sufficient to assume that the voltage applied to the Z piezo is proportional to load, since there are significant non-linearities in piezo response, which depend on the speed and direction of displacement[26-28].

3.8 Experimental Lever Calibration

For the following example, we have not calibrated the normal force constant of the cantilever. Therefore, we will actually take derivatives of the experimentally measured quantities Δ_0 and W_0 with respect to L_0, the experimental load signal in output Volts. Thus, $\Delta_0' \equiv \partial\Delta/\partial L_0$ and $W' \equiv \partial W/\partial L_0$. In this case, equations (3.23) and (3.24) become

$$\alpha/\beta \cdot \Delta_o' = \Delta' = \frac{(1+\mu^2)\sin\theta\cos\theta}{\cos^2\theta - \mu^2\sin^2\theta} \tag{3.27}$$

and

$$\alpha/\beta \cdot W_o' = W' = \frac{\mu}{\cos^2\theta - \mu^2 \sin^2\theta} \tag{3.28}$$

We have thus used the wedge calibration procedure described with our AFM to measure α/β for cantilevers of three different nominal spring constants. In this system the laser beam is carried by a single-mode fiber and is well focused on the cantilever, so $R_{DETECTOR} \approx 1$[4]. The cantilevers are "V"-shaped silicon nitride "Sharpened Microlevers" from Park Scientific Instruments[29]. The levers are gold coated, and the pyramidal tips are etched back to get a sharp tip with a nominal radius of ≈30 nm. We made measurements on the "*D*", "*E*" and "*F*" levers which have nominal normal force constants 0.03, 0.10 and 0.50 N/m. Two different *E* levers from the same wafer were analyzed.

The $SrTiO_3$ sample was aligned so that the ridges were perpendicular to the lateral scanning direction. The lateral and normal bending signals were recorded as the tip scanned back and forth over both facets of a single ridge. The feedback was active so that each line scan across the sloped surface was recorded at the same externally applied load. After each line was recorded, the feedback set point (applied load) was increased under computer control, and another line scan acquired. 256 line scans of 256 points were recorded in each data set. The average value of the subset of points for each facet was calculated for each load. Figure 3.7 shows an example of unprocessed data from a single line scan (friction loop), showing the simultaneous topography and lateral deflection signals for both scanning directions.

A plot of lateral force *vs.* load, obtained in this case with an *E* lever, is shown in Figure 3.8. Figure 3.8(a) shows the lateral bending signals (left-to-right and right-to-left) plotted *vs.* the normal bending signal for both facets. Figure 3.8(b) shows the resulting friction loop width and offset plotted *vs.* the normal bending signal (load) for both facets, with linear fits to the data. As predicted in section 3.7, the slopes $W_0'(101)$ and $W_0'(103)$ are similar, while $\Delta_0'(101)$ and $\Delta_0'(103)$ reflect the change in sign of the tilt angle. The data deviates slightly from nonlinearity, although the linear fit results in at most a 3.5%

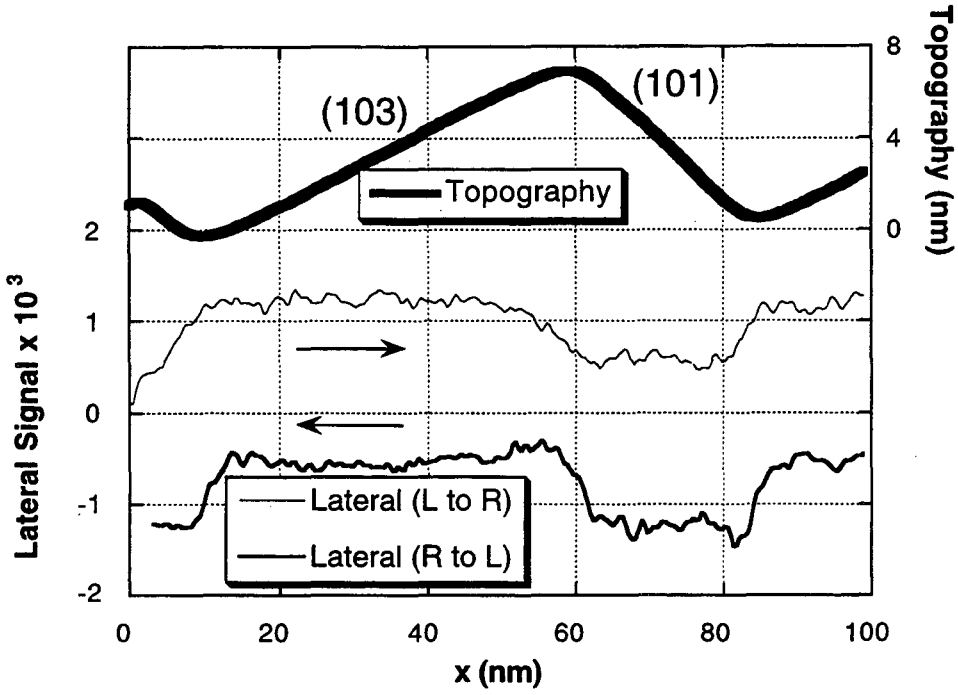

Figure 3.7 Experimental lateral deflection signals T_o $(1\text{-}2/A+B)$ measured on the (101) and (103) facets of the $SrTiO_3$(305) surface for each direction at a given load. The simultaneously acquired topography (thick line) is also shown. $W(L)$ and $\Delta(L)$ are calculated from this data. The complete series of measurements over a range of loads is shown in Figure 3.8.

statistical uncertainty in the slopes for a given measurement. A more complex fit than the simple linear fit utilized could be slightly more accurate, but would complicate the method substantially as equations (3.21) and beyond would need to be modified.

The two-slope wedge equations in the Appendix were used to calculate α/β. We did not have a good experimental value for the lever normal force constant, so we report α/β instead of the absolute lateral force response α. The results are summarized in Table 3.1.

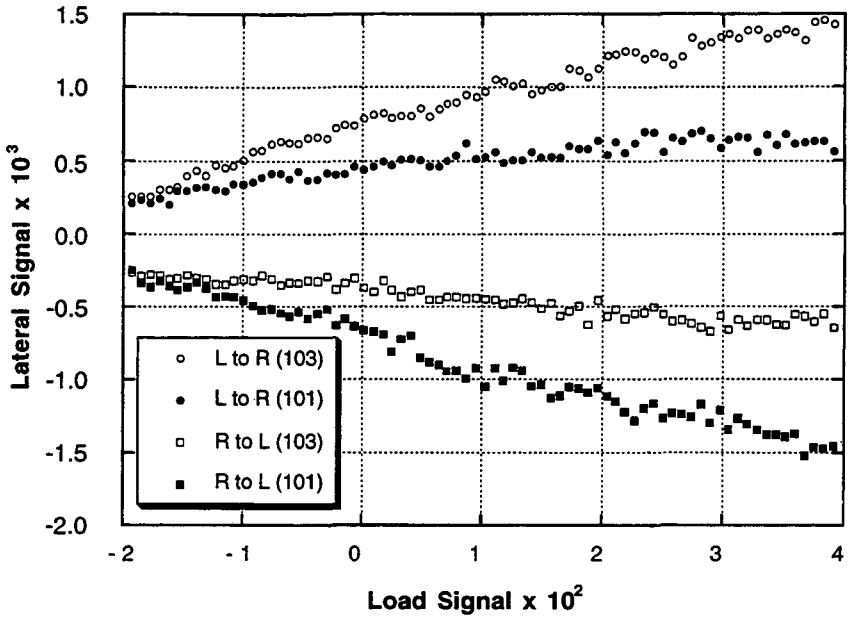

(a)

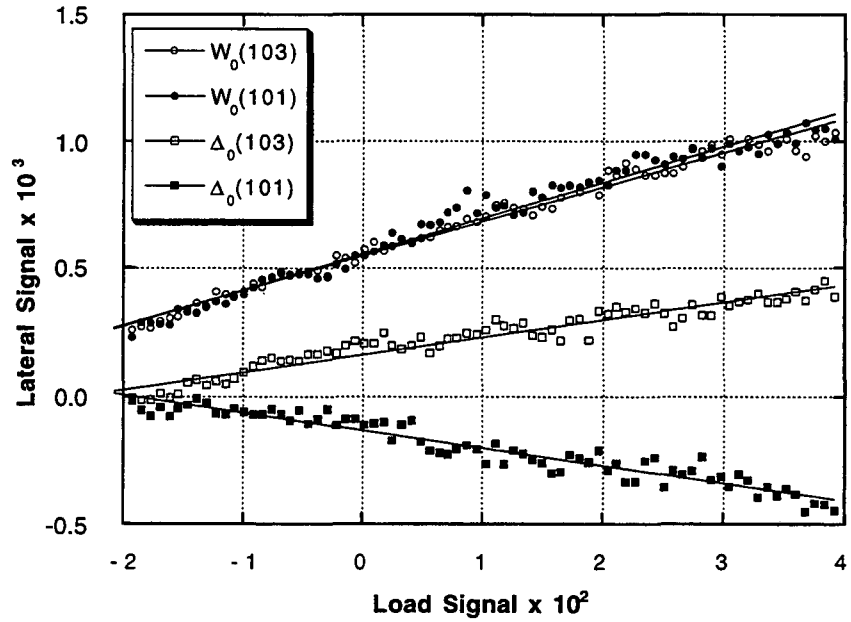

(b)

Figure 3.8 (a) Lateral deflection signals for left-to-right and right-to-left scanning directions ($1\text{-}2/A+B$) as a function of load deflection signal ($A\text{-}B/A+B$) for the (101) and (103) facets. The total $A+B$ signal (photodiode current) was 185 μA. (b) The friction loop width $W(L)$ and offset $\Delta(L)$ as a function of load for the (101) and (103) facets. Straight lines fit the data very well, justifying our assumption of linear friction behavior. The slopes of each line are measured and used in formulae given in the Appendix to solve for α/β, the normal force to lateral force deflection ratio.

Table 3.1 Experimental lever calibration results and estimates based on calculations.

	EXPERIMENTAL			ESTIMATED		
LEVER	μ_{101}	μ_{103}	α/β	R_{LEVER}	k_{NORMAL}	$k_{LATERAL}$
D (0.03)	.42±.10	.51±.09	51±6	61.6	.037	66.6
E#1 (0.1)	.50±.05	.52±.05	43±3	39.4	.111	92.7
E#2 (0.1)	.66±.14	.74±.12	36±4	39.4	.111	92.7
F (0.5)	.33±.02	.41±.03	19±1	25.5	.508	132

The α/β values are averages of several data sets, each acquired on a different ridge. For comparison, the table includes the spring constants estimated by the method of section 3.6, and the value for R_{LEVER} assuming that X_{LASER} was located in the center of the solid triangular region at the end of the lever (Figure 3.2). Some data sets were recorded on different days. The error quoted is the statistical variation. Since, for our instrument, $R_{DETECTOR} \approx 1$, then from equation (3.26) , $\alpha/\beta \approx R_{LEVER}$. We see from the results that the experimental α/β values are generally consistent with the R_{LEVER} values estimated from material properties, but the difference is not insignificant. The experimental friction coefficients tend to be slightly higher for the (103) facet of strontium titanate relative to the (101) facets. We noted more substantial variations in friction coefficients from day to day. As mentioned, these experiments were carried out in air with no humidity control. Friction coefficients on other materials measured with AFM have been observed to vary with relative humidity[30,31]. This may partially account for the variation of friction coefficients

observed. Friction coefficients may also vary from lever to lever due to changes in tip radius.

There are some subtle experimental requirements for successful application of this method. As stated before, the method will fail if the tip is too blunt as the tip will always be riding over the sharp ridges, instead of scanning on the facets. Generally a tip radius of 50 nm or less is required. Careful examination of the topographic image can verify if the tip is sufficiently sharp. Specifically, taking the numerical derivative of the topographic data perpendicular to the $SrTiO_3$ ridges will reveal if a constant slope is measured on the facets. This is the signature of the tip's contact with the flat facets as opposed to the sharp ridge.

Another problem can arise if the facet where one is scanning contains any contamination or a step. One can see in Figure 3.3 that the (101) facet often possesses small steps which can be difficult to perceive. One muse acquire a topographic image first to identify a locally flat pair of facets for the measurement.

3.9 Error Analysis

We have considered the propagation of errors for this calibration method. For a given uncertainty in the experimentally measured slopes $W_0'(101)$, $W_0'(103)$, $\Delta_0'(101)$, and $\Delta_0'(103)$, the uncertainty in α/β will depend upon the value of μ on each facet. μ apparently changes for different tips and different relative humidities. To facilitate this analysis, let us assume that $\mu_{101} = \mu_{103} \equiv \mu$. In general it is expected that the uncertainty will be smaller when μ is smaller since the measured signals are due more to geometry than friction, and it is this geometrical coupling that is leading to the calibration.

In Figure 3.9, we graph the experimental error in α/β as a function of μ for 1%, 3%, 5% and 10% uncertainty in the slope measurements. At low μ, the uncertainty approaches the fundamental limit, as expected. The error diverges for large μ since the sensitivity to geometry is overwhelmed by the friction signal.

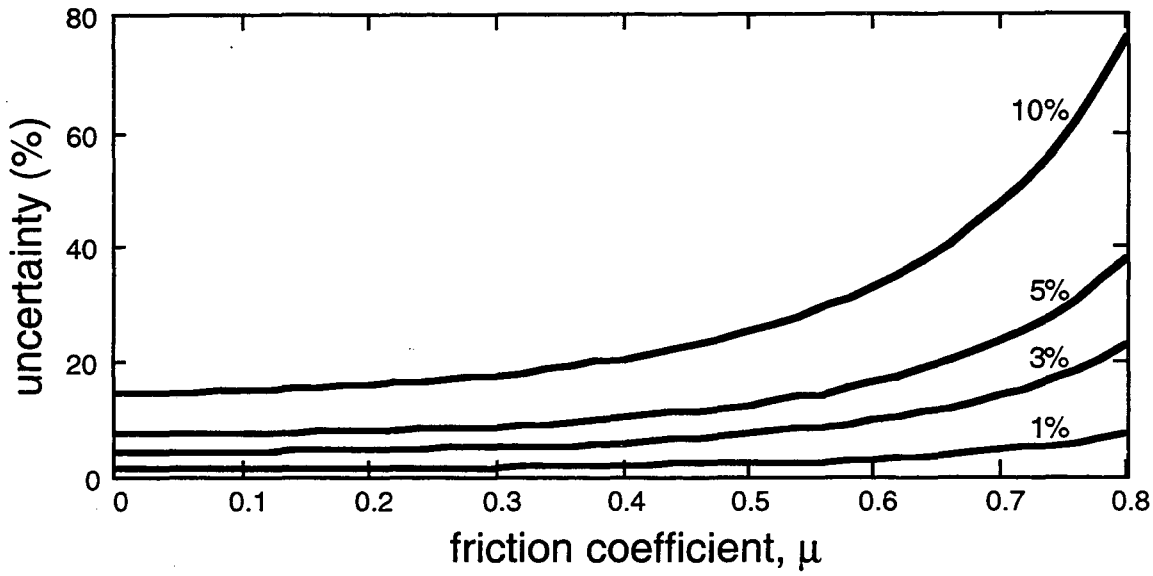

Figure 3.9 Uncertainty in the measurement of α/β as a function of the friction coefficient μ (for simplicity we assume that $\mu_{101} = \mu_{103}$). The error is calculated assuming the measurement error in W_0' and Δ_0' for both facets is 1%, 3%, 5% and 10%, respectively.

This calculation indicates that low friction is clearly desirable for this calibration method. Furthermore, we see that errors become unreasonable for $\mu > 0.7$. For most of the measurements performed, friction between tips and the $SrTiO_3$ sample is generally low enough for accurate measurements. Future work should attempt to measure μ as a function of relative humidity, to see which experimental conditions are optimal for the experiment.

3.10 Summary

We have demonstrated a quantitative method of lateral force calibration for the microfabricated tip-cantilever assemblies used in friction force microscopy. We find that there are significant variations among cantilevers fabricated from the same wafer. Tip variations also play a role. Furthermore, the overall system calibration depends on the precise alignment of the deflection sensor where optical detection is used.

In order to perform quantitative friction force microscopy with the atomic force microscope, it is important to perform an experimental force calibration for *each* cantilever sensor.

3.11 Appendix

3.11.1 Photodiode Response

An elliptical Gaussian beam has a normalized intensity distribution

$$\Gamma(y,z) = \frac{2}{\pi \Delta\omega_y \Delta\omega_z} e^{\frac{-2y^2}{\Delta\omega_y^2} + \frac{-2z^2}{\Delta\omega_z^2}} \tag{3.29}$$

Here $\Delta\omega$ is the angular half width of the *field* distribution, following the conventions of Gaussian optics. The half width of the intensity distribution is then $\Delta\omega/\sqrt{2}$. If the beam is deflected by d in the y direction, the signal is given by

$$S(d) = \frac{A-B}{A+B} = 1 - \frac{1}{\Delta\omega_y}\sqrt{\frac{8}{\pi}}\int_d^\infty e^{\frac{-2y^2}{\Delta\omega_y^2}} dy \tag{3.30}$$

The integral

$$I(d) = \int_d^\infty e^{\frac{-2y^2}{\Delta\omega_y^2}} dy = \int_0^\infty e^{\frac{-2(t+d)^2}{\Delta\omega_y^2}} dt \tag{3.31}$$

can be expanded around $d = 0$ by taking a derivative

$$\frac{dI}{dd} = \int_0^\infty \frac{\partial}{\partial d}\left[e^{\frac{-2(t+d)^2}{\Delta\omega_y^2}} \right] dt = \int_0^\infty -\frac{4(t+d)}{\Delta\omega_y^2} e^{\frac{-2(t+d)^2}{\Delta\omega_y^2}} dt = -e^{\frac{-2d^2}{\Delta\omega_y^2}} \tag{3.32}$$

likewise higher derivatives can be calculated

$$\frac{d^2 I}{dd^2} = \frac{4d}{\Delta\omega_y^2} e^{\frac{-2d^2}{\Delta\omega_y^2}} \tag{3.33}$$

and

$$\frac{d^3 I}{dd^3} = \left[\frac{4}{\Delta\omega_y^2} - \frac{16d^2}{\Delta\omega_y^4} \right] e^{\frac{-2d^2}{\Delta\omega_y^2}} \tag{3.34}$$

When these derivatives are evaluated at $d = 0$, the even terms vanish, as expected, since *S(d)* is an odd function. Finally we put these terms into a Taylor expansion and get

$$S(d) = \sqrt{\frac{8}{\pi}} \frac{d}{\Delta\omega_y} \left[1 - \frac{4}{3!}\left(\frac{d}{\Delta\omega_y}\right)^2 + \frac{48}{5!}\left(\frac{d}{\Delta\omega_y}\right)^4 - \frac{960}{7!}\left(\frac{d}{\Delta\omega_y}\right)^6 + \ldots \right]. \tag{3.35}$$

3.11.2 Z Calibration and Tilt Measurement

A measurement of the apparent topography of the $SrTiO_3$ sample slopes provides a

check of the relative Z:X piezo calibration, as well as determining the overall tilt of the sample with respect to the scanning plane. This is important because one must use the actual physical angles between the sloped facets and the scanning plane in the wedge calculations.

We assume that the X calibration of the piezo scanner is correct and that the initial Z calibration is approximate. We acquire a topographic image of the faceted strontium titanate surface, with known facet angles of θ_1 = -14.0° and θ_2 = 12.5° relative to the (305) plane. We wish to determine the correction factor γ for the Z calibration such that $Z_{TRUE} = \gamma \bullet Z_{INITIAL}$ and the macroscopic tilt angle ψ of the (305) surface relative to the scanning plane, projected onto the y-z plane.

From the image we measure the apparent slopes ($\Delta Z/\Delta X$) of the facets S_1 and S_2. Then $\tan(\theta_1 + \psi) = \gamma \bullet S_1$ and $\tan(\theta_2 + \psi) = \gamma \bullet S_2$. From this we make a quadratic equation

$$\tan(\theta_1 - \theta_2) = \frac{\gamma S_1 - \gamma S_2}{1 + \gamma^2 S_1 S_2} \tag{3.36}$$

Solving for γ gives positive and negative solutions. The positive solution is physically reasonable:

$$\gamma = \frac{(S_1 - S_2) - \sqrt{(S_1 - S_2)^2 - 4S_1S_2\tan^2(\theta_1 - \theta_2)}}{2S_1S_2\tan(\theta_1 - \theta_2)} \tag{3.37}$$

Then the tilt angle is easily calculated: $\psi = \tan^{-1}(\gamma \bullet S_1) - \theta_1$.

3.11.3 Two Slope Calibration

We wish to find the lateral force calibration α in terms of the experimentally measured quantities $W_0'(101)$, $W_0'(103)$, $\Delta_0'(101)$, and $\Delta_0'(103)$. This discussion assumes these derivatives are taken with respect to the calibrated load L. If the load is not calibrated, then these derivatives are taken with respect to the load signal L_0, and thus α is replaced by α/β in equations (3.40) and (3.44).

Since the magnitude and offset of lateral force coupling is unknown, we use the difference $\Delta_0'(101) - \Delta_0'(103)$ in the calculation. The ratios of uncalibrated experimental

values should be equal to the ratios of the forces as calculated from geometry in section 3.6. Therefore

$$p \equiv \frac{W_o'(101)}{W_o'(103)} = \frac{W_{101}'}{W_{103}'} \tag{3.38}$$

$$q \equiv \frac{\Delta_o'(103) - \Delta_o'(101)}{W_o'(101)} = \frac{\Delta_{103}' - \Delta_{101}'}{W_{101}'} \tag{3.39}$$

$$\alpha = \frac{W_{103}'}{W_o'(103)} \tag{3.40}$$

Here p and q are pure number ratios derived from experimental data such as that in Figure 3.8. From (3.38) and the equations in section 3.6:

$$\mu_{101} = \frac{-1 + \sqrt{1 + \kappa^2 \sin^2 2\theta_{101}}}{2\kappa \sin^2 \theta_{101}} \tag{3.41}$$

$$\kappa \equiv p \frac{\mu_{103}}{\cos^2 \theta_{103} - \mu_{103}^2 \sin^2 \theta_{103}} \tag{3.42}$$

Here, θ_{101} and θ_{103} represent the physical angles of each facet with respect to the scanning plane, *i.e.* $\theta_{101} = -14^\circ + \psi$, and $\theta_{103} = 12.5^\circ + \psi$.

There is also an ambiguity here between a friction coefficient and its reciprocal, similar to the one slope solution of section 3.6. We choose the quadratic roots giving $\mu < 1$, which gives calibration results consistent with the calculated lever properties. Equation (3.42) expresses μ_{101} in terms of μ_{103}. From (3.39),

$$2q = (\frac{1}{\mu_{103}} + \mu_{103}) \sin 2\theta_{103} \frac{1}{p} - (\frac{1}{\mu_{101}} + \mu_{101}) \sin 2\theta_{101} \tag{3.43}$$

Now we can substitute (3.41) and (3.42) into (3.43) to eliminate μ_{101}. As the resulting expression is difficult to invert, we solve it numerically for the root such that $0 < \mu_{103} < 1$. With this solution, we find the calibration

$$\alpha = \frac{1}{W_o'(103)} \frac{\mu_{103}}{\cos^2 \theta_{103} - \mu_{103}^2 \sin^2 \theta_{103}} \tag{3.44}$$

Chapter 3 References

[1] G. Meyer and N. Amer, Appl. Phys. Lett. **57,** 2089 (1990).

[2] O. Marti, J. Colchero, and J. Mlynek, Nanotechnology **1,** 141 (1991).

[3] W. F. Kolbe, D. F. Ogletree, and M. B. Salmeron, Ultramicroscopy **42-44B,** 1113 (1992).

[4] Q. Dai, R. Vollmer, R. W. Carpick, D. F. Ogletree, and M. Salmeron, Rev. Sci. Instrum. **66,** 5266 (1995).

[5] Dr. M. Tortonese, Park Scientific Instruments Inc., Sunnyvale, CA (personal communication).

[6] Dr. R. Alley, Berkeley Sensors Group, Berkeley, CA (personal communication).

[7] J. E. Sader, I. Larson, P. Mulvaney, and L. R. White, Rev. Sci. Instrum. **66,** 3789 (1995).

[8] J. E. Sader and L. R. White, J. Appl. Phys. **74,** 1 (1993).

[9] J. M. Neumeister and W. A. Ducker, Rev. Sci. Instrum. **65,** 2527 (1994).

[10] U. D. Schwarz, P. Koster, and R. Wiesendanger, Rev. Sci. Instrum. **67,** 2560 (1996).

[11] D. F. Ogletree, R. W. Carpick, and M. Salmeron, Rev. Sci. Instrum. **67,** 3298 (1996).

[12] S. P. Timoshenko and J. N. Goodier, *Theory of Elasticity* (McGraw Hill, New York, 1987).

[13] J. E. Sader, Rev. Sci. Instrum. **66,** 4583 (1995).

[14] R. J. Warmack, X.-Y. Zheng, T. Thundat, and D. P. Allison, Rev. Sci. Instrum. **65,** 394 (1994).

[15] R. Lüthi, E. Meyer, H. Haefke, L. Howald, W. Gutmannsbauer, M. Guggisberg, M. Bammerlin, and H.-J. Güntherodt, Surf. Sci. **338,** 247 (1995).

[16] J. P. Cleveland, S. Manne, D. Bocek, and P. K. Hansma, Rev. Sci. Instrum. **64,** 403 (1993).

[17] T. J. Senden and W. A. Ducker, Langmuir **10,** 1003 (1994).

[18] A. Torii, M. Sasaki, K. Hane, and S. Okuma, Meas. Sci. Technol. **7,** 179 (1996).

[19] J. A. Ruan and B. Bhushan, Trans. ASME J. Tribology **116,** 378 (1994).

[20] Y. Q. Li, N. J. Tao, J. Pan, A. A. Garcia, and S. M. Lindsay, Langmuir **9,** 637 (1993).

[21] H. J. Butt and M. Jaschke, Nanotechnology **6,** 1 (1995).

[22] J. L. Hutter and J. Bechhoefer, Rev. Sci. Instrum. **64,** 1868 (1993).

[23] S. S. Sheiko, M. Möller, E. M. C. M. Reuvekamp, and H. W. Zandbergen, Phys. Rev. B **48,** 5675 (1993).

[24] R. W. Carpick, N. Agraït, D. F. Ogletree, and M. Salmeron, J. Vac. Sci. Technol. B **14,** 1289 (1996).

[25] RHK Inc., Rochester Hills, MI.

[26] J. Fu, Rev. Sci. Instrum. **66,** 3785 (1995).

[27] S. M. Hues, C. F. Draper, K. P. Lee, and R. J. Colton, Rev. Sci. Instrum. **65,** 1561 (1994).

[28] A. E. Holman, P. M. L. O. Scholte, W. C. Heerens, and F. Tuinstra, Rev. Sci. Instrum. **66,** 3208 (1995).

[29] Park Scientific Instruments Inc., Sunnyvale CA, USA.

[30] M. Binggeli and C. M. Mate, Appl. Phys. Lett. **65,** 415 (1994).

[31] J. Hu, X.-D. Xiao, D. F. Ogletree, and M. Salmeron, Surf. Sci. **327,** 358 (1995).

4. Atomic-Scale Stick-Slip

The observation of atomic-scale stick-slip behavior with contact mode AFM is both striking and quite general. It is also not fully understood. In this chapter, we consider this beautiful yet mysterious phenomenon in some detail, as it occurred throughout all of the friction measurements presented in further chapters. We consider our results in the context of other experimental and theoretical studies which will be reviewed here.

4.1 Macroscopic Stick-Slip

The term "stick-slip" must be used with caution: in general "stick-slip" refers to the behavior of a macroscopic contact which involves multiple contact asperities. For example, a creaking door hinge, a bowed violin string, screeching tires, and earthquakes are all examples of macroscopic stick-slip behavior. As well, stick-slip in micrometer-sized single asperity contacts with molecularly thin interlayers has been observed in SFA experiments[1]. A rich variety of phenomena are involved in these examples[2], but the unifying principle is that the friction force depends upon the relative tip-sample sliding velocity. Specifically, friction during sliding is lower than the friction when not sliding. If an increasing lateral stress is applied to an interface that is stuck together, then when the applied stress exceeds the static friction, sliding occurs and so friction is now lower. Initially, this leads to increasingly faster relaxation of the applied stress until it is no longer large enough to maintain sliding. The system is then "stuck" again and the cycle repeats itself. The behavior is influenced to varying degrees by factors such as the roughness/topology of the contacting surfaces, "creep"/strengthening of the interface during sticking, and velocity dependent effects particularly with viscous or visco-elastic materials. With AFM we are dealing exclusively with "atomic-scale stick-slip". In contrast to macroscopic stick-slip, the interface is atomically smooth, wear does not appear to occur, and the contact involves only

solid, elastic materials.

4.2 Stick-Slip at the Atomic Scale: Overview

Mate *et al.*'s pioneering paper measuring friction with AFM[3] for a tungsten tip on graphite showed that lateral forces exhibited stick-slip behavior with the periodicity of the graphite lattice. Since then, atomic-scale stick-slip behavior has been observed on a wide range of materials: from soft materials like stearic acid crystals (with a silicon nitride tip)[4] to a diamond tip on a diamond surface[5], the hardest and stiffest interface possible.

Typical atomic-scale stick-slip behavior is shown in Figure 4.1, for a silicon nitride tip on the surface of mica(0001). The image exhibits a periodic lattice. The line trace from the image shows that the lateral force starts from zero and builds up to some maximum lateral force. The tip is sticking to the surface throughout this portion of the measurement. The arrow indicates the occurrence of the first slip event. The tip then sticks again until the maximum lateral force is reached once more, and the next slip occurs, and so on. The periodicity of the slips is equal to 0.52±0.02 nm, which is equal to the lattice constant of

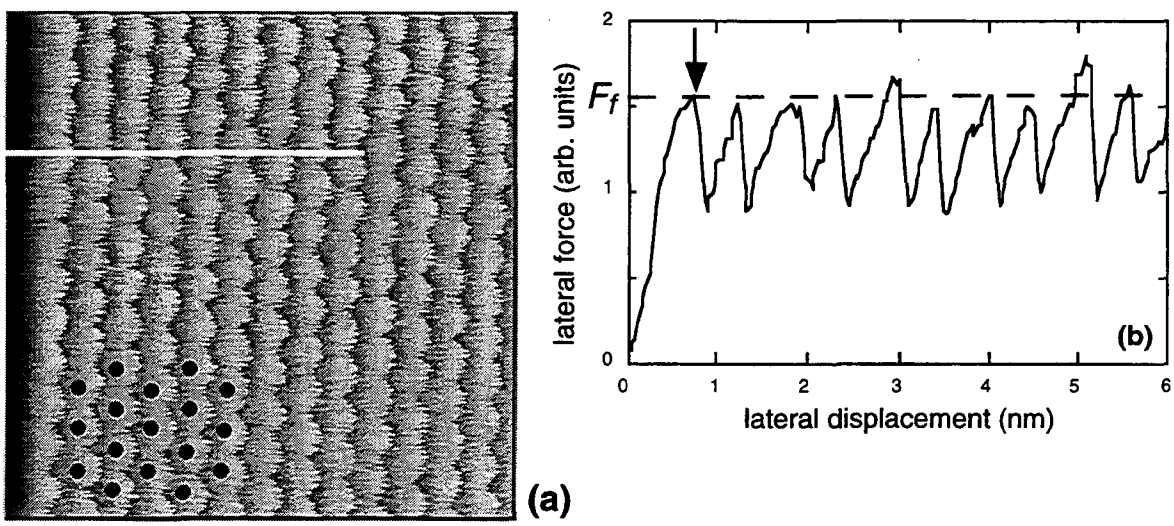

Figure 4.1 (a) 7.5 × 7.5 nm^2 lateral force image of the mica(0001) surface. The scan direction is from left to right. The black dots represent the repeat units of the mica lattice, whose periodicity coincides with the lateral forces. (b) Line trace of the section indicated in (a). The lateral force exhibits "stick-slip" behavior, where the lateral force builds up to some well-defined maximum value, and then quickly relaxes. During the relaxation, the tip slips by one unit cell. This behavior repeats itself with the lattice periodicity.

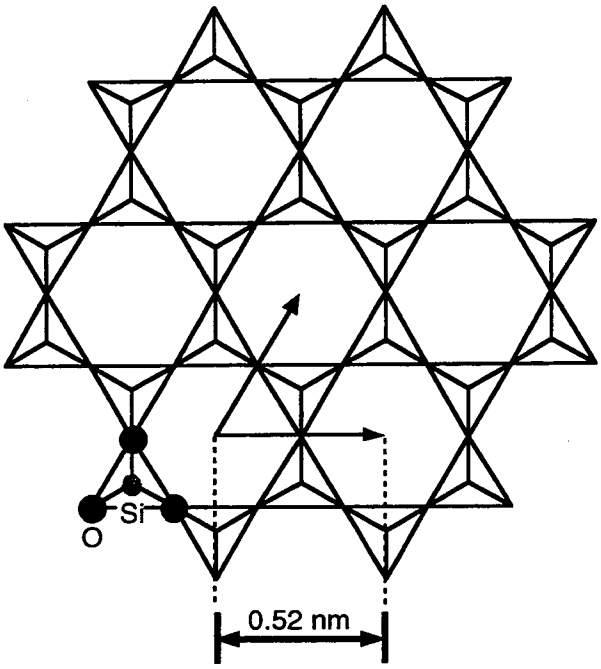

Figure 4.2 The surface structure of mica. SiO_4 tetrahedra point upward exposing rings of O atoms. The centers of the rings have a 0.52 nm periodicity. Not shown are potassium ions which sit in the center of the rings. A fraction of these ions are removed by the cleavage process, leaving an uneven distribution behind.

the mica surface. The mica surface structure is illustrated in Figure 4.2. We see in Figure 4.1 that there is a well-defined force, F_f, at which the tip slips. This is what we define as the friction force, and we will discuss its relation to the physical properties of the contact in the next two chapters.

There was, and still remains some confusion in this field regarding images showing lattice periodicity in the measured forces. The confusion partly stems from the fact that *topographic* images appear to be composed of rounded bumps with the periodicity of the lattice. Naturally, one is drawn to believe that the AFM is achieving true atomic resolution imaging of the surface, akin to an STM.

However, when the tip is in mechanical contact with a given sample, simple elastic contact mechanics shows that for typical tip radii, loads and elastic constants, the contact is not just a single atom. For example, a 20 nm radius silicon nitride tip (sharp by AFM standards) exerting a 1 nN load (relatively low by AFM standards) on a mica sample produces a contact area involving nearly 15 mica unit cells, as estimated using the Hertz theory which in fact neglects adhesion (further details of elastic contact mechanics will be given in the next chapter). Including the effect of tip-sample adhesion makes the contact area even larger and can ensure a substantial contact area even at the lowest possible applied loads. Contact-mode AFM therefore cannot possess single-atom resolution as with STM. This has several consequences: point defects are not imaged, and the lateral resolution of

features is limited by the contact area. We therefore make a careful distinction in terminology: an *atomic resolution* image is one where individual atoms and associated point defects, single adsorbates *etc.* are truly resolved. This is what is achieved in STM. An *atomic lattice resolution* image is one that displays the periodicity of the atomic lattice, like that shown in Figure 4.1, but is not an atom-by-atom image. In the next section we discuss the origin of this apparent topographic contrast.

In these experiments, there is no reason to expect that the tip atoms will be ordered. For example, atomic-scale stick-slip has been observed with tips made out of amorphous silicon nitride. Even if the tip atoms are ordered they will not necessarily be in a structure that is commensurate with the sample's lattice. Without a commensurate tip-sample interface, there would be no preferred relative positions for the tip to reside in, so smooth sliding would be expected. Perhaps at best, the tip-sample contact could be commensurate but with a large unit cell. The regular appearance of atomic-scale stick-slip is thus surprising.

The first few observations of this phenomenon in this field were acquired with highly anisotropic samples, such as graphite[3] and mica[6]. These layered materials exhibit strong covalent bonding within each layer, but the various layers are stacked together and held by weaker van der Waals' or electrostatic forces. These materials exhibit easy cleavage of the layers. It was initially suggested that the periodic forces occurred because a flake of the layered material had become attached to the tip. Therefore, the tip and sample structures were commensurate, and a periodic interaction would be expected. However, further measurements reported atomic-scale stick-slip on materials that did not possess such bonding anisotropy, such as NaCl. Atomic-scale stick-slip thus occurs between the tip itself and the sample. It therefore remains to be explained why, despite having a multiple atom contact and (most likely) a non-commensurate tip structure, the interaction between the tip and sample possesses the periodicity of the sample's atomic lattice, apparently for both lateral and normal forces.

Also unresolved is the question of stick-slip periodicity. Most accounts of stick-slip motion so far report that the forces have the symmetry of the surface lattice, *i.e.* there is *one* stick-slip event per surface unit cell. This has been generally observed even when the unit cell contains more than one atomic species, such as alkali halide surfaces, including KBr[7] and NaF[8,9]. There are some excpections. Multiple stick-slip events per unit cell were resolved for the large unit cell of Si(111)7 × 7 measured in UHV with tips coated with polytetrafluorethylene[10]. With KBr, Giessibl and Binnig[11] resolved maxima corresponding to the positions of both K^+ and Br^- ions in the normal force signal in UHV at 4.2K, so perhaps two stick-slip events per unit cell were taking place, although lateral forces were not measured in this experiment. Yet Lüthi *et al.*[7] observed only one stick-slip event per unit cell at room temperature with KBr in UHV. Recently, Fujisawa *et al.* observed stick-slip lateral forces on NaF[12] with the periodicity of the oppositely charged ions, not the lattice; *i.e.* there were *two* stick-slip events per unit cell. This was observed for an intermediate load range. Lateral forces with lattice periodicity were observed at lower and higher loads. It is therefore worth investigating materials with polyatomic unit cells to see if the stick-slip periodicity is determined by the symmetry of the lattice, or if multiple slip events take place per unit cell.

4.3 Instrumental Effects and Tip Trajectories

We first discuss the apparent "topography", or normal force variation observed in atomic lattice resolution images. To understand the observed forces, one must consider the instrumental response of the cantilever/optical beam setup. With the optical beam deflection technique, longitudinal (buckling) deformation of the cantilever cannot be distinguished *a priori* from vertical deflection due to normal forces, since both deflection modes change the angle of the cantilever in the same direction, as illustrated in Figure 4.3. Thus, one could mistake longitudinal cantilever deformation with a variation in the normal force. If the topographic feedback circuit is enabled, then the feedback circuit will respond to the fast variations in normal force with a finite time constant. The rapid slips will be smeared out to

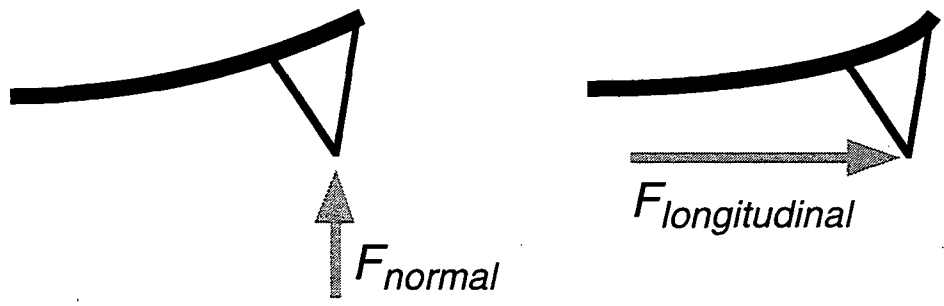

Figure 4.3 Normal forces and longitudinal forces (parallel to the cantilever's long axis) acting on the tip will both bend the end of the cantilever. Since the optical beam deflection method senses the angle of the end of the cantilever, these two types of forces are indistinguishable to the instrument without further investigation.

some extent, and the topographic image will appear to consist of rounded bumps. Considering the fact that some coupling between normal and lateral signal channels can also occur with the beam deflection scheme[13,14], we propose that this periodic frictional force interaction is responsible for *all* atomic-lattice contrast images obtained with *contact* AFM, including topographic images. To our knowledge, no observation of atomic lattice contrast *without* atomic-scale stick-slip behavior has yet been reported, while lateral force atomic lattice contrast, when it is measured, is often clearer than topographic contrast[10]. This simple argument takes for granted the details of the geometrical response of the cantilever beam. However, an exact description of the cantilever/instrumental response has been worked out by Ogletree *et al.*[15], confirming the result of the simple qualitative argument given here.

The reason that longitudinal buckling occurs is illustrated more clearly by carefully examining atomic-scale stick-slip images. Morita *et al.*[8] carried out a systematic study of atomic-scale stick-slip on various materials and discussed the details of the atomic scale slip motions that take place. Our observations and analysis are consistent with those of Morita *et al.* As seen in Figure 4.4, both lateral and longitudinal deformation of the cantilever occurs, due to two-dimensional frictional forces acting parallel to the sample surface.

Some distortion of the signals in Figure 4.4 occurs because of noise and unavoidable signal filtering by the acquisition electronics; oscilloscope traces confirm the stick-slips to be rapid jumps. By analyzing the signals, the path that the tip traces out across the sample can be determined (Figure 4.4(c)). Clearly, on an ordered sample, the tip (whose surface atoms are not necessarily ordered) generally prefers to reside in positions in registry with the sample lattice. The lever buckles and twists accordingly in response to the tip's motion of searching for lattice positions.

In summary, the AFM tip is not smoothly tracing out individual atomic corrugations as in STM, but instead the relative tip-sample motion is *discontinuous* and involves frictional forces in both the lateral and longitudinal directions with respect to the cantilever's axis.

4.4 Theoretical Approaches

Several theoretical efforts to explain and model atomic-scale stick-slip behavior in the context of force microscopy have appeared in the literature. These can be divided into semiclassical simulations/calculations[16-28], and molecular dynamics simulations[29-35]. The semiclassical models primarily attempt to explain the *mechanics* of stick-slip behavior. The starting point for these models is the Tomlinson model proposed more than five decades ago[36]. Some of these model the tip as a single atom or at least a single entity without internal degrees of freedom[16,21-23,26,27], although multiple atom tips have also been considered[17,25,28]. A periodic interaction potential is assumed to exist between this "tip" and the sample, simply because this is consistent with the experimental results. The important question of how this potential arises is not dealt with in these models.

In most cases the scanning process is carried out adiabatically, *i.e.,* the system is assumed to be in equilibrium at each step of the simulation, since typical AFM scanning velocities are much smaller than the sound velocities of the materials. The total interaction potential is sketched in Figure 4.5. When scanning, the lateral displacement between the lever and the sample is increased. The "tip" initially resides in a potential minimum that is

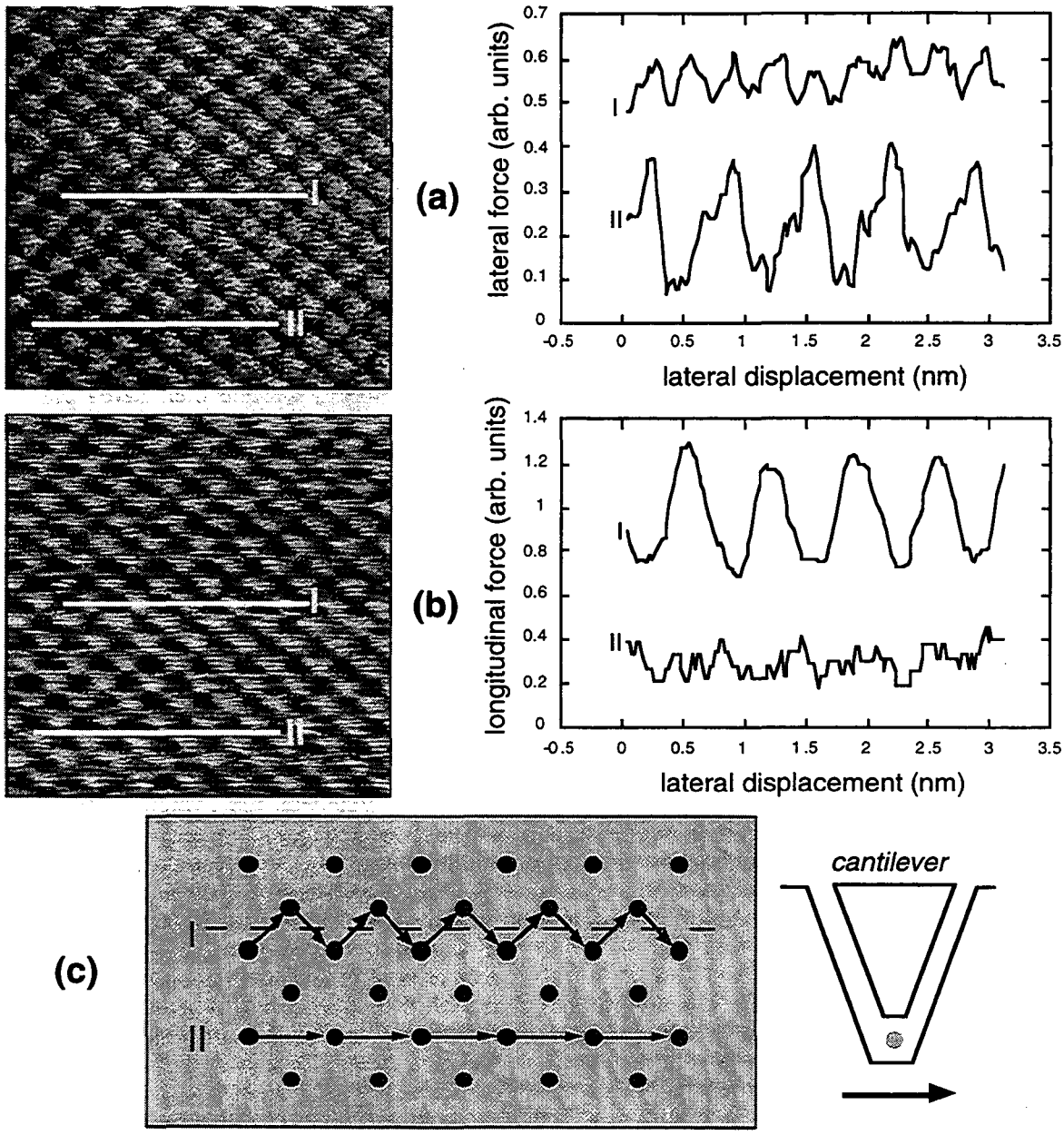

Figure 4.4 5×5 nm^2 image of NaCl(001) in UHV. (a) Lateral force image (left) and line traces (right). (b) Simultaneous longitudinal force image (left) and line traces (right). (c) Reconstructed tip trajectories. Circles represent surface unit cell positions, not individual ions. The cantilever's orientation is also shown. Twisting due to lateral forces and buckling due to longitudinal forces exhibit the lattice periodicity. In trace I, the tip is positioned between two lattice rows. The lever buckles and twists as the tip zigzags across the surface so that it always remains in registry with the surface lattice. In trace II, the tip is positioned along a lattice row. Consequently, in (b) the lever does not need to buckle for the tip to remain in registry, and in (a), half as many lateral stick-slip events occur.

determined by the tip-sample interaction. Finite static friction due to the tip-sample interaction inhibits sliding of the tip, and so elastic energy is built up in the cantilever and, as Colchero *et al.* have appropriately pointed out[27], in elastic deformation of the tip-sample contact itself (this will be discussed further in Chapter 6). The total energy of the system consists of the interaction energy and the elastic energy stored in the lever and the contacting materials. Eventually a critical point is reached where the elastic strain energy eliminates the potential minimum. Relative slip between tip and sample then takes place. The lever and the contact quickly relax, releasing energy, and the motion is brought to a stop as the tip finds a new potential minimum, one unit cell over. The phonons generated in this process in the tip and sample carry energy away from the interaction region; energy has thus been dissipated. Since phonon frequencies are much higher than typical AFM scanning frequencies (by a factor of $\sim 10^{11}$), this relaxation occurs very quickly. The collective results of these semiclassical models are as follows:

- the atomic-scale stick-slip instability can be interpreted as the system ("tip" and sample) residing in or searching for total potential energy minima, where the energy is the sum of the tip-sample interaction potential and elastic energy stored in the cantilever and contact.

- the atomic-scale stick-slip periodicity reflects the periodicity of the interaction potential.

- weak springs and strong tip-sample interactions are required to produce the atomic-scale stick-slip instability. It has been suggested that if this is not the case, then this instability can be prevented and frictionless sliding can occur[16,18,33,37,38]. However, this neglects other velocity-dependent forms of frictional dissipation, such as electronic contributions[39-43]. More importantly, it neglects the inherent compliance of the contact itself which will always be present. Contact compliance will be discussed further in Chapter 6.

- the two-dimensional stick-slip effects observed in experimental images can be

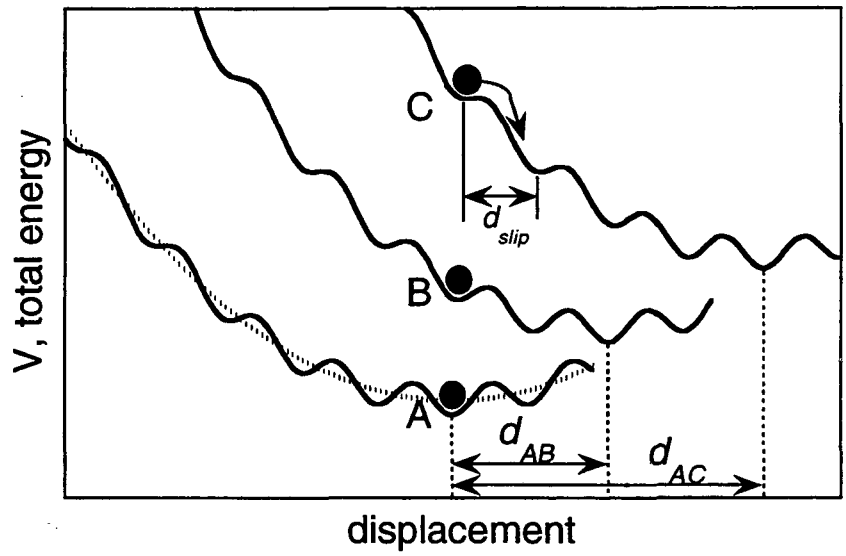

Figure 4.5 A one-dimensional "atomic Tomlinson model". Total energy V is plotted *vs.* displacement for an AFM in three positions. A single point potential is assumed for the tip. The atomic periodicity of the tip-sample interaction is superposed upon the parabolic elastic strain energy (dotted line) of the cantilever and the contact. The circle represents the position of the tip. The tip is initially located at point A, where the tip resides in a local energy minimum ($\partial V/dx = 0$, $\partial^2 V/\partial x^2 > 0$). At point B, after the lever has been displaced by d_{AB} with respect to the sample, the tip remains in a local minimum. At point C, the system becomes unstable ($\partial V/dx = \partial^2 V/\partial x^2 = 0$) and the tip rapidly slips over by one atomic position. The potentials are offset vertically from one another and cropped for clarity.

reproduced in these simulations[7,19,21,22,24,26], including observable effects in the images due to anisotropy in the cantilever spring constants (lateral *vs.* longitudinal)[19,21,23,24,26].

- the energy dissipated will be distributed amongst the substrate, tip and cantilever depending on their relative stiffness[27], with the more compliant components dissipating more energy.

- the atoms at the interface can be distorted from their equilibrium positions by the interfacial potential[17,25,28].

Atomic-scale stick-slip has also been produced in various molecular dynamics simulations. For example, simulations have been performed for ordered hydrogen-terminated diamond surfaces sliding together[29,30], and a silicon tip/surface pair[34,35,44].

These simulations provide local pictures of the vibrational motion and energy dissipation generated during atomic stick-slip motion, showing that excitations are highly localized in the contact zone.

Sørensen *et al.*[31] simulated Cu tips sliding on Cu surfaces. Wearless atomic stick-slip occurred for a (111)-terminated tip sliding on a (111) surface. The bottom layer of the tip (9×9 atoms) were shown to slip via a dislocation mechanism. The tip atoms initially reside in surface FCC positions. During the rapid slip, tip atoms start to jump from FCC to HCP sites to relieve lateral strain. The slipped and unslipped atoms are separated by a dislocation which propagates through the contact. Variations with scan velocity and relative orientation were also probed. Friction was observed to decrease with increasing scan velocity. At higher velocity, more phonons are excited during a slip and can promote subsequent slip events.

The lack of experimental control or even knowledge of the tip atomic structure makes comparison with these simulations challenging but not impossible. Another serious difference is the gap in time scale and velocity of these simulations - typical MD simulation velocities are 10^0 - 10^2 m/s *vs.* typical AFM experimental velocities of 10^{-7} to 10^{-4} m/s. Unfortunately, these simulations have yet to shed light on exactly how and why a non-commensurate interface produces a periodic interaction, although some of these studies suggest that the tip atoms may be pulled into registry with the surface lattice by interfacial forces.

4.5 Experiments

Various samples with different lattice constants were imaged in this experiment. Sample cleaving and measurements were performed in UHV, with some measurements also performed in air. The materials, the observed stick-slip periodicity, and the lattice constant of these materials is listed in Table 4.1. In some cases, measurements were performed above or below room temperature, and different tip materials were used.

The main observation is that atomic-scale stick-slip occurs on all of these materials.

Table 4.1 Periodicity of atomic-scale stick-slip measurements.

Sample	Surface Lattice Constant (nm)	Stick-Slip Periodicity (nm)	Notes
mica(0001)	0.520	0.52±0.02	Si, Si_3N_4, and Pt-coated tips, 100-300K
MoS_2(0001)	0.316	0.31±0.01	Si tip, 440K
NaCl(001)	0.398	0.40±0.01	Si_3N_4 tip
KBr(001)	0.467	0.49±0.03	Si_3N_4 tip
KCl(001)	0.445	0.44±0.02	Si_3N_4 tip
KF(001)	0.378	0.39±0.02	Si_3N_4 tip

Since this involves a range of surface structures, elastic properties, tip materials and temperatures, atomic-scale stick-slip is therefore a rather general phenomenon. The details of these measurements are discussed below.

4.5.1 Layered Materials

Mica and MoS_2 are highly anisotropic materials. MoS_2 consists of layers of in-plane covalently bonded S-Mo-S species. The layers are held together by weak van der Waals' forces, allowing easy cleavage exposing the (0001) plane. Using a Si cantilever, stick-slip forces with the periodicity of the surface lattice were observed, consistent with observations by Morita *et al*[8]. These stick-slip forces lead to apparent topographic lattice resolution, which was presented in Chapter 2, Figure 2.6.

Mica consists of covalently bonded alumina-silicate layers that are negatively charged. Layers are held together electrostatically by K^+ ions which sandwich the alumina-silicate layers. The exact chemical formula is $KAl_2(AlSi_3)O_{10}(OH)_2$ The surface structure is illustrated in Figure 4.2. The surface layer consists of SiO_4 tetrahedra that point upwards, forming rings of O atoms. In the bulk structure, the K^+ ions reside in the centers of the rings. Ideally, cleavage removes half of the K^+ layer, although studies have shown

that these ions are unevenly distributed and only weakly ordered[45,46]. These weakly bound species may be displaced by the AFM tip during scanning, although the exact structure both with and without the AFM tip present is in fact unknown. Measurements in both air and UHV at and below room temperature were acquired. Si, Si_3N_4 and Pt-coated tips all exhibited stick-slip forces with the surface lattice periodicity. An example was shown in Figure 4.1.

4.5.2 Alkali Halides

Alkali halide surfaces are relatively inert because of the closed-shell nature of the ionic bonding. Sample cleavage results in atomically flat terraces often several hundred nm wide or more.

The lattice constants of the materials are listed in Table 4.1. These materials form a FCC lattice with a basis of two atoms, the cation and anion, known as the "rocksalt" structure. The surface structure is illustrated in Figure 4.6. One can think of the ions as being packed like billiard balls whose radii are equal to the respective ionic radii.

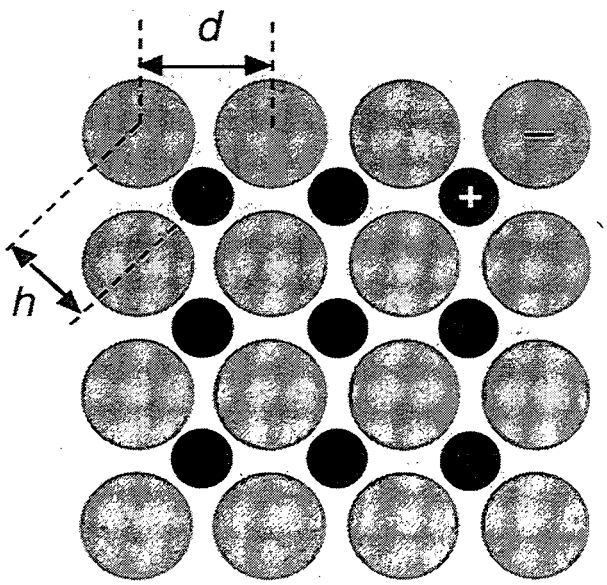

Figure 4.6 The rocksalt surface structure consists of alternating rows of cations and anions. The lattice periodicity *d* and the nearest-neighbor spacing *h* are shown.

Four (001) alkali halide surfaces were studies; KF, KCl, KBr and NaCl. Once in UHV, crystals were cleaved using a knife-edge, producing an optically flat (001) plane. All measurements were performed at room temperature using Si_3N_4 cantilevers. Measurements in air with NaCl were also performed.

Atomic lattice resolution lateral force images of all three materials were obtained. An example with KF is presented in Figure 4.7, and NaCl was

shown in Figure 4.4. The images for KCl and KBr are qualitatively similar to these. The lateral force images display periodic stick-slip behavior with periodicities of 0.39 ± 0.02 nm for KF, 0.44 ± 0.02 nm for KCl, 0.49 ± 0.03 nm for KBr, and 0.40 ± 0.01 nm for NaCl. In all three cases, the stick-slip exhibits the lattice periodicity *d* of each material (see Figure 4.6). This was consistently observed over a range of low loads for each material, typically from just before the pull-off point to a few nN positive load. At higher positive loads, the contrast tended to reduce. The stick-slip rows were observed to shift laterally across a monatomic step by half the row spacing, consistent with the rocksalt structure.

Therefore, at all loads where periodic stick-slip behavior occurs, the lattice periodicity is observed and is due to the two-dimensional frictional forces between tip and

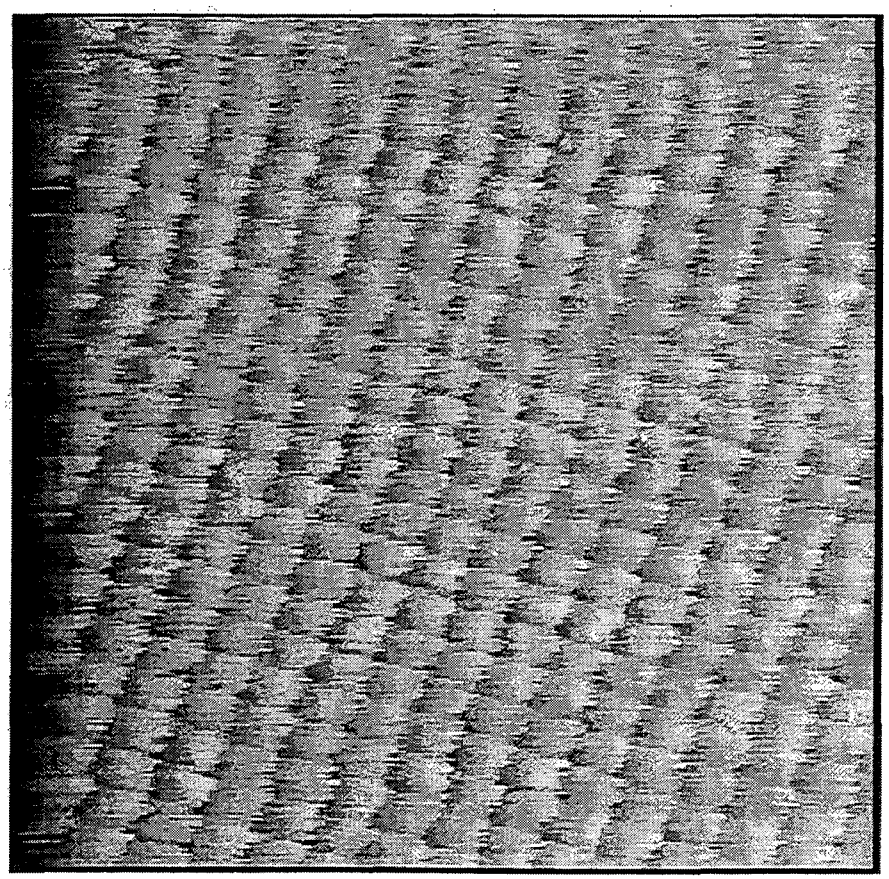

Figure 4.7 7.5 × 7.5 nm^2 lateral force image of KF(001). The scan direction is left to right. The stick-slip response has the periodicity of the KF(001) lattice, 0.39±0.02 nm.

sample.

4.6 Conclusions and Outstanding Issues

We have observed atomic-scale stick-slip with a variety of tip and sample materials, for a range of cantilever force constants, temperatures, and for samples with both isotropic and anisotropic bonding. Atomic-scale stick-slip was observed both in UHV and ambient experimental conditions. For the particular materials investigated, stick-slip forces exhibited the periodicity of the surface lattice. It is clear that atomic-scale stick-slip is a general phenomenon for a nanometer-sized contact, and is an important mechanism leading to energy dissipation.

Several issues remain outstanding. The question of how a (probably) non-commensurate interface so commonly exhibits stick-slip with the sample's lattice periodicity has not been explained. That stick-slip occurs so commonly suggests that in a nanometer-sized contact, the tip atoms may be distorted sufficiently by interfacial forces to pull them into at least partial registry with the sample's lattice.

Micrometer-scale stick-slip behavior is observed in SFA experiments[47-49] but a transition to smooth wearless sliding occurs at higher velocities. No reports of stick-slip to smooth sliding transitions have been made with AFM, probably due to the limited scan speeds. It would be interesting to quantify this limit by attempting faster AFM experiments. This would require instrumental modification to allow high-frequency scanning and data acquisition.

If FFM measurements involve stick-slip motion, then we must keep in mind that we are dealing with *static* friction. The force of interest is thus the lateral force for which the tip slips across the surface, *i.e.,* the *maximum* force measured in a stick-slip plot like that shown in Figure 4.1. The following chapters examine the physics that determines this force.

Chapter 4 References

[1] A. D. Berman, W. A. Ducker, and J. N. Israelachvili, Langmuir **12,** 4559 (1996).

[2] *Physics of Sliding Friction*, edited by B. N. J. Persson and E. Tosatti (Kluwer, Dordrecht, 1996).

[3] C. M. Mate, G. M. McClelland, R. Erlandsson, and S. Chiang, Phys. Rev. Lett. **59,** 1942 (1987).

[4] H. Takano and M. Fujihira, J. Vac. Sci. Technol. B **14,** 1272 (1996).

[5] G. J. Germann, S. R. Cohen, G. Neubauer, G. M. McClelland, H. Seki, and D. Coulman, J. Appl. Phys. **73,** 163 (1993).

[6] R. Erlandsson, G. Hadziioannou, C. M. Mate, G. M. McClelland, and S. Chiang, J. Chem. Phys. **89,** 5190 (1988).

[7] R. Lüthi, E. Meyer, M. Bammerlin, L. Howald, H. Haefke, T. Lehmann, C. Loppacher, H.-J. Güntherodt, T. Gyalog, and H. Thomas, J. Vac. Sci. Technol. B **14,** 1280 (1996).

[8] S. Morita, S. Fujisawa, and Y. Sugawara, Surf. Sci. Rep. **23,** 3 (1996).

[9] L. Howald, R. Lüthi, E. Meyer, G. Gerth, H. Haefke, R. Overney, and H.-J. Güntherodt, J. Vac. Sci. Technol. B **12,** 2227 (1994).

[10] L. Howald, R. Lüthi, E. Meyer, and H.-J. Güntherodt, Phys. Rev. B **51,** 5484 (1995).

[11] F. J. Giessibl and G. Binnig, Ultramicroscopy **42-44,** 281 (1991).

[12] S. Fujisawa, Y. Sugawara, and S. Morita, Philos. Mag. A, Phys. Condens. Matter Struct. Defects Mech. Prop. **74,** 1329 (1996).

[13] D. F. Ogletree, R. W. Carpick, and M. Salmeron, Rev. Sci. Instrum. **67,** 3298 (1996).

[14] R. Lüthi, E. Meyer, H. Haefke, L. Howald, W. Gutmannsbauer, M. Guggisberg, M. Bammerlin, and H.-J. Güntherodt, Surf. Sci. **338,** 247 (1995).

[15] D. F. Ogletree, R. W. Carpick, and M. Salmeron, in preparation (1997).

[16] D. Tomanek, W. Zhong, and H. Thomas, Europhys. Lett. **15,** 887 (1991).

[17] J. B. Sokoloff, Thin Solid Films **206,** 208 (1991).

[18] G. M. McClelland and J. N. Glosli, in *Fundamentals of Friction*, edited by I. L. Singer and H. M. Pollock (Kluwer, Dordrecht, 1992), p. 405.

[19] J. Kerssemakers and J. T. M. De Hosson, Appl. Phys. Lett. **67,** 347 (1995).

[20] T. Gyalog, M. Bammerlin, R. Lüthi, E. Meyer, and H. Thomas, Europhys. Lett. **31,** 269 (1995).

[21] N. Sasaki, K. Kobayashi, and M. Tsukada, Jpn. J. Appl. Phys. 1, Regul. Pap. **35,** 3700 (1996).

[22] H. Hölscher, U. D. Schwarz, and R. Wiesendanger, Europhys. Lett. **36,** 19 (1996).

[23] T. Gyalog and H. Thomas, in *Physics of Sliding Friction*, edited by B. N. J. Persson and E. Tosatti (Kluwer Academic Publishers, Dordrecht, 1996), p. 403.

[24] J. Kerssemakers and J. T. M. De Hosson, J. Appl. Phys. **80,** 623 (1996).

[25] M. Weiss and F.-J. Elmer, Phys. Rev. B **53,** 7539 (1996).

[26] N. Sasaki, K. Kobayashi, and M. Tsukada, Surf. Sci. **357-358,** 92 (1996).

[27] J. Colchero, A. M. Baro, and O. Marti, Trib. Lett. **2,** 327 (1996).

[28] T. Gyalog and H. Thomas, Europhys. Lett. **37,** 195 (1997).

[29] J. A. Harrison, C. T. White, R. J. Colton, and D. W. Brenner, Phys. Rev. B **46,** 9700 (1992).

[30] M. D. Perry and J. A. Harrison, J. Phys. Chem. **99,** 9960 (1995).

[31] M. R. Sørensen, K. W. Jacobsen, and P. Stoltze, Phys. Rev. B **53,** 2101 (1996).

[32] A. L. Shluger, R. T. Williams, and A. L. Rohl, Surf. Sci. **343,** 273 (1995).

[33] G. M. McClelland, in *Adhesion and Friction, Springer Series in Surface Science*; *Vol. 17*, edited by M. Grunze and H. J. Kreuzer (1989), p. 1.

[34] U. Landman, W. D. Luedtke, and A. Nitzan, Surf. Sci. Lett. **210,** L177 (1989).

[35] U. Landman, W. D. Luedtke, and M. W. Ribarsky, J. Vac. Sci. Technol. A **7,** 2829 (1989).

[36] G. A. Tomlinson, Phil. Mag. **7,** 905 (1929).

[37] J. B. Sokoloff, Phys. Rev. Lett. **71,** 3450 (1993).

[38] J. B. Sokoloff, Phys. Rev. B **52,** 7205 (1995).

[39] C. Daly and J. Krim, Surf. Sci. **368,** 49 (1996).

[40] B. N. J. Persson, Comm. Cond. Matt. Phys. **17,** 281 (1995).

[41] J. B. Sokoloff, Phys. Rev. B **52,** 5318 (1995).

[42] B. N. J. Persson and A. I. Volokitin, J. Chem. Phys. **103,** 8679 (1995).

[43] B. N. J. Persson and A. Nitzan, Surf. Sci. **367,** 261 (1996).

[44] U. Landman and W. D. Luedtke, in *Scanning Tunneling Microscopy III : Theory of STM and Related Scanning Probe Methods*, edited by R. Wiesendanger and H.-J. Guntherodt (Springer-Verlag, Berlin, 1993), p. 207.

[45] R. Gerlach, G. Polanski, and H.-G. Rubahn, Surf. Sci. **352-354,** 485 (1995).

[46] G. Brusdeylins and D. Schmicker, Surf. Sci. **331-333,** 237 (1994).

[47] H. Yoshizawa, Y.-L. Chen, and J. Israelachvili, Wear **168,** 161 (1993).

[48] G. Reiter, A. L. Demirel, J. Peanasky, L. L. Cai, and S. Granick, J. Chem. Phys. **101,** 2606 (1994).

[49] G. Reiter, A. L. Demirel, and S. Granick, Science **263,** 1741 (1994).

5. Contact, Friction and Adhesion with Mica Substrates

5.1 Introduction

In the previous chapter we showed that the AFM tip-sample contact exhibits unique atomic-scale stick-slip behavior. We saw that there is a well-defined critical lateral force at which slip occurs (see Figure 4.1 of Chapter 4). We would like to know what determines the value of this force - how does it depend upon the load, the structure and chemistry of both the tip and sample, and other experimental conditions. We would also like to know the size of the contact, *i.e.* how many atoms are involved in the contact. To this end, we examined how this critical lateral force depends upon the applied load for mica substrates with various tips, and compared the results to predictions of tip-sample contact area derived from continuum mechanics[1,2]. We thus begin with a discussion of the existing theories of contact mechanics, then describe the experiments performed.

5.2 Theoretical Background - Continuum Contact Mechanics

Contact mechanics describes the deformations, displacements and stresses which occur when materials are brought in contact. This field is comprehensively reviewed by Johnson[3]. We shall concentrate on theories that assume the conditions are elastic, *i.e.* all deformations are reversible. A single contact is formed between a sphere and a plane, who possess isotropic elastic properties. These are continuum theories which neglect the atomic structure of the materials. Furthermore, these particular theories do not take into account the tangential stresses that will be present due to frictional forces during sliding, but this has been shown for the SFA to be a small effect for low sliding velocities[4]. For the purpose of this discussion, we shall ignore these corrections.

5.2.1 Hertz Theory

The pioneering work on this topic was performed by Hertz[5] in the 19th century. He solved the contact mechanics problem for two spheres of radius R_1 and R_2 assuming only elastic deformations of the materials, thus there is no interpenetration of the surfaces, and no attractive forces acting between the surfaces. The interaction force is sketched in Figure 5.1. The spheres are actually treated as paraboloids with curvature radii R_1 and R_2 respectively, which is a valid approximation if the contact radius is much less than the curvature radii. The symmetry of the problem leads to a flat, circular contact area between the materials when they are pushed together. His result leads to the following relation

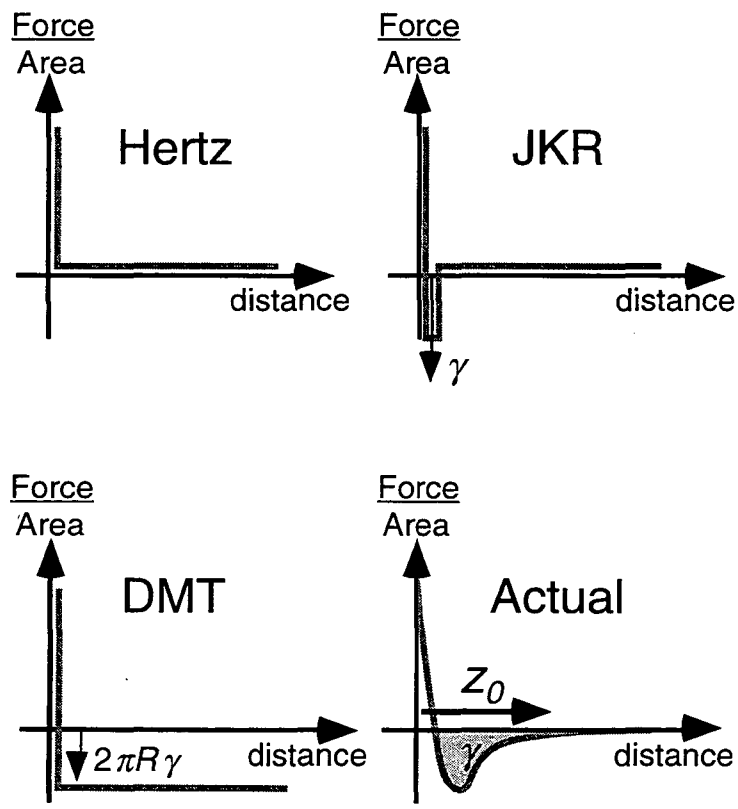

Figure 5.1 Interaction forces (normalized per unit area) for the Hertz, JKR, and DMT models, compared to a realistic interaction. There is no attractive force in the Hertz model, only hard wall repulsion at contact. The JKR model includes short range adhesion which is essentially a delta function with strength γ. The DMT model assumes a long-range attractive force. For an actual interaction force, the integral of the force-distance attractive well corresponds to the work of adhesion, γ.

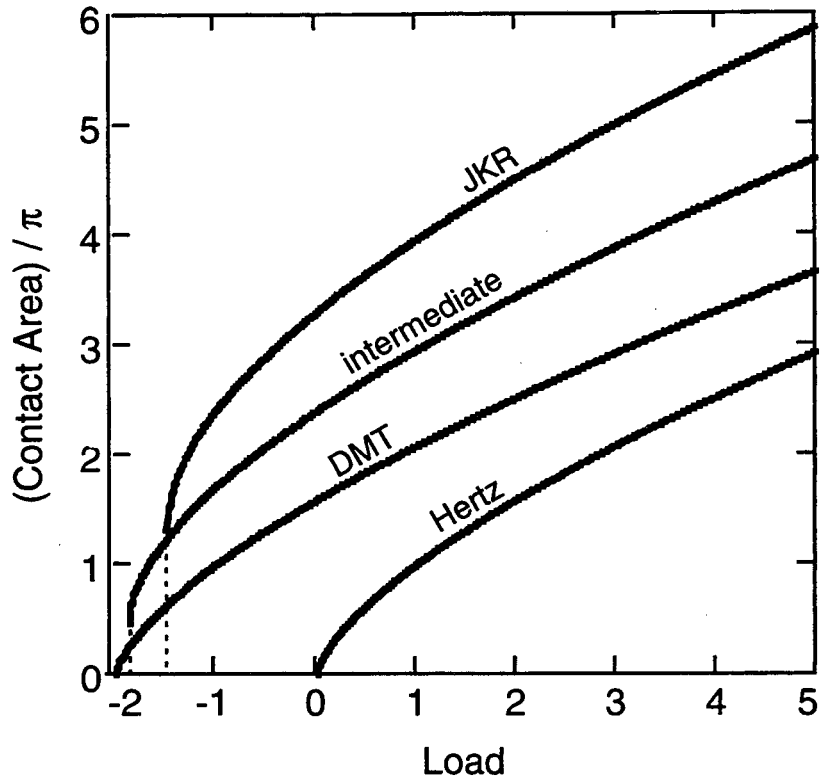

Figure 5.2 The Hertz area-load curve, and the JKR-DMT transition, plotted in dimensionless units (R=1, K=1, $\pi\gamma = 1$). The exact relationship between contact area and load depends upon the range of attractive surface forces. Area-load curves for the JKR limit, the DMT limit and an intermediate case are shown. All of these approach the Hertz curve in the limit $\gamma \rightarrow 0$ (no adhesion). Adhesion increases the contact area from the Hertz case for a given load by an amount dependent upon the range of attractive forces.

between contact area and load:

$$A = \pi \cdot \left(\frac{R \cdot L}{K} \right)^{2/3} \tag{5.1}$$

where A is the contact area, L is the externally applied load, R is the combined curvature radius

$$R = \left(\frac{1}{R_1} + \frac{1}{R_2} \right)^{-1} \tag{5.2}$$

and K is the combined elastic moduli of the materials, given by

$$K = \frac{4}{3} \cdot \left(\frac{1 - \nu_1^2}{E_1} + \frac{1 - \nu_2^2}{E_2} \right)^{-1} . \tag{5.3}$$

Here E_1 and E_2 are the respective Young's Moduli, and ν_1, ν_2 the respective Poisson ratios.

Equation (5.1) is also valid in the case of a tip of radius R and a flat sample, since $R_1 \rightarrow R$ and $R_2 \rightarrow \infty$. The Hertz area-load curve is plotted in Figure 5.2. We see that for an elastic single asperity contact between a round tip and a flat sample, the contact area is a non-linear function of load.

5.2.2 JKR Theory

The Hertzian model does not take into account attractive forces between the contacting surfaces. The Johnson-Kendall-Roberts (JKR) theory[6] considers the effect of finite surface energy. In particular, the theory calculates the increase in contact area that results from the elastic bodies deforming to accommodate their mutual attraction, so that the deformations are no longer perfectly Hertzian. As with the Hertz theory, the JKR theory applies to the case of two spheres (approximated as paraboloids) in contact. The model can be extended to more general shapes[7,8]. The validity of the JKR model has been verified by SFA experiments[9].

The interface is considered to possess an energy per unit area $\gamma = \gamma_1 + \gamma_2 - \gamma_{12}$, where γ_1 and γ_2 are the respective surface energies and γ_{12} the interfacial energy. γ is equivalent to the Dupré energy of adhesion which corresponds to the work per unit area required to separate the surfaces from contact to infinity. As such, the parameter γ effectively encompasses all attractive interaction forces. However, the JKR approximation assumes that all the interaction forces have zero range, as sketched in Figure 5.1. In other words, the surfaces gain an energy per unit area γ if they touch, but not if they are separated by an infinitesimal amount or more. We shall discuss the limitations of this approximation furhter below.

In the JKR theory, the contact area A as a function of externally applied load L is given by:

$$A = \pi \frac{R^{2/3}}{K^{2/3}} \left(L + 3\pi\gamma R + \sqrt{6\pi\gamma R L + (3\pi\gamma R)^2} \right)^{2/3} . \qquad (5.4)$$

The JKR area-load curve is plotted in Figure 5.2. The Hertz formula is recovered by setting $\gamma = 0$. In the JKR theory, the contact zone is significantly deformed from the Hertzian case, particularly by the formation of a neck-like structure at the contact zone edge, as depicted in Figure 5.3. Significant tensile stresses exist within this region. The energy cost of these stresses is paid for by the gain of interfacial energy due to increased contact area. In fact, the calculated tensile stress diverges to infinity at the contact zone edge. The authors account for this unphysical result by predicting that real materials will exhibit small relaxations at the contact zone edge which does not significantly affect the rest of the contact.

The theory predicts that a finite negative load is required to separate the surfaces. This value is often referred to as the critical load, L_c, and is given by:

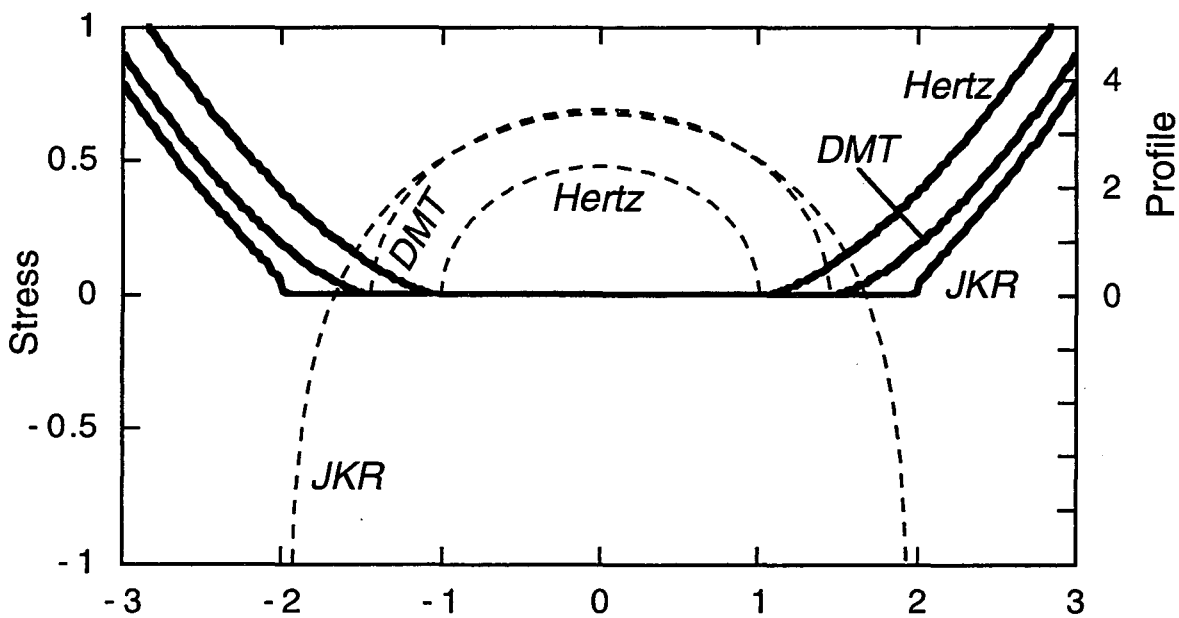

Figure 5.3 Contact stresses (dotted lines) and contact profile (solid lines) for the Hertz, DMT, and JKR models for the same applied load, plotted using non-dimensional units (R=1, K=1, $\pi\gamma$=1, applied load = 1) for two spheres in contact. For clarity, only the upper sphere is shown. In the DMT model, the Hertz profile is preserved but with a higher effective load due to long-range adhesion. In the JKR model, short-range adhesion significantly distorts the sphere's profile in and near the contact zone. This leads to a diverging tensile stress at the contact zone edge.

$$L_c = -\frac{3}{2}\pi\gamma R \tag{5.5}$$

At the critical load, a finite contact area exists. We shall refer to this area as the critical area, A_C, and is given by:

$$A_c = \pi\left(\frac{3\pi\gamma R^2}{2K}\right)^{2/3} \tag{5.6}$$

5.2.3 DMT Theory

The problem of contact mechanics in the presence of adhesion is treated by a significantly different approach by Derjaguin, Müller and Toporov (DMT)[10]. Unlike the JKR case, the DMT theory assumes that the shape of the contact is not affected by the interfacial forces. Rather, the overall Hertzian deformation profile is maintained, but the contact area is increased, as depicted in Figure 5.3. Adhesion forces effectively act as an extra external load, as described in Figure 5.1. The DMT area-load relation is given by:

$$A = \pi\frac{R^{2/3}}{K^{2/3}}\left(L + 2\pi\gamma R\right)^{2/3} \tag{5.7}$$

which is also sketched in Figure 5.2. The critical load L_c in the DMT case is larger than for the JKR case,

$$L_c = -2\pi\gamma R \tag{5.8}$$

and the contact area goes to zero at the critical load. Unlike the JKR case, stresses are finite at the contact zone edge. There is only a small tensile stress outside of the contact zone.

5.2.4 The JKR-DMT Transition

The DMT and JKR theories describe vastly different contact properties. In fact, a rather acrimonious debate broke out in the literature regarding which theory is correct. This was resolved with the realization that both theories are correct, but for different situations. Compliant materials with strong, short-range adhesion forces and large radii will behave more like a JKR contact, whereas stiff materials with lower, longer-range adhesion forces and small radii will behave more like a DMT contact. Cases that are in between will also occur, as illustrated in Figure 5.2.

Thus, the JKR and DMT theories are actually limiting cases of a spectrum of contact mechanics behavior. The transition between these two limits is discussed by Johnson[11], as well as by Maugis[12], and Müller *et al*[13]. The following dimensionless parameter, following on a proposal of Tabor[14], determines the contact behavior with respect to these limits[15]:

$$\mu_T = \left(\frac{16R\gamma^2}{9K^2 z_0^{\,3}} \right)^{1/3} \tag{5.9}$$

where z_O represents the effective range of adhesion. To be firmly in the JKR limit, μ_T should be about 5 or greater, whereas μ_T <0.1 implies the DMT limit. Values in between correspond to the "transition region". The symbol μ_T is often called "Tabor's Parameter" and is not to be confused with the friction coefficient μ. As well, there are different conventions in the literature for the exact form of μ_T, which are listed by Greenwood[15]. Unfortunately, z_O is a property of the interfacial forces and is thus not necessarily known. It is therefore difficult to know *a priori* which contact mechanics regime will be appropriate for a given interface.

5.2.5 The Relation to Friction

Now we will discuss how to apply a contact mechanics theory to the study of friction. We make the fundamental assumption that friction is proportional to the area of contact. SFA experiments with contacting mica surfaces that are either bare or with molecular layers between have shown that in the absence of wear, the frictional force F_f is directly proportional to the contact area[4,16], *i.e.*

$$F_f = \tau \cdot A \tag{5.10}$$

where τ is the interfacial shear strength.

Let us assume the JKR theory applies for the contact. Thus, there will be a finite frictional force at the critical load, which we shall call the critical friction force, F_c, given by:

$$F_c = \tau \cdot A_c = \tau \cdot \pi \left(\frac{3\pi\gamma R^2}{2K} \right)^{2/3} \quad . \tag{5.11}$$

Using the assumption of equation (5.10) and the JKR equation, we can write the equation for friction as a function of load in the following compact non-dimensional form after completing the square:

$$\hat{F}_f = \left(1 + \sqrt{1 + \hat{L}}\right)^{4/3} \tag{5.12}$$

where the load and friction have been parametrized in terms of the critical load and critical friction:

$$\hat{F}_f = \frac{F_f}{F_c} \text{ and } \hat{L} = \frac{L}{L_c} \quad . \tag{5.13), (5.14}$$

The above discussion shows that although four physical quantities are involved in the friction-load equation (interfacial energy, tip radius, combined elastic modulus, and shear strength), there are only two independent parameters in the equation: L_c (equation (5.5)) and F_c (equation (5.11)). Thus, the entire shape of the curve is fixed, and these two quantities (or any other single pair of points (L, F) on the curve) only determine the scaling of the axes. Therefore, it will be easy to test the validity of our assumption that $F_f = \tau \cdot A$. If the assumption is valid, and if R and K are known, then the JKR theory gives the interfacial energy γ and the shear strength τ from the measured L_c and F_c.

All of these equations are only valid for parabolic tip profiles. However, a non-parabolic tip shape produces substantially different behavior. We have extended the JKR model to predict the contact area for an axisymmetric tip with a general power law height profile ($z=c \cdot r^n$). The result is given in the Appendix. In general, for a flatter tip profile, such as a quartic tip ($z \propto r^4$), the area does not increase as rapidly with externally applied load as in the case of a parabolic tip. This is intuitively obvious as the limiting case is that of a flat cylindrical punch; the contact area would be independent of load due to the flat tip profile. Yet for different tip shapes, it is still true that there will be a finite critical load and a finite contact area at the critical load, and the modified area-load relation can still be

written in terms of these two parameters. It will therefore be crucial to know the shape of our tip for this analysis, then the interfacial energy and shear strength can be determined.

One can also fit the DMT model to friction data to determine the adhesion energy and shear strength. In this case, since the contact area at the critical load is zero, friction forces should be parametrized by the value of the friction force at *zero* load.

5.3 Experiment

Experiments were carried out to examine the load dependence of friction using mica(0001) substrates with different tips. Mica can be cleaved to produce atomically flat, ordered terraces and serves as a worthwhile comparison for SFA experiments which have used mica extensively.

5.3.1 Sample and Tip Preparation

We have used two different types of microfabricated cantilevers for these experiments: Si_3N_4[17], and Pt-coated Si_3N_4. We believe that Si_3N_4 tips terminate in a layer which has significant nitrogen content as indicated by scanning Auger electron spectroscopy performed on the cantilever arm itself. The other type of cantilevers used were Si_3N_4 cantilevers which we coated with nominally 100 nm of Pt. Our experience has shown that metal-coated AFM tips may lose the coating at the end of the tip due to tip-sample contact stresses. To avoid this, the Pt was deposited after a plasma etch of the lever and tip which promotes adherence. To determine if the Pt coating remained on the end of the tip being used, for each experiment we placed the tip in contact with a conducting sample and measured a low contact resistance (~1.5 kΩ including lead resistance) both before and after acquiring all the data presented below. The resistance did not vary appreciably with applied load, even just before the tip pulled out of contact with the sample. Since Si_3N_4 is an insulator, we conclude that throughout the experiments with Pt-coated levers, the Pt coating was not removed. These resistance measurements were carried out in atmospheric conditions.

The mica surface structure was illustrated in Chapter 4, Figure 4.2. The mica

sample is held fixed in a sample holder inside the UHV chamber; the exact arrangement is described elsewhere[18]. A thin steel foil is epoxied on top of the mica sample and protrudes outward far enough to be grabbed by a wobble stick. Using the wobble stick, the foil is pulled off and carries a few layers of mica with it, exposing a fresh mica surface. The AFM is then brought into range to perform the experiment.

The chamber pressure during the friction experiments was 5×10^{-10} Torr or less, and all experiments were performed with the system at room temperature.

Unfortunately, the tips used for these experiments were too blunt to allow the wedge calibration technique to be utilized. Therefore, lateral and normal forces were estimated using the calculations described in Chapter 3.

5.3.2 Tip Shape Determination

By selecting atomically flat regions on our samples, we have a perfectly characterized geometry for half of the interface being probed. The geometry of the tip must also be known to be able to properly characterize the interface.

A topographic AFM image is actually a convolution of surface and tip features. The smaller and sharper the features of one, the more the AFM image corresponds to the topography of the other. Usually, one requires sharp AFM tips to reveal the surface topography, but equivalently, a sharp surface feature will reveal the tip structure. Several methods have been discussed[19-22] which allow the AFM tip profile to be "imaged" based on this principle. In general, the finite lateral extent of the surface feature will increase the apparent size of the tip. Thus, the "tip images" acquired by these methods are in fact the largest possible tip that could have produced the image, meaning that these methods provide upper bounds on the tip dimensions.

As mentioned in Chapter 3, a sample that can be used for this purpose is the stepped $SrTiO_3$(305) surface[23]. The (101) and (103) facets of the surface meet to form long unidirectional ridges which approach atomic sharpness. These ridges are thus much sharper than a typical AFM tip, and so a topographic scan over a ridge produces a cross-

sectional "image" of the AFM tip that reveals its shape at the nanometer scale. Since the density of ridges is high, acquired images contain many individual "tip images" which can be correlated to reduce the effect of noise and spurious surface features. Since we need to know the tip shape and dimensions, each tip is imaged with $SrTiO_3(305)$ before and after each full set of data. These measurements were performed in air. All references to tip shape and size were obtained by this method. Although these measurements are actually upper bounds to the tip dimensions, there was no substantial difference between tip images acquired on different ridges. This suggests, in combination with TEM images of the $SrTiO_3(305)$ surface[23] and the relatively high elastic modulus of $SrTiO_3$ that the apparent dimensions are not substantially different from the true ones.

5.3.3 Data Acquisition

We simultaneously measure the normal and lateral bending of the AFM cantilever as it is scanned laterally across the sample while the applied load is sequentially stepped[24]. For each line scan, the average value of the critical lateral force required to cause slip is calculated. To eliminate any offset in the lateral force signal (due to coupling between normal and lateral channels), we calculate half the difference between the critical lateral force signals measured for the two opposing scanning directions. Each line scan is acquired at a fixed applied load, then the load is changed slightly, and another line scan recorded. 256 line scans are recorded for each run. Each run is acquired in roughly 30 seconds. Other than the averaging, the data is unprocessed.

These measurements can be performed over any desired load range that is attainable with the particular cantilever used. For these experiments, we usually begin the measurements at a substantial positive load which is sequentially decreased until the tip pulls out of contact with the sample. The data can also be acquired while increasing the load although, due to the jump-to-contact instability, the low-load portion of the friction *vs.* load curve is not accessed.

At very high loads with mica, anomalously large lateral forces occur indicating the

onset of wear of the surface, similar to effects seen in air[24]. For these experiments, all friction data were acquired with the externally applied load remaining well below the wear threshold. Such wear events permanently damage the surface and can be imaged in topographic mode after they occur. Regular imaging of each surface confirmed that scanning the sample did not instigate wear. In general each set of data was acquired over a new area of the surface.

5.4 Results and Discussion

5.4.1 Friction *vs.* Load

Figure 5.4(a) shows a characteristic friction *vs.* load plot for the Pt-coated tip on mica in UHV. The x-axis corresponds to externally applied load *i.e.* normal cantilever displacement with respect to zero bending. The zero point is given by the cantilever position out of contact with the sample when no normal force is acting. The behavior is non-linear with the non-linearity most evident near the critical load. Clearly, there is a finite frictional force at the critical load. Figure 5.4(a) also shows three JKR/extended JKR curves overlaid for comparison. The three curves correspond to successively flatter axisymmetric tip profiles of $z \propto r^2$, r^4, and r^6 respectively, all fit to the critical load and the friction force at zero load (the critical friction force could have been used instead). Clearly, only the parabolic tip suits the data, and it does so very accurately.

One can see that the data cannot be fit by the $z \propto r^4$ and r^6 solutions as they predict friction values too large at negative loads, and too small at positive loads. The disagreement is a consequence of the shape of the curve, as opposed to the relative calibration of the axes. Thus, we can determine whether or not the JKR or extended JKR equations fit the data independent of the absolute calibration of the cantilever forces.

Before these data were taken, the tip was imaged using the $SrTiO_3$(305) surface. An averaged tip profile is shown Figure 5.4(c). The profile is fit well by a parabola with a radius of curvature of 140 nm. The parabolic profile agrees with the JKR fit to the friction data.

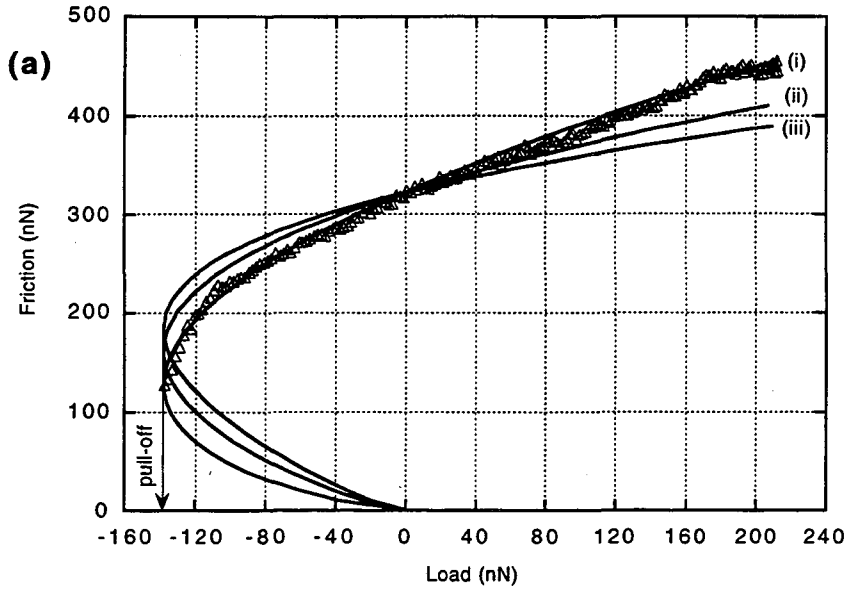
(a)
Friction (nN)
Load (nN)
pull-off
(i)
(ii)
(iii)
500
400
300
200
100
0
-160 -120 -80 -40 0 40 80 120 160 200 240

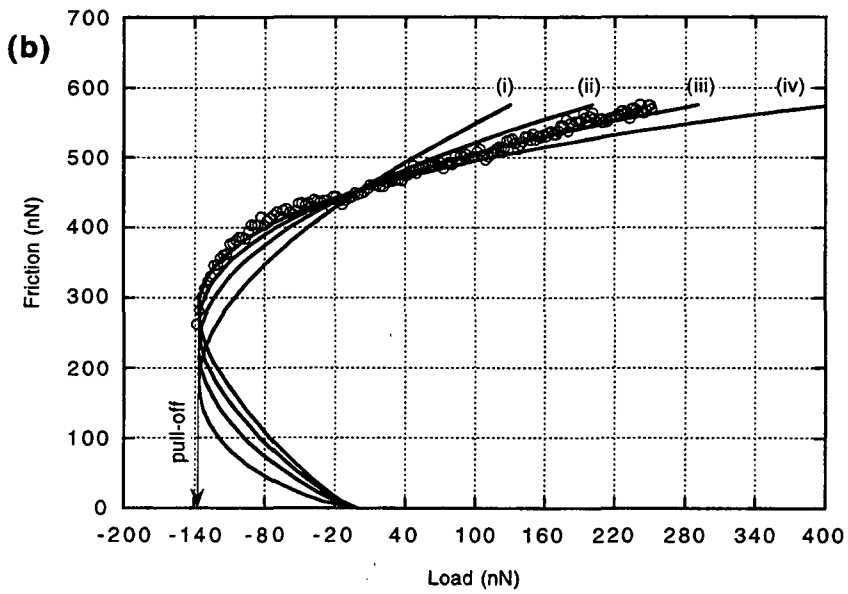
(b)
Friction (nN)
Load (nN)
pull-off
(i)
(ii)
(iii)
(iv)
700
600
500
400
300
200
100
0
-200 -140 -80 -20 40 100 160 220 280 340 400

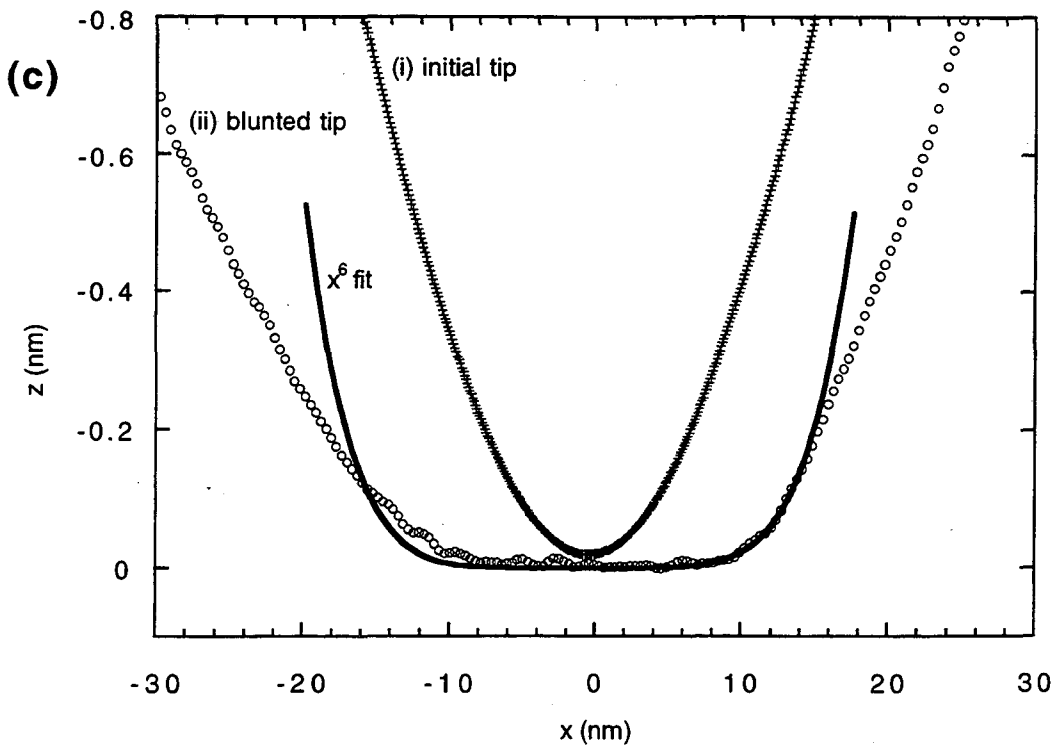
(c)
(i) initial tip
(ii) blunted tip
x^6 fit
z (nm)
x (nm)
-0.8
-0.6
-0.4
-0.2
0
-30 -20 -10 0 10 20 30

Figure 5.4 (previous page) Friction *vs.* load plots for a Pt-coated tip in contact with mica in UHV. (a) Friction data (triangles) and JKR prediction for increasingly flatter tip shapes (solid lines): (i) parabolic, $z \propto r^2$; (ii) $z \propto r^4$; and (iii) $z \propto r^6$. The data initially follow the JKR prediction for a parabolic tip (solid curve (i)). (b) After blunting the tip, friction (circles) varies with load according to a modified JKR description for a flatter tip shape. The solid lines represent the same tip shapes described in (a) with curve (iv) $z \propto r^8$ added for further comparison. (c) Tip cross-sections confirm that in (a) the tip was nearly parabolic and in (b) the tip was flattened, and is fit well by a $z \propto r^6$ dependence.

To further investigate the validity of the JKR or extended JKR models, we decided to study the behavior of a substantially different tip shape and see if the friction *vs.* load behavior changed accordingly. Since the Pt coating is relatively thick (nominally ~100 nm), we attempted to deliberately alter the tip shape by exerting large forces on the tip. This was done by exerting an extremely high load of ~1000 nN on the tip, corresponding to an estimated average pressure of roughly 60 GPa, then reducing the load somewhat to ~500 nN, and then scanning the tip across the surface ~20 times. Friction data was then acquired at the usual applied loads. Figure 5.4(b) shows one of the resultant friction *vs.* load plots, accompanied by fits for the same three tip profiles as before; $z \propto r^2$, r^4, and r^6, with the r^8 solution added for further comparison. Now the r^6 profile provides a good fit. In fact, the r^8 solution fits the data well in the negative load region. This clearly indicates that the end of the tip is indeed flatter than before.

After these data were acquired, we again imaged the tip using the $SrTiO_3(305)$ surface. This time, a much flatter tip profile was observed. Figure 5.4(c) displays the cross-section from the "blunted" tip and the original tip plotted on the same scale, along with a $z \propto r^6$ fit, which is a suitable fit for the end of the tip, consistent with the friction-load data presented in Figure 5.4(b). In fact, the tip shape could certainly be described to greater accuracy by a more complicated function for which an area-load curve could be worked out for comparison to the data. Our main point is that the tip is qualitatively much flatter than before, and that this corresponds to the change in frictional behavior we observed after the tip was blunted. Furthermore, the $z \propto r^6$ solution is seen to be a

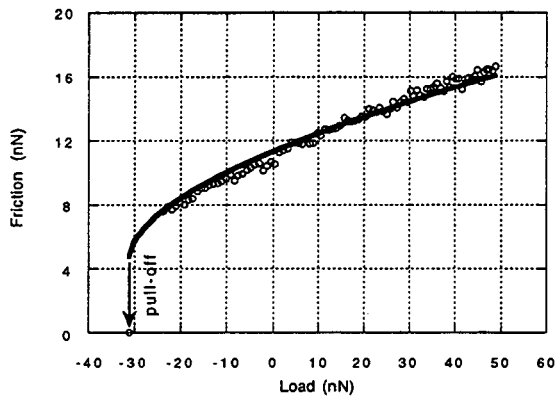

Figure 5.5 Friction *vs.* load measurement for a Si_3N_4 tip on mica in UHV (circles) and a JKR fit to the data (solid line).

reasonable estimate of the tip shape, consistent with both the "tip imaging" technique and the friction *vs.* load data. Calculations based upon this estimate of the tip shape are not significantly affected by considering more exact mathematical descriptions.

A friction *vs.* load measurement for the Si_3N_4 tip is shown in Figure 5.5. Again, the JKR model fits the data extremely well, although the measured forces are very different from the measurements with the Pt-coated tip. In particular, friction forces and adhesion were substantially smaller. Low adhesion led to "premature" pull-off events, where the tip would snap out of contact before the critical load (as measured by taking force-distance curves). This is apparent in Figure 5.5. The JKR curve is thus fit using a value of L_c measured from force-distance curves.

We have attempted to fit all our data by a DMT fit but the quality was much poorer. This can be plainly seen from the data because the DMT theory predicts zero contact area at the critical load; in contrast we always observe a finite frictional force at the critical load. Even adding a finite offset to the frictional forces fails to make the DMT fit better than the JKR fit. Likewise, area-load curves between the JKR-DMT transition did not fit as well as the JKR curves.

Of course, determination of the parameter μ_T, equation (5.9), would be a valuable confirmation that we are in the JKR regime. Unfortunately, we cannot unambiguously determine μ_T since (i) our calibration is uncertain leading to a possible error in the value of γ and (ii) the exact value of z_0 is unknown and thus somewhat arbitrary although we expect

short-range adhesion forces to dominate in vacuum. For our data, using z_0=0.15 nm, estimates for μ_T range from 0.24 to 2.6, which should be in the transition region. Our apparent agreement with the JKR fit could be explained if we have underestimated the normal forces, so the adhesion energies are actually larger. Alternately, the elastic constant values we used, which are from bulk measurements, may be too large.

The above results show that the variation of our friction data with load is described to an excellent degree by JKR/extended JKR model depending on the tip shape. These models predict contact area as a function of load, which indicates that the frictional force between Pt-terminated and Si_3N_4 tips and the mica surface is proportional to the area of contact.

It is important and surprising that a continuum model can account very accurately for the behavior of a nanometer-sized contact which exhibits lateral atomic-scale stick-slip behavior. This is plausible at high loads, where for each load step (typically 1 nN or less) the corresponding change in contact area, using the continuum model, would only be a few mica unit cells. Elastic relaxations of tip and sample atoms can easily smooth out the changes in contact area. Yet even at the lowest loads, the contact area appears to be changing smoothly. Discrete steps in friction corresponding to quantization of the contact area were not observed in these experiments.

As mentioned, shear strength relates frictional force to contact area. A pressure-dependent shear strength has been observed for organic monolayers between mica surfaces in a SFA experiment[16]. Our data indicates direct proportionality between contact area and friction which would imply a pressure-independent shear strength over the pressure range we attained, up to nearly 1 GPa average pressure.

For each set of measurements, fitting the JKR equation to the data gives values for F_c and L_c, from which one can determine γ and τ. To perform these calculations, we used a Young's modulus of 177 GPa for Pt[25], 155 GPa for Si_3N_4[26], and 56.5 GPa for the mica c-axis, calculated from recent Brillouin scattering data[27]. From the same references, the

Table 5.1 Adhesion energy and shear strength measurements for mica in UHV.

Tip	γ (mJ/m^2)	γ (meV/cell)	vdWaals' energy (meV/cell)	τ (MPa)	τ (pN/cell)	frictional work (meV/cell)
Si_3N_4	24	18	6.7	52	6.0	17
Pt: max	404	300	12	910	106	345
Pt: min	19	14	12	270	32	104

Poisson ratios used are 0.39 for Pt, 0.27 for Si_3N_4, and 0.098 for mica. The results are summarized in Table 5.1. The values quoted are from ensembles of measurements. In the case of the Pt-coated tip, there was a systematic reduction of the adhesion and shear strength during the experiment, so the minimum and maximum values observed are quoted. This variation of adhesion and shear strength will be discussed in detail in the next section. No such variation was observed with Si_3N_4 tips.

The highest interfacial energy measured with the Pt-coated tip, 404 mJ/m^2 is more than an order of magnitude higher than adhesion energies of 20 - 50 mJ/m^2 measured with the SFA for inert hydrocarbon surfaces in air[9]. The interfacial energy of two freshly cleaved mica surfaces in contact has been measured with the SFA to be as high as 150 mJ/m^2 in dry nitrogen[28], which is closer to our measurement. In these SFA experiments, adhesion energy is seen to decrease with time due to contamination. The high interfacial energy we measure is not surprising considering that in UHV, contamination is minimized.

Adhesion between Si_3N_4 tips and mica, with an interfacial energy of 24 mJ/m^2, is more than on order of magnitude less than the maximum adhesion measured with the Pt-coated tip. The expected nitride/oxide termination of Si_3N_4 is relatively inert. Not surprisingly, this inertness leads to lower adhesion.

In Table 5.1 we convert the measured adhesion energies to meV per mica unit cell, and compare this to the van der Waals' energy for the respective interfaces[29]. Attractive

van der Waals' forces act for every pair of materials. However, we see that the van der Waals' energy is not large enough to account for the observed adhesion in both cases. Therefore, some other short-range attractive force is acting.

The shear strengths listed in Table 5.1 are converted to pN/mica unit cell, and the amount of energy dissipated, which we call frictional work, is given in meV/mica unit cell. The maximum shear strength observed between Pt-coated tips and mica was 910 MPa, more than an order of magnitude larger than 52 MPa measured for Si_3N_4 tips, and large compared to the bulk yield strength metals, but of the same order of magnitude of the ideal shear strength of metals in the absence of dislocations[30]. A method for determining the ultimate shear strength of a metal-ceramic interface was used for a silica-copper interface[31]. The ultimate shear strength was measured to be in the range of 0.56-1.67 GPa, attributed to strong metal-oxide bonds formed at the interface. The Pt-mica interface thus initially possesses a shear strength equivalent to a covalently-bonded interface. Israelachvili measured a shear strength of 25 MPa for a mica-mica interface with the SFA, where the surfaces had been exposed to laboratory air and thus were covered with hydrocarbon contaminants. The Si_3N_4-mica interface exhibits shear strengths in this range, but much lower than for the covalently bonded interface.

To obtain an order-of-magnitude estimate of the number of phonons generated during sliding, we can compare the frictional work listed in Table 5.1 to the energy of longitudinal acoustic phonons in mica with a wavevector corresponding to the contact size. In a single slip event, 85 phonons/mica unit cell are generated for the Si_3N_4 tip, and 1700 phonons/mica unit cell for the Pt-coated tip.

Application of the JKR model allows us to explicitly calculate the area of contact. The contact area and radius at the critical load is listed in Table 5.2 for the two tips. We see that even at the lowest attainable loads and with the lower adhesion cases, many surface unit cells are in contact with the tip, which we had stated previously in more general terms. Clearly, if the AFM tip is used to image a sample, it will not resolve individual atoms.

Table 5.2 Tip-sample contact size at the critical load.

tip	contact radius (nm)	contact area (nm^2)	area in terms of # of mica unit cells
Si_3N_4	5.3	87	740
Pt: max. adhesion	8.6	230	2000
Pt: min. adhesion	3.0	29	250

5.4.2 Variation of Shear Strength and Adhesion

Another surprising finding of this study was the variation of the frictional properties of the platinum tip on mica as a result of repeated scanning. For the initial set of data (before the tip was blunted), every friction curve obtained could be fit with a JKR curve. However, the values of L_c and F_c changed with repeated scanning. In particular, both L_c and F_c were seen to decrease slightly from one run to the next (less than 5% per run). Figure 5.6 displays a selection of the friction-load curves obtained. Clearly, L_c and F_c progressively decrease as runs are performed, which after many runs results in a large overall change. Each run was performed over a new area of the mica surface.

Throughout the experiment, we were able to obtain atomic lattice resolution images of the mica surface. Despite the dramatic change in frictional forces that occurred, no noticeable changes were observed in the atomic-lattice resolution images. This does not rule out any changes of the tip, but merely indicates that the stick-slip behavior persisted.

Only a change in the surface of the tip, either structural or chemical, can explain our observations. We established that this adhesion decrease was related to the tip, and was induced by scanning the tip in contact with the mica as follows. The change in L_c and F_c did not depend upon the time interval between runs, as one might expect if there was some sort of accumulating surface contamination. For example, some of the curves in Figure 5.6 were in fact acquired 12-24 hours apart, whereas most of the other curves were acquired a few minutes apart, yet the change in L_c and F_c are about the same from one curve to the next. Our microscope is capable of coarse lateral position adjustment, and so we took

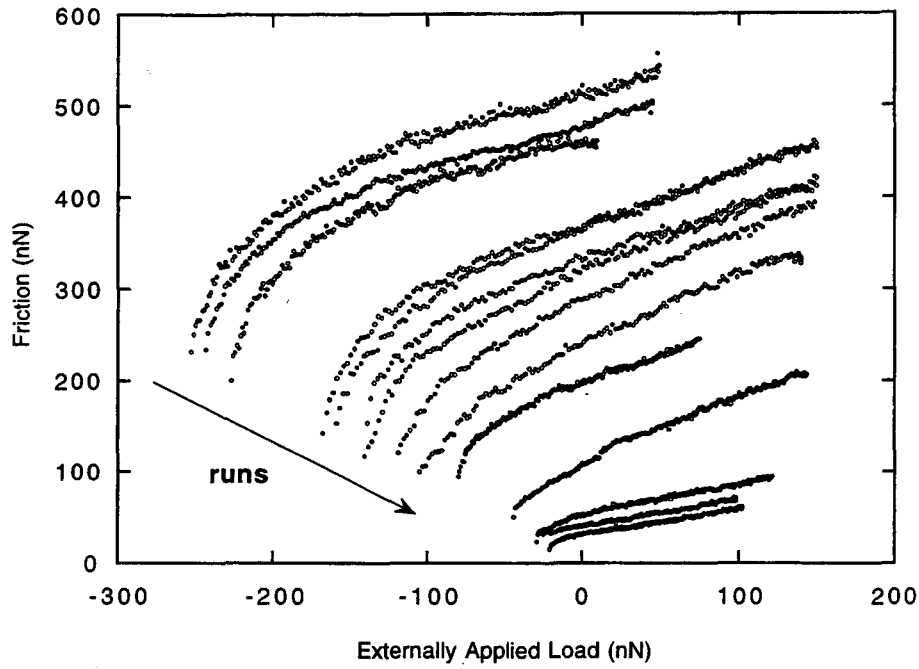

Figure 5.6 Scanning-induced reduction of adhesion energy and shear strength is revealed by friction *vs.* load plots for a Pt-coated tip in contact with mica in UHV. After each plot, the pull-off force decreased in magnitude, implying a scanning-induced decrease in the adhesion energy. Curve fitting reveals that the shear strength also decreased. This implies that changes in the structure or chemistry of the interface can dramatically affect friction and adhesion.

advantage of this by positioning the cantilever over several new regions of the sample. The subsequent values of L_c and F_c continued to monotonically decrease, independent of the imaging location.

We also investigated whether or not a brief tip-sample contact had any effect. This was done by taking several force-distance curves. Without scanning, the tip-sample separation was varied, bringing the tip in and out of contact with the sample. The force required to pull the tip out of contact with the sample corresponds to L_c. We were not able to cause L_c to decrease simply by acquiring force-distance curves. Finally, we rule out any change in the large-scale structure of the tip to account for the adhesion decrease. As mentioned above, changes in the tip shape are clearly reflected in the friction-load curve. Our friction-load curves were all consistent with a parabolic tip profile, and inconsistent

with any substantially different tip profile. Furthermore, looking at equations (5.5) and (5.11), for L_c and F_c to decrease would require the tip radius R to systematically shrink, which seems implausible.

In summary, L_c and F_c decreased *if and only if the tip was scanned in contact with the sample*. Since a JKR curve can describe each friction measurement, and R and K were constant, we conclude that the variation of L_c and F_c correspond to changes in the interfacial energy γ and the shear strength τ brought about by changes in the *interfacial* chemistry or structure induced by scanning[32]. Table 5.1 shows the largest and smallest values of γ and τ that we measured for the initial set of experiments.

Since we are unable to spectroscopically analyze the tip, explanations of this effect are purely conjectural. One particular chemical change worth discussing is scanning-induced transfer of potassium from the mica surface to the tip. The mica cleavage plane exposes potassium ions which are strongly bound to the mica surface, but during tip-sample contact there is a finite probability that a potassium atom will transfer to the metal tip and adsorb. An energetic barrier to this process as well as diffusion of potassium on the platinum tip[33] would necessitate repeated transfer events to eventually saturate the end of the tip. Furthermore, it has recently been observed that potassuim will also incorporate itself into the platinum lattice[34]. This is all consistent with our observation of a gradual, scan-by-scan change in adhesion. Potassium adsorption lowers the surface free energy of the platinum, thus the work of adhesion will decrease as potassium adsorbs since the sample, being much larger than the contact zone itself, provides a reservoir of potassium to replenish vacancies in the mica surface. In other words, the partially potassium-covered tip will not have as strong a chemical attraction to the potassium-covered mica surface as a cleaner metal tip would. Note that our estimated total decrease in the work of adhesion is ~0.39 J/m^2 (see Table 5.1). The energy of adsorption of potassium on the clean Pt(111) surface at one monolayer coverage in UHV has been measured[33] to be ~0.94 J/m^2 which is of the same order of magnitude. Attributing the adhesion energy decrease to potassium

adsorption is therefore not physically unreasonable.

Another possibility is a structural rearrangement of tip atoms at the interface caused by sliding. It has been postulated that changes in the atomic commensurability of the contacting surfaces would cause changes in friction and adhesion[35-37]. Increased commensurability is expected to increase friction and possibly adhesion as tip and sample atoms can "lock together" more easily. Indeed, mica surfaces in contact that were rotated with respect to one another produced maximum adhesion[36] and friction[37] when the orientation of the two mica sheets matched[38]. From this point of view, the observed decrease in friction and adhesion with scanning implies that scanning reduces commensurability. Whether this occurs in our case is not known, and it is not obvious that the tip structure should have any degree of commensurability with the mica to begin with. Nevertheless, further experiments are needed to investigate this interesting possibility.

In any case, it is remarkable that such a dramatic change in friction and adhesion occurs as a result of interfacial changes. Order of magnitude changes in adhesion and friction can thus occur even though bulk properties such as the tip radius, phonon spectrum and specifically the elasticity, which also play crucial roles in determining friction, are unchanged. As stated previously, we did not observe such a variation of adhesion and friction in experiments with silicon nitride tips. This may reinforce the idea that the chemistry of the surface of the tip plays a role, as platinum has very different chemistry than the expected passive terminations of silicon nitride tips. Alternately, platinum is more ductile than silicon nitride which is a fairly brittle material. Thus, a structural change in the tip termination brought about by shear forces is also more likely to occur with platinum.

As mentioned above, the platinum-coated tip was blunted after this set of experiments and further friction measurements performed. This was followed by measuring the contact resistance between the tip and a conducting sample which confirmed that the platinum coating had not been removed. Immediately after blunting the tip, the adhesion and friction recovered, but again progressively decreased with scanning. From

these measurements, we estimate that immediately after blunting the tip, the interfacial energy had recovered to ~100 mJ/m^2, a value in between the initial and final values measured before blunting the tip. This further supports the idea that the tip chemistry is affecting the adhesion, since blunting the tip presumably exposes new unreacted platinum, thus restoring the adhesion.

We thus have a set of measurements for a single system where γ and τ vary due to interfacial changes. We can therefore probe the relation between γ and τ. For each set of data in Figure 5.6 (*i.e.* before blunting the tip), F_c and L_c can be determined. Figure 5.7 shows a plot of F_c *vs.* L_c. The dependence is nearly linear. Since L_c is proportional to γ, while F_c is proportional to $\tau \cdot \gamma^{2/3}$, this implies that τ is only weakly dependent upon γ. By calculating τ and γ for each point (F_c, L_c) in Figure 5.7, we determined that $\tau \propto \gamma^{\lambda}$ where $\lambda \cong 0.44 \pm 0.10$. Any uncertainty due to calibration does not affect the functional dependence of shear strength upon adhesion.

The weak dependence of the shear strength upon the adhesion is a surprising result. Sophisticated models relating friction and adhesion simply do not exist, although in the most simple case, one might expect τ to be linearly proportional to γ. A simple model relating surface energy and shear strength in the absence of wear is the so-called "Cobblestone Model"[4,39-41]. Surfaces sliding with respect to one another are considered in a similar fashion to the wheels of a cart rolling over a cobblestone street. If at rest, the wheels will be settled into grooves between the cobblestones. To initiate motion, a lateral force is required to lift the wheels out of the grooves and over the cobblestones. In this model, the force of gravity is replacing the attractive surface forces. For an atomically smooth sample, the "cobblestones" could represent the atomic corrugation. SFA experiments for contacts between hydrocarbon surfaces or surfaces with layers of liquid molecules in between show general agreement with the model[4,9,40]. However, the model predicts that the shear strength is linearly proportional to the interfacial energy ($\lambda = 1$)[9], which we do not observe in this case. The model is essentially geometric in nature, which

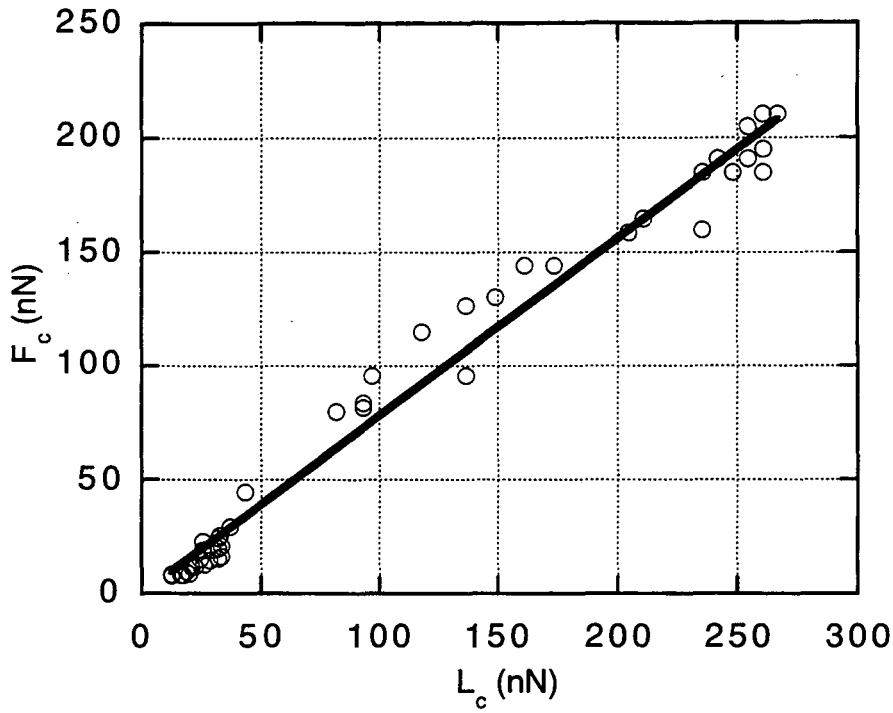

Figure 5.7 Plot of the values of F_C and L_C measured from a large number of runs, some of which are displayed in Figure 5.6. The dependence is nearly linear. The interfacial energy g and the shear strength t were calculated for each point. A fit to a power law $\tau \propto \gamma^{\lambda}$ gives $\lambda \cong 0.44 \pm 0.10$.

is too simple to describe the atomic-scale interactions taking place at the interface.

Another model relating friction and adhesion has been proposed by Israelachvili[9,42] Experiments with the SFA have shown that for systems of chain-like molecules between contacting surfaces, the adhesion energy increases while surfaces are in contact. Hysteresis of the contact area then occurs between approach and retraction of the surfaces, and evidence suggests that frictional forces are larger when adhesion hysteresis is larger. However, this is inconsistent with our observations as we do not observe any frictional hysteresis when comparing increasing and decreasing loading. Israelachvili's theory is based on studies of particular molecular structures such as long hydrocarbon chain molecules, whereas according to the theory adhesion hysteresis is not expected for solid-

solid contacts. The theory attributes the hysteresis to complex phenomena occurring at the interface, namely reorientation, interdiffusion and interdigitation of the molecules. These processes have long relaxation times which are comparable to the time the surfaces spend in contact with each other, and so equilibrium is not reached during contact. In contrast, we do not expect processes with long relaxation times to occur on surfaces in UHV as the interface is much less complex. Also, the model predicts a cyclical hysteresis as opposed to the progressive changes in adhesion and shear strength which we observe.

It is thus not clear yet whether the observed power law represents a very specific case of the friction-adhesion relation for the particular platinum-mica system studied here, or is a more general phenomenon. More experiments with other systems are needed to understand this important relation.

5.5 Summary

Macroscopic theories and experiments have shown that friction is proportional to applied load, where the constant of proportionality is defined as the friction coefficient. These macroscopic situations involve multiple asperity contacts and plastic deformation. The results presented here are the first comprehensive measurements ever in UHV of nanometer-sized single asperity contacts. Our results demonstrate that the concept of a friction coefficient, *i.e.* Amonton's Law, is not valid in the elastic single-asperity regime for nanometer-sized contacts. Rather, the frictional force is proportional to the contact area predicted by the JKR theory of elastic adhesive contacts. These results demonstrate the surprising applicability of continuum mechanics theories at the nanometer scale.

These results demonstrate that one can calculate interfacial energies and shear strengths, to the extent that the tip dimensions, elastic moduli, and AFM signal calibrations are known. The entire shape of the JKR curves are fixed by selection of one pair of points on the friction-load plot, allowing us to see the difference between a parabolic tip versus a flatter tip that was deliberately blunted. This difference was verified with "tip images" acquired by scanning sharp ridges on the $SrTiO_3(305)$ surface. This establishes that the tip

shape and composition are critical in determining the frictional behavior observed in an AFM experiment on a particular surface. Friction measurements with AFM cannot be considered to be fundamental unless these considerations are taken into account.

Our results indicates that the shear strength is pressure-independent in the pressure range we examined. Using the JKR theory, adhesion energies and shear strengths were calculated for the interface between mica and Pt-coated and Si_3N_4 tips in UHV. In the case of the Pt-coated tip, the tip-sample adhesion dropped by more than one order of magnitude during the experiment, as did the measured frictional forces. These dramatic changes were induced by scanning the tip in contact with the mica sample. We attribute the substantial friction and adhesion decreases to changes of the interface, either structural or chemical, as opposed to changes in bulk structure or properties. The interfacial energy, γ, dropped by more than one order of magnitude while the shear strength, τ, decreased to a lesser extent. Our observations indicate that for a platinum-coated tip on mica, $\tau \propto \gamma\lambda$ where λ=0.44±0.10. This is a new observation of a relation between adhesion and friction, and is not explained by existing theories.

5.6 Appendix - Extended JKR Model

The JKR model can be applied to an axisymmetric tip with height profile $z = c \cdot r^n$. The analytic result expresses the load as a function of contact area as follows:

$$L = -(6\pi\gamma K)^{1/2} \cdot \left(A/\pi\right)^{3/4} + \tfrac{3}{2} Kcn\psi\left(A/\pi\right)^{\frac{n+1}{2}} \tag{5.15}$$

where

$$\psi = \frac{\left(\frac{n}{2}\right)!^2\, 2^n}{(n+1)!},\ n \text{ even} \tag{5.16}$$

$$\psi = \frac{(n+1)!}{\left(\frac{n+1}{2}\right)!^2\, 2^{n+1}},\ n \text{ odd}. \tag{5.17}$$

Assuming $F_f = \tau \cdot A$, the non-dimensional form of the equation in terms of the frictional force F_f is given by:

$$\hat{L} = -\left(\frac{2n+2}{2n-1}\right) \cdot \hat{F}_f^{\,3/4} + \left(\frac{3}{2n-1}\right) \cdot \hat{F}_f^{\,\frac{n+1}{2}} \tag{5.18}$$

where

$$L_c = -\frac{(2n-1)}{2(n+1)} \cdot \left[\frac{(6\pi\gamma)^{n+1} \cdot K^{n-2}}{\left(n(n+1)c\psi\right)^3} \right]^{\frac{1}{2n-1}} \tag{5.19}$$

and

$$F_c = \tau \cdot A_c = \tau \cdot \pi \cdot \left[\left(\frac{6\pi\gamma}{K} \right) \cdot \frac{1}{\left(n(n+1)c\psi\right)^2} \right]^{\frac{2}{2n-1}} \tag{5.20}$$

in analogy to equations (5.5) and (5.10)-(5.14).

Chapter 5 References

[1] R. W. Carpick, N. Agraït, D. F. Ogletree, and M. Salmeron, J. Vac. Sci. Technol. B **14,** 1289 (1996).

[2] R. W. Carpick, N. Agraït, D. F. Ogletree, and M. Salmeron, Langmuir **12,** 3334 (1996).

[3] K. L. Johnson, *Contact Mechanics* (University Press, Cambridge, 1987).

[4] A. M. Homola, J. N. Israelachvili, M. L. Gee, and P. M. McGuiggan, J. Tribology **111,** 675 (1989).

[5] H. Hertz, J. Reine Angew. Math. **92,** 156 (1881).

[6] K. L. Johnson, K. Kendall, and A. D. Roberts, Proc. Roy. Soc. Lond. A **324,** 301 (1971).

[7] D. Maugis and M. Barquins, J. Phys. D. (Appl. Phys.) **16,** 1843 (1983).

[8] D. Maugis, Langmuir **11,** 679 (1995).

[9] J. N. Israelachvili, in *Fundamentals of Friction*, edited by I. L. Singer and H. M. Pollock (Kluwer, Dordrecht, 1992), p. 351.

[10] B. V. Derjaguin, V. M. Muller, and Y. P. Toporov, J. Colloid Interface Sci. **53,** 314 (1975).

[11] K. L. Johnson, Langmuir **12,** 4510 (1996).

[12] D. Maugis, J. Colloid Interface Sci. **150,** 243 (1992).

[13] V. M. Müller, V. S. Yushenko, and B. V. Derjaguin, J. Colloid Interface Sci. **77,** 91 (1980).

[14] B. J. Briscoe and D. C. B. Evans, Proc. Roy. Soc. Lond. A **380,** 389 (1982).

[15] Sharpened Microlever, Park Scientific Instruments, Sunnyvale, CA.

[16] Q. Dai, R. Vollmer, R. W. Carpick, D. F. Ogletree, and M. Salmeron, Rev. Sci. Instrum. **66,** 5266 (1995).

[17] F. Atamny and A. Baiker, Surf. Sci. **323,** L314 (1995).

[18] A. L. Bogdanov, D. Erts, B. Nilsson, and H. Olin, J. Vac. Sci. Technol. B **12,** 3681 (1994).

[19] L. Montelius, J. O. Tegenfeldt, and P. van Heeren, J. Vac. Sci. Technol. B **12,** 2222 (1994).

[20] T. O. Glasbey, G. N. Batts, M. C. Davies, D. E. Jackson, and others, Surf. Sci. **318,** L1219 (1994).

[21] S. S. Sheiko, M. Möller, E. M. C. M. Reuvekamp, and H. W. Zandbergen, Phys. Rev. B **48,** 5675 (1993).

[22] J. Hu, X.-D. Xiao, D. F. Ogletree, and M. Salmeron, Surf. Sci. **327,** 358 (1995).

[23] *Metals Handbook*, 10th ed. (American Society for Metals, Metals Park, Ohio, 1990).

[24] Dr. M. Tortonese, Park Scientific Instruments Inc., Sunnyvale, CA (personal communication).

[25] L. E. McNeil and M. Grimsditch, J. Phys: Condens. Matter **5,** 1681 (1992).

[26] H. K. Christenson, J. Phys. Chem. **97,** 12034 (1993).

[27] J. N. Israelachvili, *Intermolecular and surface forces*, 2nd ed. (Academic Press London, London, 1992).

[28] A. Kelly, *Strong Solids*, 2nd ed. (Oxford University Press, London, 1973).

[29] D. C. Agrawal and R. Raj, Acta Metall. **37,** 1265 (1989).

[30] Since the decrease of γ and τ occurs during scanning, fitting each of the friction-load curves to the JKR equation is not strictly correct since fixed values of γ and the τ are assumed for such a fit. However, the changes in these values were sufficiently small so that ignoring them for an individual fit introduces a negligible error. In fact, adapting the JKR equation to take such changes into account has a negligible effect (K.L. Johnson, personal communication).

[31] E. L. Garfunkel and G. A. Somorjai, Surf. Sci. **115,** 441 (1982).

[32] J. B. Hannon, M. Giesen, C. Klunker, G. S. Icking-Konert, D. Stapel, H. Ibach, and J. E. Muller, Phys. Rev. Lett. **78,** 1094 (1997).

[33] J. B. Sokoloff, Wear **167,** 59 (1993).

[34] P. M. McGuiggan and J. N. Israelachvili, J. Mater. Res. **5,** 2232 (1990).

[35] M. Hirano, K. Shinjo, R. Kaneko, and Y. Murata, Phys. Rev. Lett. **67,** 2642 (1991).

[36] However, the presence of adhesion and friction anisotropy depended upon the experimental environment. Adhesion anisotropy occurred in humid air (33% RH) but not in dry nitrogen. Friction anisotropy occured in dry air at higher temperature (130° C) but not in ambient air.

[37] M. J. Sutcliffe, S. R. Taylor, and A. Cameron, Wear **51,** 181 (1978).

[38] A. M. Homola, J. N. Israelachvili, P. M. McGuiggan, and M. L. Gee, Wear **136,** 65 (1990).

[39] G. M. McClelland, in *Adhesion and Friction, Springer Series in Surface Science*; *Vol. 17* (1989), p. 1.

[40] H. Yoshizawa, Y.-L. Chen, and J. Israelachvili, Wear **168,** 161 (1993).

6. The Lateral Stiffness Measurement Technique

6.1 Introduction

The results of the previous chapter demonstrate that AFM is capable of measuring fundamental friction and adhesion properties of nanometer-sized contacts. However, quantitative analysis requires choosing a specific continuum mechanics model to describe the tip-sample contact area. Instead of relying upon a model, it would be desirable to have an independent experimental measurement that is related to the tip-sample contact area. We subsequently discovered that this is possible by measuring the lateral stiffness of the tip-sample contact[1]. This chapter describes the technique to perform this measurement, and presents examples of lateral stiffness measurements.

6.2 Theoretical Framework

As we showed in the last chapter, the AFM tip can form a single-asperity contact with a surface[2-5] and wearless interfacial sliding occurs. Friction scales with load in proportion to the area of contact as predicted for a continuous, elastic, single asperity contact. In other words,

$$F_f = \tau \cdot A = \tau \cdot \pi \cdot a^2 \tag{6.1}$$

where F_f is the frictional force, A the contact area, a the contact radius, and τ the shear strength (shear force/area). However, the contact area is not directly measured, so a contact mechanical model must be chosen to properly investigate the relationship between friction and contact area. The particular model utilized, such as the Hertz or JKR model, depends upon the strength and range of the tip-sample interaction forces (among other things), which is uncertain in each case. The contact area - load relation for a single asperity also depends upon the tip shape, as demonstrated in the previous chapter.

Furthermore, if the shear strength is not independent of load (pressure) then the load dependence of shear strength and contact area become convoluted in the friction measurement[3]. Indeed, pressure dependent shear strengths have been reported in SFA[6] and macroscopic experiments[7,8]. For these reasons, an independent measurement related to the contact area is desirable.

Contact stiffness is defined as the amount of force per unit displacement required to compress an elastic contact in a particular direction, has the units of N/m, and is essentially the "spring constant" of the contact. For example, the normal stiffness is given by $\kappa = dL/dz$, where L is the applied load (normal force), and z is the elastic penetration depth. In the Hertz case, a sphere-plane contact,

$$\kappa_{contact} = 2aE^* \tag{6.2}$$

where $E^* = \left[\left(1-\nu_1^2\right)/E_1 + \left(1-\nu_2^2\right)/E_2\right]^{-1}$; E_1 and E_2 the respective Young's Moduli, and ν_1 and ν_2 the respective Poisson ratios (in the previous chapter we used the symbol K which is related to E^* via $K = \frac{4}{3}E^*$). From equation (6.2) the normal stiffness, for the Hertz model, is directly proportional to the contact radius. Typically the contact strain is concentrated within a volume of the order a^3.

With AFM, the plane corresponds to the sample, and the sphere corresponds to the tip. In addition, the sphere is attached to a spring, *i.e.* the cantilever, which has its own stiffness (the normal spring constant κ_{lever}). The cantilever and the contact are thus two springs in series, as described in Figure 6.1(a).

For nanometer-sized contacts between common materials like metals and ceramics, stiffness values are roughly 50-500 N/m. However, the normal stiffness of typical commercial cantilevers, κ_{lever}, is on the order of 0.01 to 1 N/m. Thus nearly all the elastic compression is taken up by the lever and not the contact, so the measurement is relatively insensitive to $\kappa_{contact}$. Notably, Pethica and co-workers[9] have designed a substantially modified scanning force microscope using custom-made cantilevers where a magnetic force

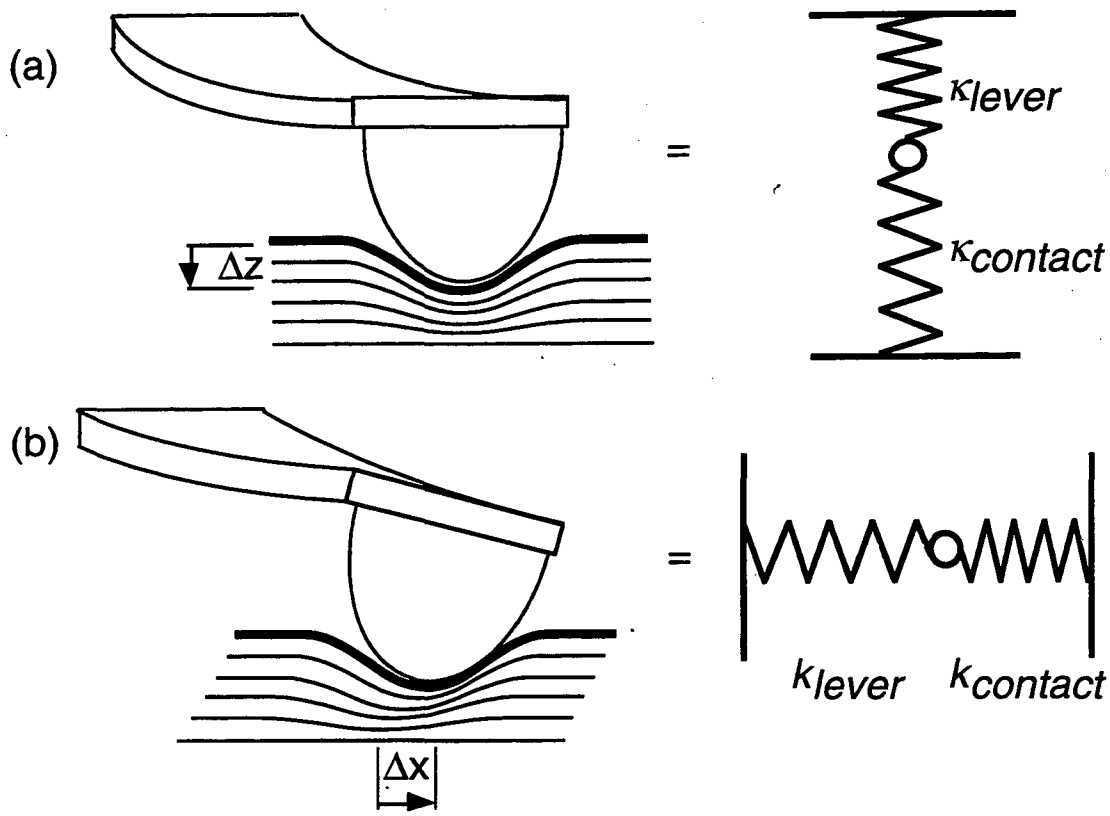

Figure 6.1 The cantilever : contact system consists of two springs in series depending on the mode of compression. If the relative normal displacement between the cantilever and sample is changed, as shown in (a), compression of both the cantilever, with normal spring constant k_{lever}, and the contact (tip + sample), with normal stiffness $k_{contact}$, will occur. (b) depicts the case of a relative lateral displacement; lateral compression of the contact, with stiffness $k_{contact}$, will occur along with a twisting of the lever with spring constant k_{lever}.

is directly applied to the tip. This effectively allows control of the compliance of the cantilever, and so the normal contact stiffness can be sensitively measured. This set-up is not trivial to implement.

A different approach is suggested by the fact that the typical *lateral* stiffness of commercial AFM cantilevers, k_{lever}, is around 50-200 N/m (as shown in Chapter 3)[10], *i.e.* of the same order as the lateral contact stiffness, $k_{contact}$, so typical cantilevers can accurately measure variations in the *lateral* stiffness of nanometer-sized contacts, *i.e.*

$$\frac{dF_{lateral}}{dx} = k_{tot} = \left(\frac{1}{k_{lever}} + \frac{1}{k_{contact}} \right)^{-1} \tag{6.3}$$

where $F_{lateral}$ is the lateral force (cantilever torsion), and x is the lateral displacement (Figure 6.1(b)). For a sphere-plane contact, $k_{contact}$ is given by[11]

$$k_{contact} = 8G^* a \tag{6.4}$$

where

$$G^* = \left(\frac{2-\nu_1}{G_1} + \frac{2-\nu_2}{G_2} \right)^{-1} \tag{6.5}$$

Here G_1 and G_2 are the tip and sample shear moduli, respectively. Again, $k_{contact}$ is directly proportional to the contact radius. Equation (6.4) is a very powerful equation because it is extremely general. It is valid regardless of the tip-sample interaction forces[12], unlike the analogous equation for normal stiffness, equation (6.2), which must be modified for non-Hertzian contacts. It is also valid for any axisymmetric tip shape, not just a paraboloid.

A simple explanation of (6.4) is obtained by considering an applied lateral force $dF_{lateral}$ at fixed load, *i.e.* applying a lateral stress $d\sigma$ over the contact area A, producing a proportional strain $d\varepsilon$, where $d\varepsilon \propto dx/a$ (since a is the length scale of the stress distribution). Stress and strain are related by Hooke's Law,

$$d\sigma = G \times d\varepsilon \tag{6.6}$$

where G is the shear modulus, appropriate for the direction of the applied stress considered here. Hence

$$\frac{dF_{lateral}}{A} \propto G \times \frac{dx}{a} \tag{6.7}$$

which gives

$$\frac{dF_{lateral}}{dx} \propto G \times a \tag{6.8}$$

as in equation (6.4). Note the simplifying assumption that the contact radius is not affected by the lateral displacement dx. This is reasonable and expected for small lateral displacements[12]. In the case of normal stiffness, the normal displacement dz *does* change the contact radius even for an infinitesimal displacement. This is because load, normal

displacement, and contact area are all interdependent. This essentially explains why normal stiffness is *not* generally proportional to contact radius (except in the Hertz case).

Thus, a measurement of the lateral contact stiffness produces a quantity that is proportional to the contact radius. This can be compared to a friction measurement to see how friction and contact area are related. We can see if equation (6.1) holds, and if so, determine the load dependence of the shear strength.

6.3 Lateral Stiffness Experimental Technique

6.3.1 Instrumental Setup

As long as there is finite static friction between the tip and sample, the lateral stiffness can be measured. Consider the lateral force response of a cantilever as it scanned across a sample (Figure 6.2). Typically atomic scale stick-slip behavior is preceded by an initial sticking portion, the slope of which corresponds to $dF_{lateral}/dx=k_{tot}$, the total lateral stiffness. It is this slope which we wish to accurately measure.

A block diagram of the experimental setup is shown in Figure 6.3. At a fixed load, the relative position between the cantilever base and the sample is modulated laterally in a sinusoidal fashion with an amplitude that is small enough to avoid the onset of sliding

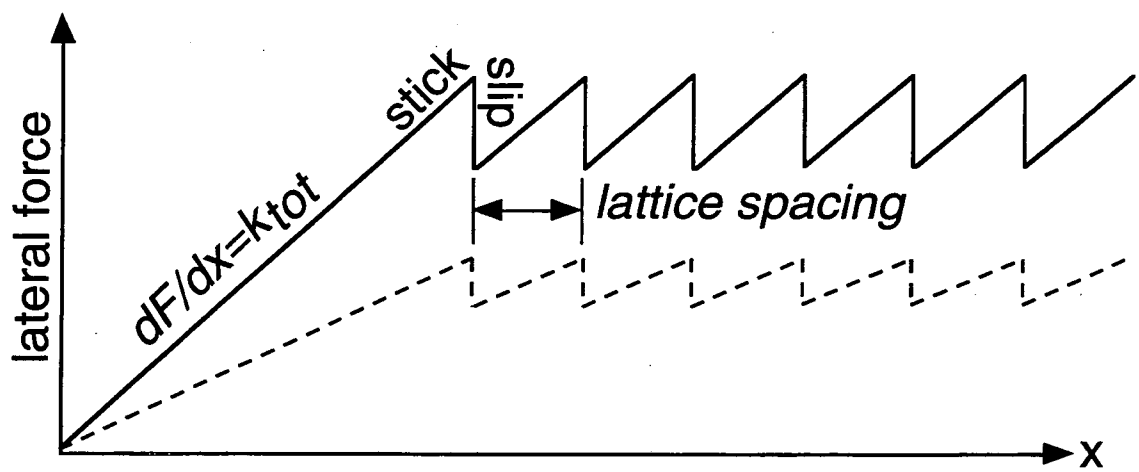

Figure 6.2 Lateral force signal *vs.* lateral displacement (x). Solid line: a relatively stiff contact. Dashed line: a more compliant contact - there is less cantilever bending per unit displacement as the contact is compressed more.

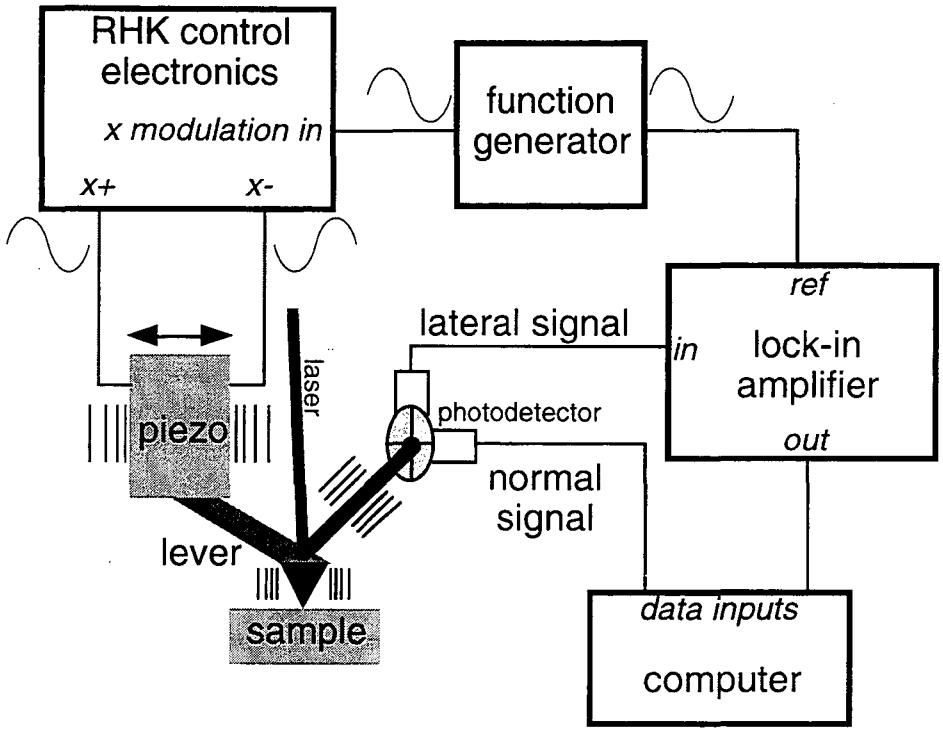

Figure 6.3 Block diagram of the experimental set-up for measuring lateral stiffness.

(which occurs most easily at low loads). Typically the amplitude of relative displacement is less than 0.5 nm. The amplitude of the lateral response of the cantilever is measured with a lock-in amplifier.

It is easy to determine whether or not the amplitude of this displacement is too large by monitoring the lateral response on an oscilloscope, as described in Figure 6.4, since the slips show up clearly in the time response. The response is no longer harmonic if slip occurs. Therefore, the lock-in amplifier will detect a significant out-of-phase component. A two channel lock-in can monitor this, to allow discarding of measurement points where slip occurred. An example using this will be presented in section 6.4.3.

The lock-in output is divided by the amplitude of relative displacement, dx. This corresponds to the *total* lateral stiffness of the system, k_{tot} (equation (6.3)). We chose an oscillation frequency of 200 Hz to avoid a resonance of our microscope head near 1 kHz. Higher frequencies would otherwise be suitable to use. The lock-in time constant is set to

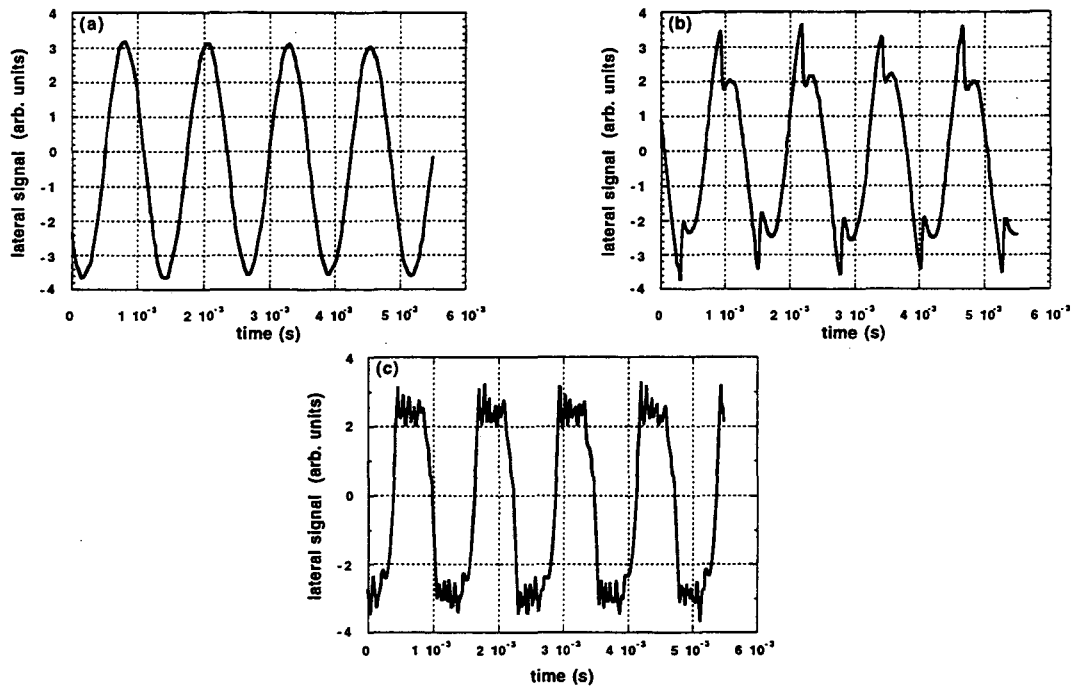

Figure 6.4 (a) Lateral force response for a lateral modulation displacement amplitude that is less than the critical value for slippage to occur. The response is completely harmonic. (b) After increasing the modulation amplitude slightly, slippage begins and one atomic slip per cycle is clearly observed. This produces a measurable out-of-phase response easily detected with a lock-in amplifier. The transition between the signals shown in (a) and (b) is quite sharp. (c) Lateral force response for a modulation amplitude that is even larger. Several slips per cycle are clearly observed.

be long enough to sample many cycles. We sample two data points at each load, then change the load slightly, and take another measurement, and so on. The lock-in signal gives $dF_{lateral}$, while dx must be determined by accurately knowing the piezo response calibration. We note that virtually the same equipment and setup was used by Colchero *et al.*[13] to measure sliding friction with AFM. In their experiment, the lateral displacement amplitude was deliberately large so that relative tip-sample sliding took place. The resulting signal amplitude was deconvoluted to get a measure of the frictional force during sliding.

6.3.2 Data Analysis

We wish to extract $k_{contact}$ from the measurement of k_{tot}. Thus we must know k_{lever}, the lateral force spring constant of the cantilever. Although k_{tot} asymptotically approaches k_{lever} at high loads, generally the load at which this asymptotic value is reached can be very

high, even beyond the load range of the experiment. This is seen by considering equation (6.3): for k_{tot} to reach 90% of k_{lever}, $k_{contact}$ must be 9 times greater than k_{lever}. Using the Hertz model to calculate, this requires a 729 (=9^3)-fold increase of the load from the value at which $k_{lever} = k_{contact}$.

If k_{lever} is known from a precise lever calibration, then that value can be used for $k_{contact}$. However, for reasons we have pointed out in Chapter 3, an accurate knowledge of lever force constants is difficult. Furthermore, Lantz *et al.*[14] have pointed out that for high aspect ratio tips, the tip structure itself can have significant lateral compliance, which for would add another force constant in series with the cantilever (*i.e.* renormalizing the value of k_{lever} in equation (6.3)). In our case, we only rely upon κ_{lever} (the normal force spring constant), and the lateral *vs.* normal force sensitivity ratio, which we can determine experimentally using the wedge calibration technique. We have not assumed a value for k_{lever}. If we do choose a contact mechanics model to fit the data, then k_{lever} can be an adjustable fitting parameter. However, this again necessitates choosing a particular contact mechanics model. To avoid this, a direct comparison between friction and stiffness measurements can be made to determine k_{lever} as follows. If equation (6.1) applies, then it can be combined with equations (6.3) and (6.4) to give

$$k_{tot}^{-1} = k_{lever}^{-1} + \frac{\sqrt{\pi \cdot \tau}}{8 \cdot G^*} \cdot F_f^{-1/2} \qquad (6.9)$$

Therefore, a plot of k_{tot}^{-1} *vs.* $F_f^{-1/2}$ will yield a linear relation, if friction is directly proportional to the contact area. From equation (6.9), the y-intercept is equal to k_{lever}. For all the data presented in this chapter, this linear relation was confirmed and k_{lever} thus obtained. In principle, one could use the slope of the plot of equation (6.9) to also determine τ. However, the expected non-linear dependence of both friction and stiffness upon load will lead to a clustering of points about the larger values of friction and stiffness. It is better to plot τ as a function of load, as described in the next section.

6.4 Lateral Stiffness Measurements

6.4.1 Si_3N_4 tip/Mica in Air

Lateral stiffness (k_{tot}) was measured *vs.* load for a silicon nitride tip contacting freshly cleaved muscovite mica in humid atmosphere (~55% relative humidity (RH)) using a Si_3N_4 cantilever[15] with a nominal normal force constant 0.58 N/m (Figure 6.5 - crosses). k_{tot} shows a distinct load dependence with a good signal to noise ratio. The fit (Figure 6.5 - solid line) indicates how k_{tot} should vary with load, assuming the DMT model applies.

At 55% RH, a substantial water meniscus forms about the tip-sample contact. This

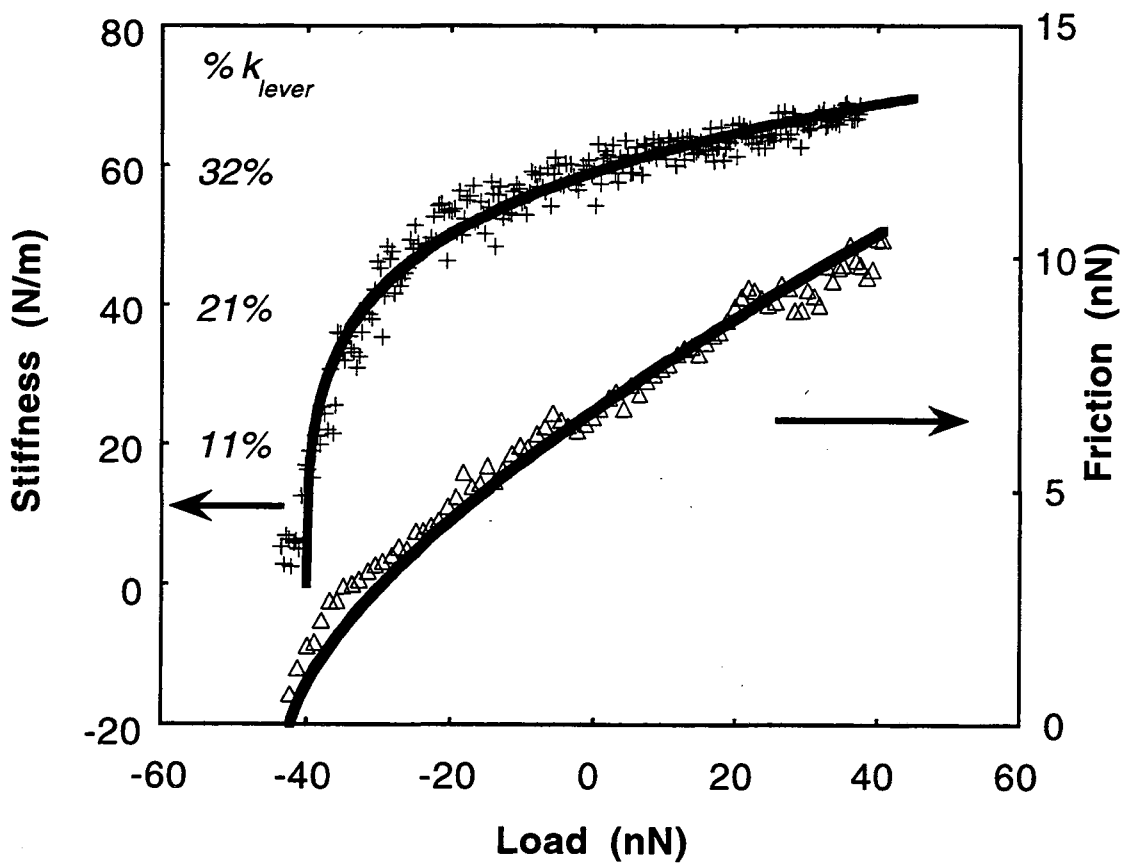

Figure 6.5 Crosses: lateral stiffness (k_{tot}) *vs.* load for a Si_3N_4 tip on mica in air. As load increases, k_{tot} asymptotically approaches k_{lever} (~190 N/m), although even at the maximum load, k_{tot} ~ 35% k_{lever}. Triangles: Ff *vs.* load, acquired shortly after the stiffness measurement. Solid lines: fits of the DMT model to both measurements.

can act like a long-range attractive force, and so the DMT model ought to apply. In fact, an exact treatment of the effect of capillary condensation upon contact areas has been formulated by Fogden and White[16] and Maugis[17]. The contact area depends upon the elastic constants, tip radius, and relative humidity. Using their model, we have determined that the DMT fit should apply in our case, at 55% RH. A more detailed discussion of this approach has been presented elsewhere[3].

We see in Figure 6.5 that k_{tot} only reaches 35% of k_{lever} at the highest load; in this case and in many other AFM experiments, the lateral contact deformation is equal to or greater than the lateral lever deformation for typical conditions[18].

From these results, we can determine the load dependence of τ. To do this, friction, F_f, was measured as a function of load (Figure 6.5 - triangles) immediately after the stiffness measurement. To see how τ varies with load, we can divide the measured friction by the square of the contact stiffness. Equations (6.1), (6.3) and (6.4) are combined to give

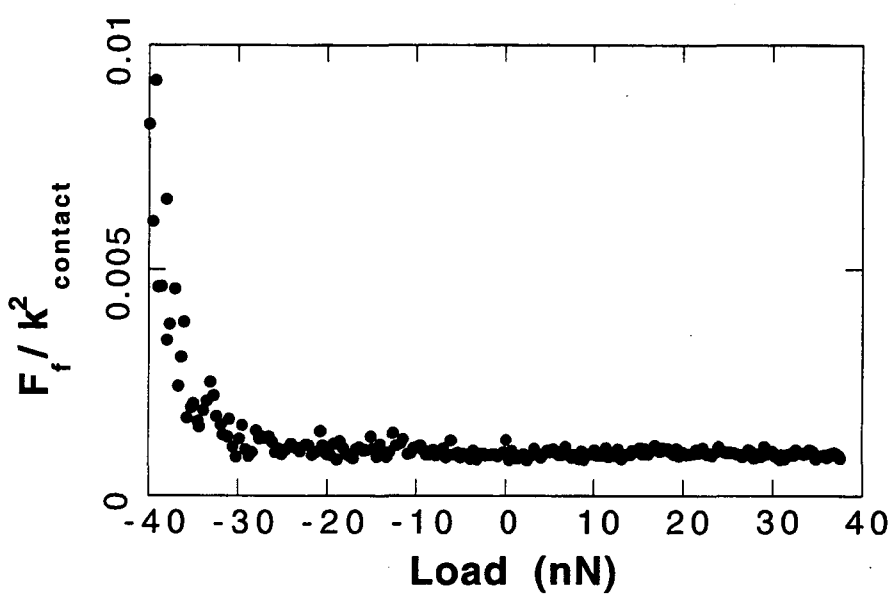

Figure 6.6 $F_f / k^2_{contact}$ *vs.* load for the Si_3N_4 tip on mica in air, calculated from the stiffness and friction data in Figure 6.5.

$$\frac{F_f(L)}{k_{contact}^2(L)} = \frac{\pi \cdot \tau(L)}{64 \cdot \left[G^*\right]^2} \propto \tau(L) \quad . \tag{6.10}$$

Therefore, our measurements give us a quantity that is proportional to the shear strength. Importantly, this equation is independent of the tip shape and dimensions, adhesion energy and adhesion force range. We calculate and plot this quantity at each load value from the separately acquired measurements of friction and stiffness. The result is plotted in Figure 6.6. For this measurement, τ appears to be independent of load, except near the pull-off point(~-40 nN). This low-load anomaly occurs because of slippage at low loads; this produces a stiffness measurement that is lower than the true value, so the apparent shear strength is higher than the true value. From the DMT fit to the friction data we calculate τ = 110 MPa.

6.4.2 Si_3N_4 tip/Mica in UHV

Friction and stiffness measurements were carried out in UHV for the same Si_3N_4-mica interface. Stiffness and friction *vs.* load are plotted in Figure 6.7. This time, we see that the data is fit very well by the JKR model. Our model-independent plot of $F_f/k_{contact}^2$ *vs.* load is shown in Figure 6.8. Again, the shear strength is seen to be load-independent. The JKR fit to the friction data gives τ = 52 MPa.

This example also shows that the contact area behavior depends strongly on the experimental environment. In air, the DMT model applies as a consequence of long-range capillary forces. In UHV, short range adhesion forces dominate and the JKR model applies. In both cases, the shear strength is experimentally observed to be load-independent.

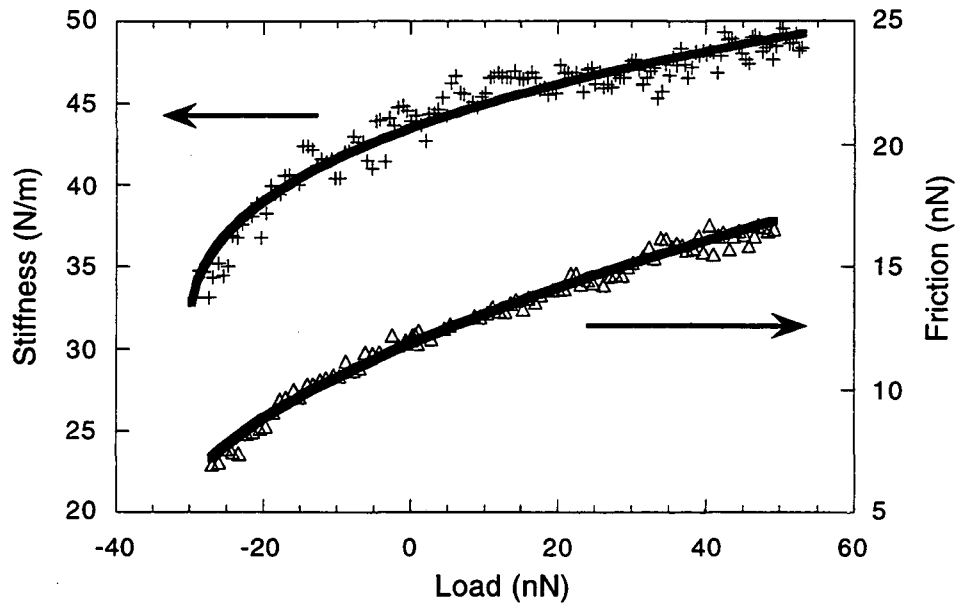

Figure 6.7 Crosses: lateral stiffness (k_{tot}) *vs.* load data for a Si_3N_4 tip on mica in UHV. Triangles: Ff *vs.* load, acquired shortly after the stiffness measurement. Solid lines: fits of the JKR model to both measurements.

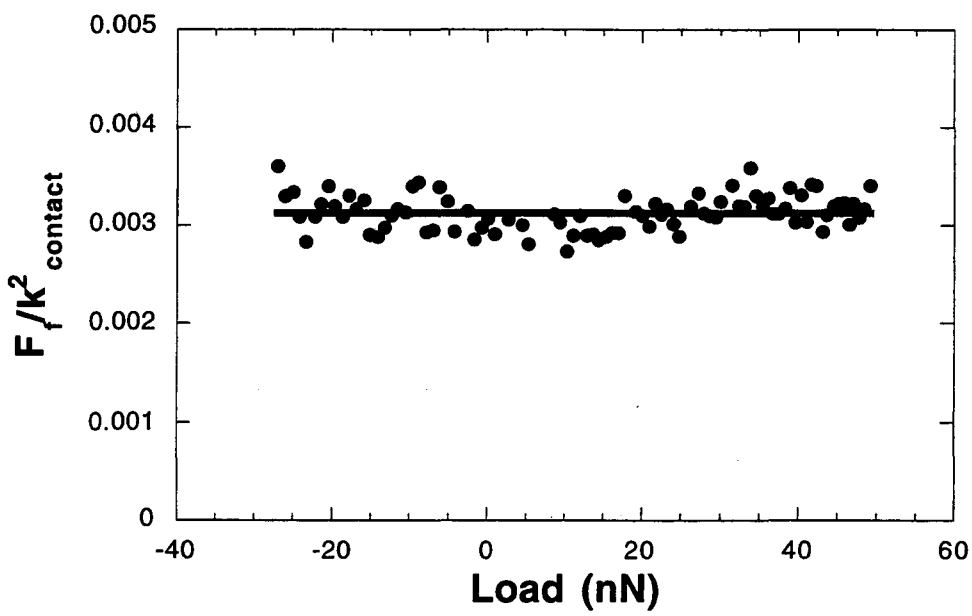

Figure 6.8 $F_f/k^2_{contact}$ *vs.* load for the Si_3N_4 tip on mica in UHV, calculated from the stiffness and friction data in Figure 6.7.

6.4.3 Si_3N_4 tip/NaCl in UHV

The measurements using the mica sample were relatively straightforward because the tip-sample frictional force prevented slippage during the measurement at most if not all loads. That is, the total lateral stress built up in the system at any point remained less than the critical lateral force at which the initial "slip" in stick-slip motion takes place (see Figure 6.2). If the critical lateral force is exceeded, the lateral stress will suddenly be relieved and so the resulting "amplitude" measured by the lock-in will be less than the no-slip value. This effect is manifested in the anamolously high apparent shear strength values near the critical load in Figure 6.6. Thus, it is important to prevent slippage from occurring during the measurement.

Slip can occur if substantial lateral thermal drift between cantilever and sample exists since this builds up additional lateral stress in the system during the measurement. More generally, as the load is changed, stress builds up in the cantilever along its long axis (longitudinal stress) because of the fact that AFM cantilevers are held at an angle with respect to the sample surface. This can lead to a slip event which involves lateral as well as longitudinal slip[19,20], as we described in Chapter 4. For some systems, friction will be so low that slip will occur throughout much of the measurement for this reason. We found this to be the case for friction between a Si_3N_4 tip and NaCl(100) in UHV. We observe that during a measurement, the system fluctuates between slip and no-slip conditions. Therefore, a fraction of the stiffness measurement points are invalid. As we stated in Section 6.3.1, we can monitor the out-of-phase response of the lock-in amplifier. Points associated with significant out-of-phase response can then be filtered from the data set. The end result is still not as accurate as measurements where slip is avoided, but at least some measurement can be made.

An example showing stiffness *vs.* load data before and after filtering is given in Figure 6.9. The unfiltered data appears nearly random. However, the filtered data is consistent with a JKR fit, as is the measured friction *vs.* load data (Figure 6.10). The

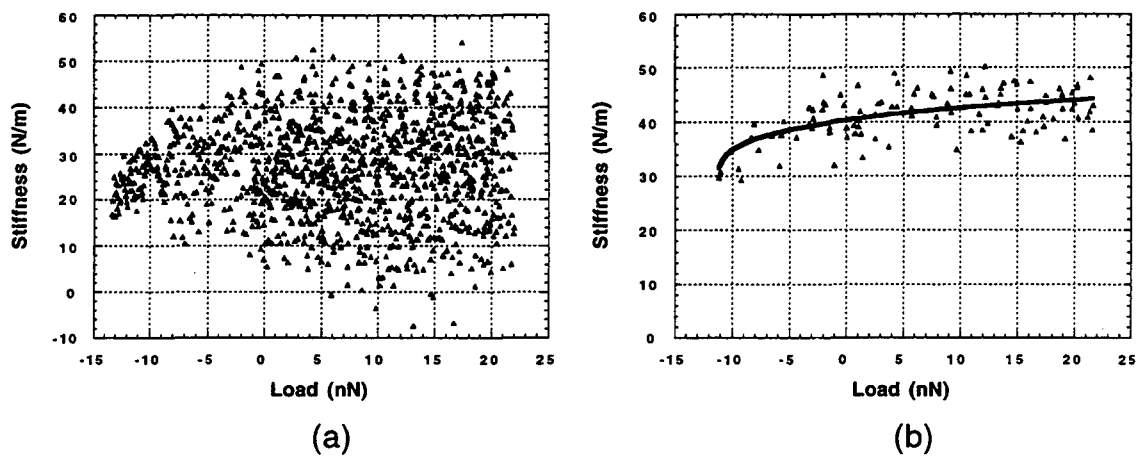

Figure 6.9 (a) Complete stiffness *vs.* load measurement for a Si_3N_4 tip on NaCl(001) in UHV. Huge fluctuations occur because of slip during the measurements. (b) The data in (a) after points corresponding to slip are removed. Solid line: JKR fit to the data.

filtering process thus allows us to plot $F_f/k^2_{contact}$ *vs.* load in Figure 6.11. From the JKR fit to the friction data, we calculate $\tau = 21$ MPa.

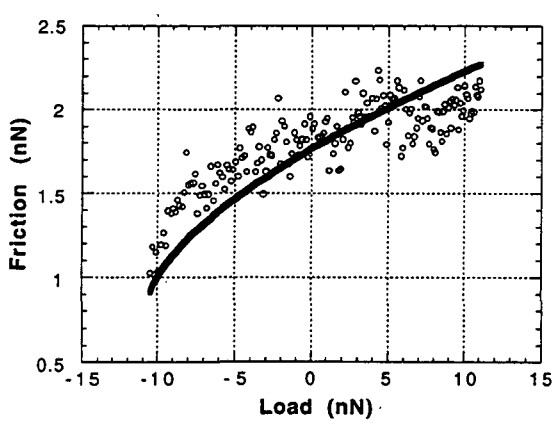

Figure 6.10 Circles: friction *vs.* load measurement for a Si_3N_4 tip on NaCl in UHV. Solid line: JKR fit.

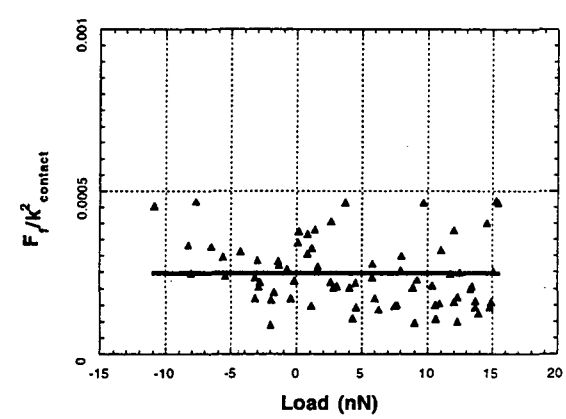

Figure 6.11 $F_f/k^2_{contact}$ *vs.* load for the Si_3N_4 tip on NaCl in UHV, calculated from the friction and filtered stiffness data above.

6.5 Deriving an Effective Modulus from Stiffness Measurements

We can use the contact mechanics fits to the stiffness data to back out a value for the combined shear modulus, G^*, by using equation (6.4), and compare this value to the expected bulk value. The bulk and derived values for G^* are listed in Table 6.1. To calculate G^* we used the following values of the elastic constants: G_{mica}=13.5 GPa, ν_{mica}=0.098[21], G_{NaCl}=24.6 GPa, ν_{NaCl}=0.20[22], G_{SiN}=61 GPa, ν_{SiN}=0.27[23].

The striking result is that the derived values of G^* do not match the bulk values. In all cases, the sample is much less stiff than the tip, and so the samples' elastic constants primarily determine the value of G^*. Therefore, it is possible that the bulk values of the samples' elastic constants are simply not correct. Local impurity or defect concentrations could affect the elastic constants. Furthermore, the shear modulus may be different from the bulk in the vicinity of the surface; only the first few atomic layers of the sample are involved in the elastic deformations that occur for these measurements. The first layer surface atoms may experience less restoring force because of having fewer neighbors, and so the shear modulus could be lower. Indeed, a theoretical study of an FCC Lennard-Jones solid predicted a 20% lower shear modulus for the surface layer[24]. However, this is nowhere near as large as the discrepancy we observe. To our knowledge, no other theoretical or experimental studies of the shear modulus for the surface atoms have been performed. Our technique may be the first observation of a low surface shear modulus at the nanometer scale. Further detailed studies would be required to investigate this

Table 6.1 Bulk and derived values of G^*

interface	G^*, bulk values (GPa)	G^*, from stiffness measurement (GPa)
Si_3N_4/mica in air	5.9	2.3±0.9
Si_3N_4/mica in UHV	5.9	1.0±0.4
Si_3N_4/NaCl in UHV	9.9	3.3±1.3

possibility.

Another possibility is that the continuum mechanics theories used to fit the contact area are quantitatively incorrect. The functional form of the equations, as seen in the figures above and in the previous chapter, are quite convincing. However, there are some refinements to these theories that have been proposed. In particular, Greenwood numerically solved the contact area problem assuming a Lennard-Jones interaction between a sphere and a plane[25]. This produces the JKR and DMT forms in the limiting cases, but also provides solutions for intermediate cases (*i.e.* for $0.1<\mu_T<5$, where μ_T is defined in equation (5.9)). By defining the contact radius as the radius at which the Lennard-Jones attractive stress is maximal, he found that area-load curves resemble the JKR curves in their shape, for values of $\mu_T>0.5$. An analytic form by Maugis for solutions within the JKR-DMT transition[26] was adapted by Johnson[27] where he defined a distinct effective area of contact. Similar to Greenwood's results, Johnson's model produces curves that resemble the JKR curve even when μ_T is not in the JKR regime.

Following on this, Johnson fit this effective contact area to friction data obtained by this author[27], specifically the data presented in Figure 5.4(a). The curve agreed nearly as well as the JKR fit. If Johnson's model is correct, then by using the JKR model the contact area is overestimated by about 15%. An overestimation by this amount is still not large enough to account for the discrepancies we observe in G^* for the data presented here. One complication that arises from fitting Johnson's model is that one must assume a value for z_0, the unknown range of attractive forces that appears in equation (5.9), although this value should be roughly of atomic dimensions. A worthwhile future goal would be to investigate in detail how well this model fits other friction and stiffness data. Notably, Lantz *et al.* have found agreement with this model for measurements with Si tips on $NbSe_2$ in UHV[28].

6.6 Correct Measurement of Friction

The effect of contact stiffness has manifestations for the correct measurement of

friction forces where stick-slip occurs. The frictional force F_f that we have discussed throughout this chapter and Chapter 5 corresponds to the maximum value of the lateral force during sliding as defined in Figure 4.1 of Chapter 4 as well as Figure 6.12 here. This definition differs from that discussed in other publications[2,3,29]. In those papers, the *average* value of the difference in bi-directional lateral force signals is calculated at each load. This average value, F_{ave}, is incorrect when stick-slip motion is taking place. When the stick-slip amplitude is significant compared with the friction force, a load-dependent shift in the average friction compared to F_f will occur and so fitting a particular contact mechanical model to such data could lead to erroneous conclusions. This occurs essentially because the stick-slip amplitude changes with contact stiffness, *i.e.* with load.

This problem is illustrated schematically and with actual friction data in Figure 6.12. It is seen from the data in Figure 6.12 that neither the stick-slip amplitude nor the *change* in the stick-slip amplitude with load is negligible compared with the magnitude of the friction force. Thus, F_{ave} essentially mixes different physical quantities. This has not been previously considered by other researchers who utilize schemes such as the "2D histogram technique"[25] and straight averaging of the friction data, in which the aforementioned error will be inherent. Only sometimes will it be negligible.

For our analysis, we have developed a software routine that calculates the average values of the *maximum* lateral force scanning in each direction at a given load. We then take half of the difference between these two values, and plot this as the friction force F_f. In Figure 6.13, we show both F_f and F_{ave}, plotted *vs.* load for the Si_3N_4 tip on mica in air. We see that the difference is substantial. We emphasize that the physically meaningful force here is *the lateral force required to initiate shear, i.e. to cause slip.* It is this quantity that we have compared to the contact area in our measurements.

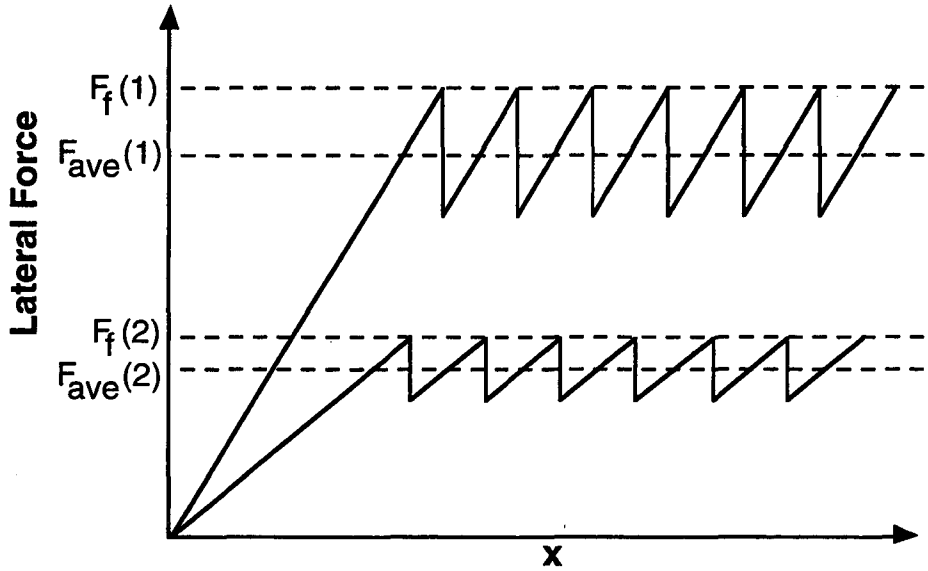

Figure 6.12 Schematic diagram (above) of the lateral force response at high load / high contact stiffness (1) and low load / low contact stiffness (2). The force at which slip occurs, F_f, and the average value of the force, F_{ave}, are indicated. F_f and F_{ave} are offset from each other by a load-dependent amount, due to the change in contact stiffness with load. Real data (below) shows the effect is observable.

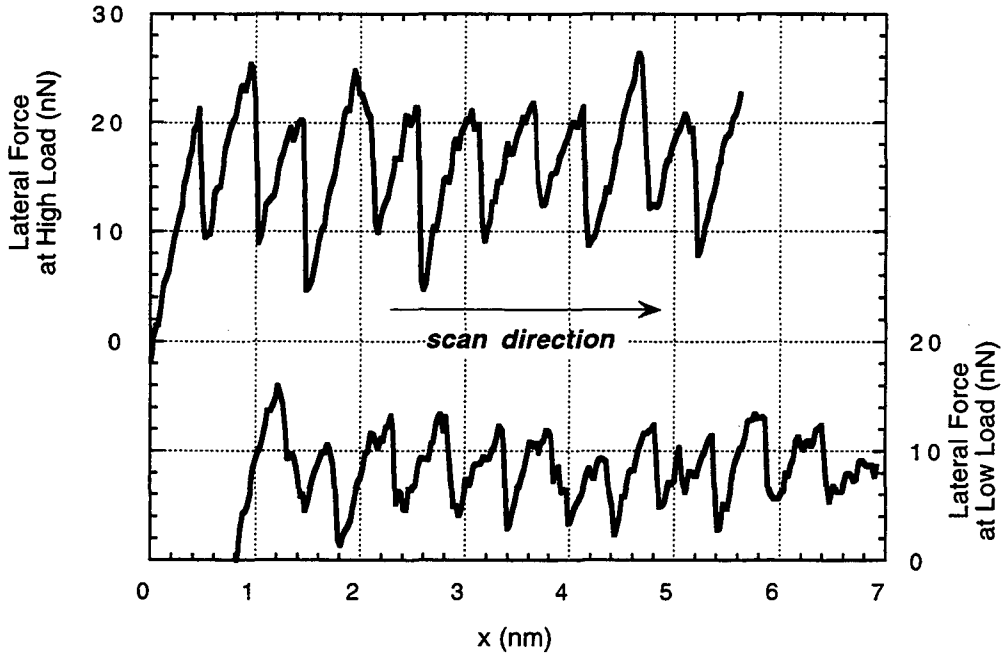

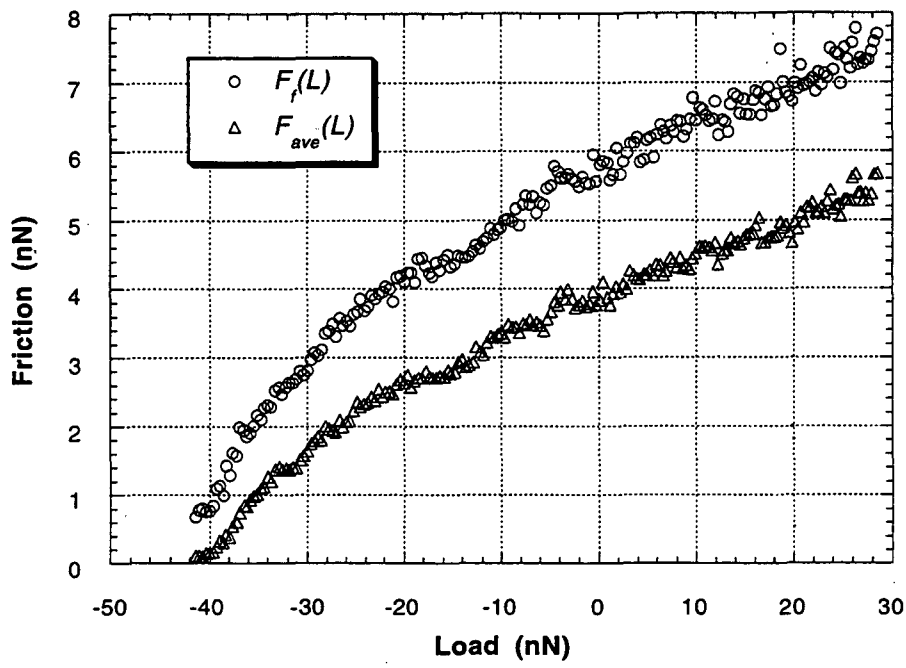

Figure 6.13 Maximum friction, F_f, and average friction, F_{ave}, measured as a function of load for a Si_3N_4 tip on mica in air. The difference is substantial and varies with load.

6.7 Summary

We have described a technique to measure the lateral stiffness of a nanometer-sized contact formed between a AFM tip and a sample surface. AFM cantilevers possess stiffness values comparable to the lateral contact stiffness and thus are optimum for performing the measurement. The measurement is proportional to the contact radius, which can then be compared to sliding friction measurements to determine the load dependence of shear strengths independent of contact mechanical models. The technique is straightforward and quick to perform. In general, we conclude that friction and lateral stiffness measurements are complimentary techniques which should be employed in tandem when studying nanotribology with AFM.

Our measurements on three different systems appear to indicate that the bulk values of the elastic constants are incorrect at the nanometer scale, although the quantitative application of contact mechanics models may also be incorrect. Further measurements

should be performed to quantify and investigate this discrepancy further.

Finally, understanding the concept of contact stiffness also allows for proper definition of friction in the stick-slip regime.

Chapter 6 References

[1] R. W. Carpick, D. F. Ogletree, and M. Salmeron, Appl. Phys. Lett. **70** (1997).

[2] J. Hu, X.-D. Xiao, D. F. Ogletree, and M. Salmeron, Surf. Sci. **327,** 358 (1995).

[3] U. D. Schwarz, W. Allers, G. Gensterblum, and R. Wiesendanger, Phys. Rev. B **52,** 14976 (1995).

[4] E. Meyer, R. Lüthi, L. Howald, M. Bammerlin, M. Guggisberg, and H.-J. Güntherodt, J. Vac. Sci. Technol. B **14,** 1285 (1996).

[5] R. W. Carpick, N. Agraït, D. F. Ogletree, and M. Salmeron, J. Vac. Sci. Technol. B **14,** 1289 (1996).

[6] B. J. Briscoe and D. C. B. Evans, Proc. Roy. Soc. Lond. A **380,** 389 (1982).

[7] R. S. Timsit, in *Fundamentals of Friction*, edited by I. L. Singer and H. M. Pollock (Kluwer, Dordrecht, 1992), p. 287.

[8] I. L. Singer, R. N. Bolster, J. Wegand, S. Fayeulle, and B. C. Stupp, Appl. Phys. Lett. **57,** 995 (1990).

[9] S. P. Jarvis, A. Oral, T. P. Weihs, and J. B. Pethica, Rev. Sci. Instrum. **64,** 3515 (1993).

[10] D. F. Ogletree, R. W. Carpick, and M. Salmeron, Rev. Sci. Instrum. **67,** 3298 (1996).

[11] K. L. Johnson, *Contact Mechanics* (University Press, Cambridge, 1987).

[12] K.L. Johnson (personal communication).

[13] J. Colchero, M. Luna, and A. M. Baro, Appl. Phys. Lett. **68,** 2896 (1996).

[14] M. A. Lantz, S. J. O'Shea, A. C. F. Hoole, and M. E. Welland, Appl. Phys. Lett. **70,** 970 (1997).

[15] Nanoprobe, Digital Instruments, Santa Barbara, CA.

[16] A. Fogden and L. R. White, J. Colloid Interface Sci. **138,** 414 (1990).

[17] D. Maugis and B. Gauthiermanuel, J. Adhes. Sci. Technol. **8,** 1311 (1994).

[18] J. Colchero, A. M. Baro, and O. Marti, Trib. Lett. **2,** 327 (1996).

[19] S. Morita, S. Fujisawa, and Y. Sugawara, Surf. Sci. Rep. **23,** 3 (1996).

[20] D. F. Ogletree, R. W. Carpick, and M. Salmeron, in preparation (1997).

[21] L. E. McNeil and M. Grimsditch, J. Phys: Condens. Matter **5,** 1681 (1992).

[22] N. W. Ashcroft and N. D. Mermin, *Solid State Physics* (Holt, Rinehart and Winston, New York, 1976).

[23] Dr. M. Tortonese, Park Scientific Instruments Inc., Sunnyvale, CA (personal communication).

[24] J. P. Eerden, H. J. F. Knops, and A. Roos, J. Chem. Phys. **96,** 714 (1992).

[25] J. A. Greenwood, Proc. Roy. Soc. Lond. A **453,** 1277 (1997).

[26] D. Maugis, J. Colloid Interface Sci. **150,** 243 (1992).

[27] K. L. Johnson, Proc. Roy. Soc. Lond. A **453,** 163 (1997).

[28] M. A. Lantz, S. J. O'Shea, M. E. Welland, and K. L. Johnson, Phys. Rev. B **55,** 10776 (1997).

[29] R. Lüthi, E. Meyer, H. Haefke, L. Howald, W. Gutmannsbauer, M. Guggisberg, M. Bammerlin, and H.-J. Güntherodt, Surf. Sci. **338,** 247 (1995).

7. Frictional Properties and Surface Modification of Potassium Halide Substrates

7.1 Introduction

The investigations reported in the previous chapters concerned friction in the apparently wearless regime, where tip-sample interactions are elastic. However, in macroscopic tribological situations, inelastic processes play an important and often dominant role in sliding contacts. Wear processes are considerably more complex to study, and so a systematic investigation of related materials would be desirable, to correlate observed tribological behavior with the materials' properties. We have thus studied a series of alkali halide single crystals where only the halogen ion is varied, namely KF, KCl and KBr. These particular alkali halides are relatively soft and so it ought to be possible to initiate wear at low loads without seriously damaging the AFM tip.

In general, alkali halides present relatively inert surfaces because of the closed-shell nature of the ionic bonding. Surfaces with atomically flat terraces can be prepared by cleavage in ultrahigh vacuum (UHV). An important difference amongst these materials is the different ionic radius of the anion. Almost all physical properties of these crystals (lattice constant, binding energy, elastic constants, etc.) vary from one material to the other in the same order as the anionic radii. Our goal is thus to examine whether observed friction and wear properties also vary in such a fashion.

While the bulk properties of alkali halide materials have been extensively studied, surface properties have received less attention[1]. The strongly insulating nature of these materials renders electron spectroscopy methods, so common for surface science investigations, difficult to utilize. Specifically, the understanding of surface defects of these materials remains minimal. With AFM, of course, sample conductivity is not

required of samples under investigation.

7.2 Properties of Potassium Halides

Various relevant physical properties of KF, KCl and KBr are listed in Table 7.1. The materials are listed in order of increasing anionic radius, which naturally corresponds to increasing atomic number. These materials all form the NaCl "rocksalt" structure, an FCC lattice with a basis of two atoms, the cation and anion. This structure is illustrated in Figure 7.1. The highly ionic bonding character allows one to describe the ions as being packed like billiard balls whose radii are equal to the respective ionic radii[2]. The F^- and K^+ ions actually posses similar radii which leads to efficient packing of the ions and hence to the smallest nearest-neighbor distance of 0.267 nm. The larger Cl^- ion results in a significantly larger nearest-neighbor distance of 0.315 nm. Br^- is slightly bigger than Cl^- and correspondingly KBr has a nearest-neighbor separation slightly larger than KCl of 0.330 nm. Similarly, the cohesive energies of KCl and KBr are nearly the same, with KCl slightly more strongly bound. The binding of KF significantly stronger than both[3]. The elastic properties as exemplified by the Young's modulus vary in a similar fashion[4].

Another important mechanical property is the yield strength. However, yield strength measurements are macroscopic in nature and thus invariably determined by dislocation behavior. The nanometer-sized contacts relevant for AFM may in fact possess

Table 7.1 Properties of potassium halide crystals

sample	cation (K^+) radius (nm)	anion radius (nm)	lattice periodicity d (nm)	cohesive energy (eV/ion pair)	Young's modulus (GPa)	ideal strength (GPa)
KF	0.133	0.136	0.378	8.2	60	1.3 - 2.6
KCl	0.133	0.181	0.445	7.2	39	0.63 - 1.3
KBr	0.133	0.195	0.467	6.9	33	0.53 - 1.0

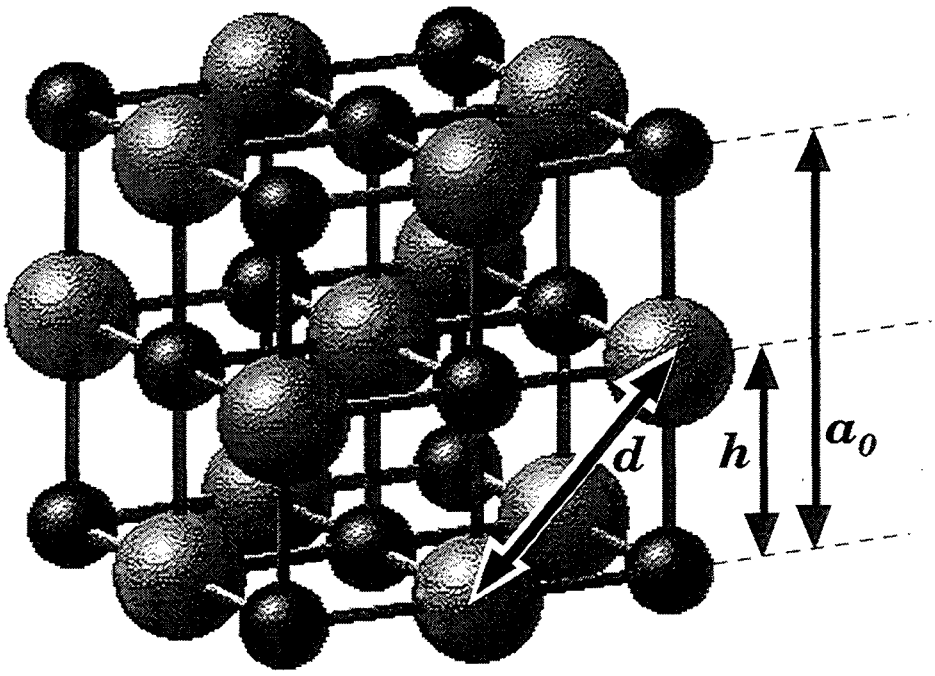

Figure 7.1 The rocksalt structure. Cations (small dark spheres) and anions (large light spheres) are arranged in an FCC lattice whose basis consists of a cation at (0,0,0) and an anion at (1/2,1/2,1/2). Indicated here are the dimensions of the conventional unit cell a_0, the ion periodicity h (= $a_0/2$, which is the nearest-neighbor distance), and the lattice periodicity d (= $a_0/\sqrt{2}$) which is the nearest separation of equally-charged ions. The monatomic step height is equal to h. The values of d for the three materials studied are given in Table 7.1. The ionic radii in the drawing are reduced from the actual values to display the structure more clearly.

yield strengths closer to the theoretical ideal[5] which for ionic materials, as with others, are proportional to the elastic constants[6]. We expect, based on other work with nano-scale contacts[7], that the strength of these materials at the nanometer scale will vary accordingly. Specifically, the ideal yield strength of these materials is estimated to be within G/10 and G/5, where G is the shear modulus, and this range of values is indicated in Table 7.1.

In general the potassium halides are more weakly bound and thus less stiff and less strong than the corresponding sodium or lithium halides. Obviously, smaller ionic radii leads to stronger bonding since the electrostatic forces which bind the crystal together are stronger at shorter range.

In this chapter, we again present results obtained using contact-mode AFM. As discussed previously, we do not expect contact-mode AFM to resolve individual atoms, nor point defects because it is impossible, even at the lowest loads, to obtain a single-atom contact[8]. The contact area will involve at least a few unit cells if not tens or hundreds. This is commonly revealed in AFM imaging by the lack of observation of point defects, as well as by the apparent width of atomic steps. True atomic resolution can in fact be obtained with AFM by using a non-contact dynamic force modulation technique[9]. Recently Bammerlin *et al.* succeeded in applying this technique to the surface of NaCl(001) in UHV and individual point defects were observed[10].

7.3 Experimental Section

For these experiments, we used commercially obtained high-purity optical grade single crystals of KBr and KCl[11], and a laboratory-grown high purity single crystal of KF[12]. Crystals were mounted with epoxy into a sample holder. Once in UHV, crystals were cleaved using a knife-edge, producing an optically flat (001) plane. All measurements were performed at room temperature with the chamber pressure below $5 \cdot 10^{-10}$ Torr. The same silicon nitride cantilever was used for all experiments[13]. The force constant of the cantilever was estimated to be 0.11 N/m, derived from the calculations described in Chapter 3. The relative lateral force to normal force sensitivity ratio of this lever was experimentally determined using the "wedge" calibration technique of Chapter 3. A nanometer scale profile of the tip was obtained using the $SrTiO_3$(305) tip imaging technique described in Chapter 5. The tip shape was confirmed to be essentially parabolic with a curvature radius of 45±5 nm.

Two types of data are presented in this chapter. Images were obtained in the usual "topographic mode" by maintaining a constant applied normal force, while simultaneously recording the lateral force signal. Friction *vs.* load plots were obtained by plotting the average difference in bi-directional lateral force signals during a 10 nm lateral scan on an atomically flat terrace for a series of loads, as described in Chapter 5.

7.4 Results

7.4.1 Sample Topography

Images were acquired as soon as 20 minutes after cleavage of the crystals. Surface structures (*i.e.* steps) remained stable over periods of several hours (changes to the surface induced by tip-sample contact will be discussed in Section 7.4.2).

In all cases, vacuum cleavage produces flat terraces with lateral dimensions of typically several hundreds of nanometers. Many steps are observed and are overwhelmingly monatomic steps, *i.e.* the step height $h = a_0/2$ where a_0 is the conventional unit cell size. This corresponds to a single (001) slab of material. The steps are oriented predominantly, but not exclusively, along the [100] and [010] lattice directions (Figure 7.2). We determined this by observing the relative alignment of these steps to be 90°, and

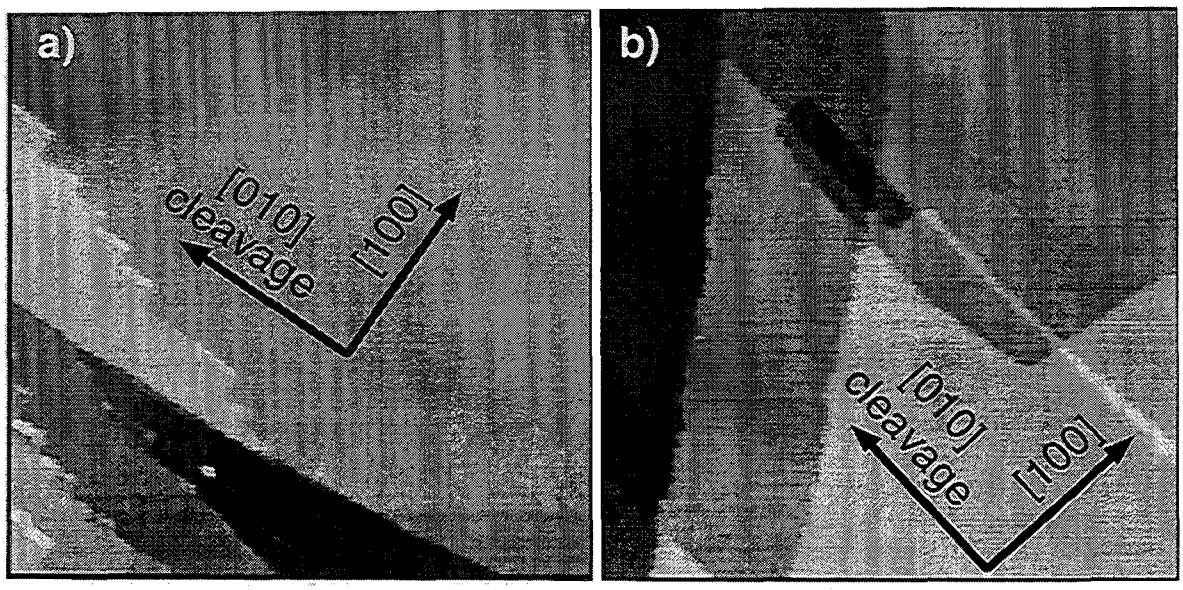

Figure 7.2 (a) 400×400 nm^2 topographic image of KCl(001) showing a large flat terrace and several steps in the lower left part of the image. The steps are oriented primarily along the <100> and <010> directions. Note the thin bright lines representing material present at certain step edges. These structures are 0.26 ± 0.02 nm high, which is equivalent to the KCl step height of 0.267 nm. We believe the bright lines are simply a narrow strip of KCl. The strips are exclusively present on steps along <100>, which may be a consequence of the cleavage dynamics. (b) 400×400 nm^2 topographic image of KBr(001). Monatomic steps are seen, some of which cross each other. Some are oriented along low index directions as indicated, although two kinked steps are seen which are not oriented as such.

comparing their orientation to the direction of rows in the lateral force stick-slip images which were discussed in Chapter 4. The direction of these steps is also consistent with the orientation of the crystal in the sample holder. We refer to these steps as "low index steps".

In Figure 7.2(b) we see an example from the KBr surface. Along with low index steps we also see two kinked steps oriented in a unique direction. The low index steps are seen to cross each other as well as the kinked steps. The low index steps are most likely the result of edge or screw dislocations that are exposed by cleavage. It is energetically favorable for dislocation features to run along low index directions. Figure 7.3 shows three screw dislocations (marked by arrows) exposed on the surface of KCl with low index steps emanating from the origin of the dislocation.

Highly stepped regions are observed as well. An example from the KF surface is

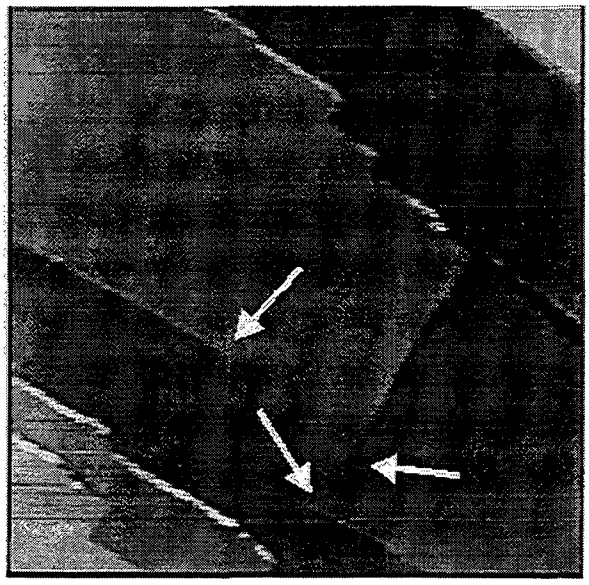

Figure 7.3 620×620 nm^2 topographic image of KCl(001). Three screw dislocations are present, with monatomic low index steps emerging from the point where the dislocation line intersects the cleavage surface. This is in agreement with the known Burgers vectors for rocksalt structures[6].

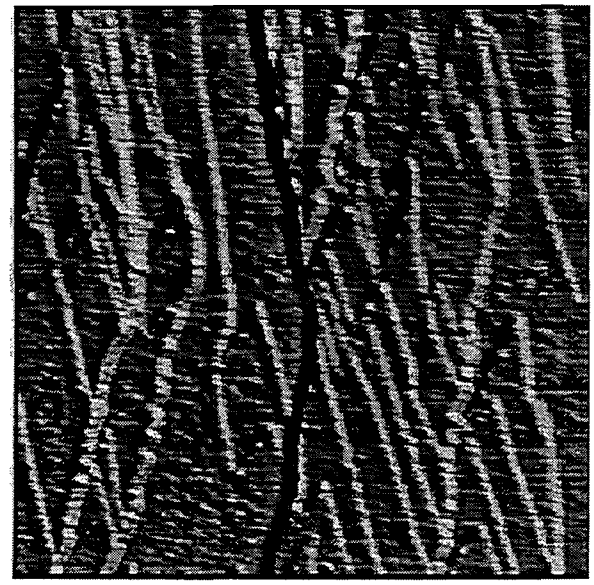

Figure 7.4 1.2×1.2 μm^2 topographic image of KF(001) showing a highly stepped region of the crystal. The image is presented in light-shaded mode to reveal the step structure clearly.

shown in Figure 7.4. Numerous pointed terraces with relatively consistent opening angles are present. Areas with large terraces were also observed on this sample. These regions may be the result of the interaction between preexisting dislocations and the cleavage process.

The steps observed on these surfaces in vacuum are markedly different than those observed on surfaces imaged in laboratory atmosphere. At various humidities, steps on rocksalt crystal surfaces are observed to have rounded shapes[14]. Increased mobility of surface ions due to hydration allows step flow to occur, leading to an equilibrium configuration.

These results demonstrate that interesting structural surface properties such as steps can be studied with AFM. A systematic study of the structure and conditions leading to these steps was however not the main emphasis of this work.

7.4.2 Friction: Domains and Load Dependence

The most remarkable phenomenon observed during these measurements was the existence of higher friction domains on the terraces which appeared after the tip made contact with the sample, and continued to grow with successive scans. In Figure 7.5, we show an example of this phenomenon on the KBr surface. The topographic image, Figure 7.5(a), shows a number of atomically flat terraces separated by monatomic low index steps. Figure 7.5(b) is the simultaneously acquired lateral force image. Two distinct friction domains are observed. Some domains are bound by steps, but sometimes their boundary exists on the terrace itself. Most of the boundaries on terraces in this example are oriented roughly perpendicular to the low index steps, *i.e.* along the [100] direction. The higher lateral force is consistent between both left-to-right and right-to-left scans, therefore the two domains correspond to regions of lower and higher friction force. These differences between the domains are not visible in the topographic image. If any topographic contrast exists between the domains on the KBr surface, it is less than the noise level of 0.02 nm.

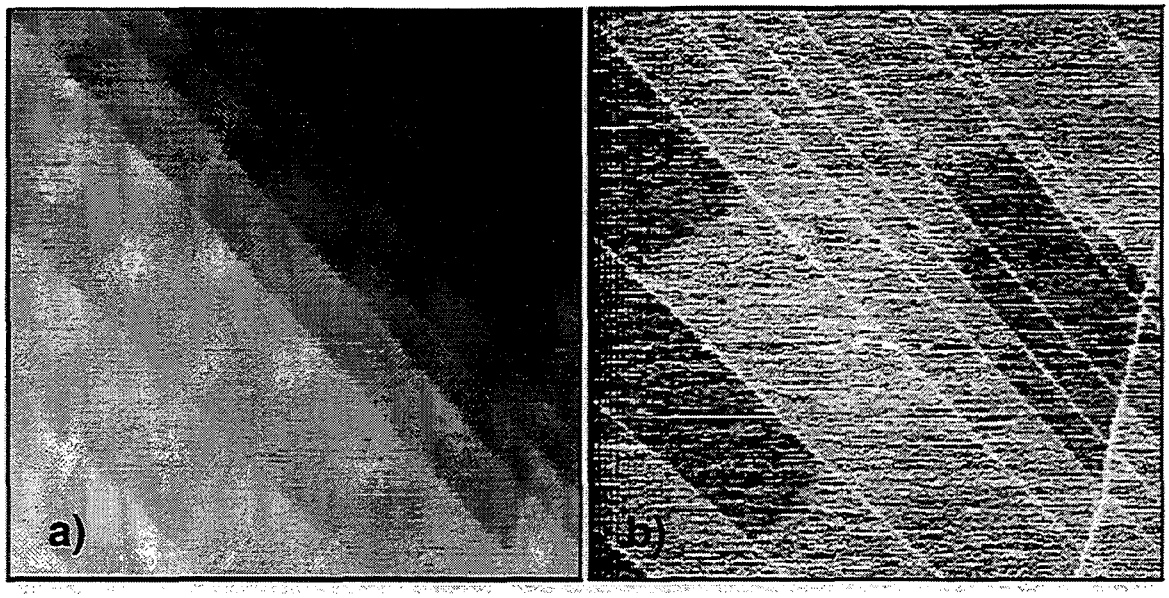

Figure 7.5 Topographic (a) and simultaneous lateral force (b) images of a 1.2 × 1.2 μm^2 region of KBr with a number of low index monatomic steps present. The lateral force image shows clearly resolved domains of low (dark) and high (bright) friction on the terraces. In this example, the domains are sometimes bound by steps but are also bound on terraces themselves perpendicular to the low index steps. There is no apparent topographic contrast corresponding to the friction domains.

The higher friction domains exist within the imaging region and spread between successive scans. This indicates that the low friction domains are associated with the native cleaved surface, while the high friction domains are induced by tip-sample contact. A series of images demonstrating the domain growth is shown in Figure 7.6. Figure 7.6(a) is a 1.2 × 1.2 μm^2 topographic image of the KBr surface in a region with a rather interesting and complicated step structure. Figure 7.6(b) is the corresponding lateral force image and Figure 7.6(c)-(g) are subsequent lateral force images. Figure 7.6(d)-(f) are 2.5 × 2.5 μm^2 scans, larger than the original scan area.

The high friction domains are seen to spread out across terraces and appear to continue outside of the imaging region even though scanning has not occurred there. Some regions remain unaffected even though they are surrounded by high friction domains. Between Figure 7.6(b) and (c) there is a region indicated on a terrace which initially was part of a high friction domain, but has then reverted to a low friction domain while a high

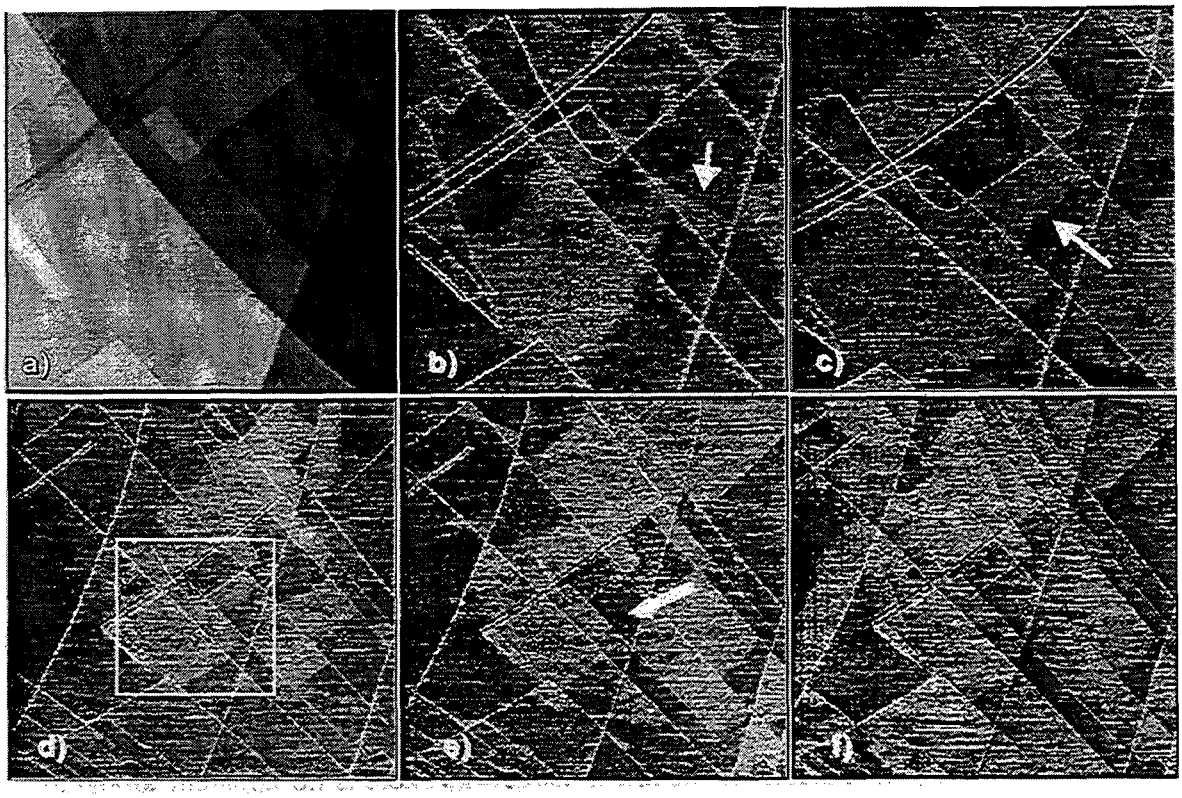

Figure 7.6 (a) 1.2 × 1.2 μm^2 topographic image of KBr. (b) Simultaneous lateral force image. (c) - (f) Subsequent lateral force images: (c) 2nd scan (d) 3rd scan (e) 6th scan (f) 13th scan. Note: (d)-(f) are 2.5 × 2.5 μm^2 images of the same region, with the imaging region for (a) indicated by the white box. There is some lateral drift between images. High friction domains grow from one scan to the next. The terrace indicated by the arrow in (b) initially has a high friction domain covering part of it which reverts to low friction (c) -(d), while another part of the terrace is converted to a high friction domain. Later, the entire terrace reverts to low friction again (e). Most of the other high friction domains remain once formed. Domains appear to be growing beyond the scan area.

friction domain appears elsewhere on the terrace. Later on, in Figure 7.6(e), the entire terrace has reverted to a low friction domain. In this series of images some of the domain boundaries are curved or are not aligned perpendicular to the low-index steps as in Figure 7.5, although some domain boundaries are aligned as such. The average ratio of friction forces between high and low friction domains on the KBr surface is 1.24 ± 0.03.

Often the very first image of a new surface region contains these domains as the tip has already made contact with the surface region during the approach cycle. Since contact is necessary for scanning, it was not possible to determine whether the domain formation

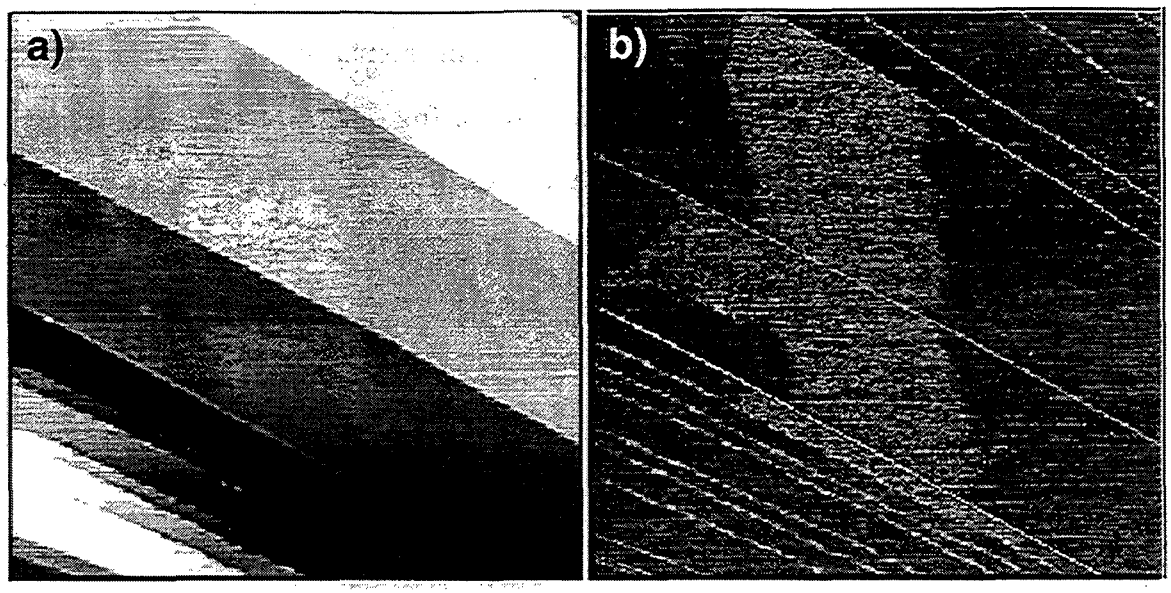

Figure 7.7 (a) Topographic image of a 1.2 × 1.2 μm^2 region of KCl. (b) Simultaneous lateral force image. As with KBr, a connected high friction domain has appeared on some of the terraces. The topographic contrast associated with high friction domains is approximately 0.04 ± 0.02 nm.

was due to contact itself (*i.e.* normal forces) or scanning (*i.e.* lateral forces).

This phenomenon was observed on the other samples as well but with different characteristics. An example from the KCl surface is shown in Figure 7.7. The friction contrast is significantly higher (1.79 ± 0.17). This time, there is a small but observable topographic contrast between high and low friction domains of 0.04 ± 0.02 nm. Like the KBr surface, the high friction domains spread out on terraces from one scan to the next and form several continuous domains, often bound by steps.

As with KBr and KCl, friction domains which spread from one scan to the next appeared on the KF surface as well, but with significantly different properties. The topographic contrast of the domains, 0.20 ± 0.03 nm, was substantially larger than with KBr and KCl. The friction contrast between domains was also higher, 2.3 ± 0.2. The lateral domain structure was also distinct. While the high friction domains on KBr and KCl formed large connected domains, the high friction domains on KF were generally disconnected. This is illustrated in Figure 7.8. Figure 7.8(a) and (b) show, respectively,

topographic and lateral force images of a 1.2 × 1.2 μm^2 region of KF which includes a step. The topographic contrast of the domains is not far from the KF step height of 0.267 nm. The subsequent lateral force image, Figure 7.8(c), shows that the area converted to high friction domains increases, but the domains are often disconnected or possess rough boundaries. The domain properties for all three materials are summarized in Table 7.2. The domain properties are clearly correlated with the materials' properties as exemplified by the Young's modulus, anionic radius and cohesive energy.

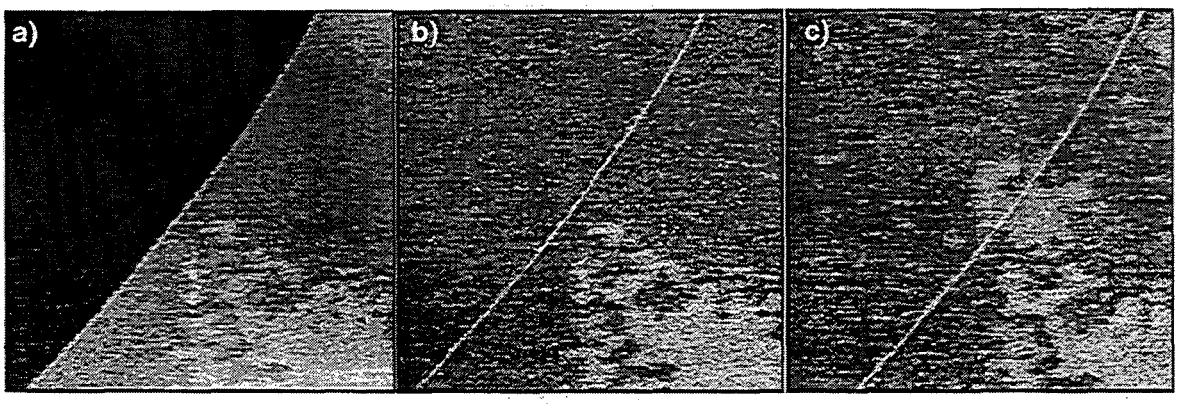

Figure 7.8 (a) Topographic image of a 1.2 × 1.2 μm^2 region of KF. (b) Simultaneous lateral force image. (c) Subsequent lateral force image, 4 scans later. High friction domains grow from one scan to the next. The topographic contrast of the domains is approximately 0.20± 0.03 nm. The domains are more disconnected than with KBr and KCl and have rougher boundaries.

Table 7.2 Properties of friction domains

sample	anion radius (nm)	domain height (nm)	adhesion - high friction domain (nN)	adhesion - low friction domain (nN)	domain friction contrast (hi:lo)	lateral structure
KF	0.136	0.20 ± 0.03	4.6 ± 0.5	4.7 ± 0.6	2.3 ± 0.2	disconnected
KCl	0.181	0.04 ± 0.02	2.7 ± 0.5	2.9 ± 0.4	1.79 ± 0.17	connected
KBr	0.195	< 0.02	3.2 ± 0.3	3.4 ± 0.2	1.24 ± 0.03	connected

The nature of these domains is striking but unknown. We know of no previous reports of similar observations. Nor have we observed similar phenomena on UHV FFM measurements with mica or NaCl samples which were described in Chapters 5 and 6. We can rule out the possibility of accumulation of contamination on the surface from the background since the occurrence of domains is always associated with tip-sample contact: after moving from a heavily scanned area where many high friction domains have been created, a newly imaged region will have only a few high friction domains which again increase as scanning/contact proceeds. Therefore, two possibilities exist:

1. The domains are produced by contamination transferred from the tip to the sample.
2. Tip-sample contact mechanically alters the sample by modifying the organization or density of surface or near-surface atoms. This structural change may involve surface or sub-surface defects such as vacancies or interstitials, or relative motion causing misfit or misalignment of near surface layers, and is produced by the substantial stresses present around the tip-sample contact zone.

The results we have obtained so far are not conclusive enough, nor is the present day understanding of nanometer scale tribology comprehensive enough, to allow us to categorically confirm either of these possibilities. However, several factors favor the second explanation. Although there is some observable shifting of the domain boundaries, once they are formed they are generally maintained. There is no sign of destruction of a layer of contamination by the tip. For example, no domains were observed to have boundaries or modifications along the scan direction. Yet one might expect to be able to modify a contamination or adsorbate layer with the tip, as observed for example by Lüthi *et al.* in the case of C_{60} and AgBr islands on NaCl on UHV[15]. Repeated attempts at this were unsuccessful. At very high loads, the tip gouged through the surface producing a hole. This will be discussed further below. It was not possible to alter a high friction domain without altering the substrate itself. Therefore, if the high friction domains are a contamination layer then they are very strongly bound to the substrate. It is surprising that

material which could readily transfer from the tip to the substrate could then be strongly bound to the substrate especially considering the inert quality of alkali halide surfaces.

No reduction in the rate of domain formation was observed during the experiment. If contamination from the tip occurred, then the source was never depleted during the course of the experiment, which was 14 days of data acquisition involving over 400 images. It seems surprising that tip contamination could persist for such a duration, whereas surface alteration obviously would occur steadily.

Furthermore, it is peculiar for a contamination layer to exhibit different topographic contrast on the different materials. However, it is conceivable that the topographic properties of surface structures associated with defects ought to vary with the type of material. Let us assume that interstitial creation is occurring. Packing ions into interstitial positions when the neighbors are of the same size (as with KF) will necessitate more rearrangement of the neighbors than packing a much smaller ion (as with KCl or KBr). Indeed, we observe that the topographic contrast is greatest for KF (0.20 nm, compared to 0.04 nm or less for KCl and KBr), where the anion and cation are nearly equal in size.

Tip-sample adhesion was measured on high and low friction domains on all three materials by measuring pull-off forces (see Table 7.2). On each material, there was no difference in the measured pull-off force between high and low friction domains. As discussed in Chapter 5, adhesion depends upon surface and interfacial energy, and so not surprisingly it has been observed that chemically distinct surfaces exhibit distinct pull-off forces[16,17].

The lack of adhesion contrast between domains despite the presence of significant friction contrast on *all three* materials is challenging to explain if the domains are assumed to be contaminants, since contamination is expected to change the adhesion. However it is conceivable that structurally distinct domains would not produce significant adhesion contrast. Although it is not known exactly how adhesion depends upon atomic structure, adhesion may not be strongly affected by atomic scale roughening or disorder as it may be

determined by electrostatic or van der Waals' forces whose effect goes beyond the surface layer. On the other hand, atomic scale roughening could strongly affect friction by presenting a "bumpy path" which the tip needs to traverse. Furthermore, the presence of defects provides a number of new vibrational modes for energy dissipation, particularly soft modes associated with vacancies and interstitials which lead to facile atom displacement.

Figure 7.5 shows that some terraces remain unaffected while high friction domains have been born on neighboring terraces. It would be surprising that contamination would so strongly favor a particular terrace for growth while completely avoiding a neighboring terrace. Furthermore, as seen in Figure 7.6, a large domain can appear from one image to the next and then remain the same size. Again this behavior would be hard to understand if contamination were involved since a more uniform increase in the affected area would be expected. However, a modified surface structure could conceivably be dependent on the initial presence of defects which would not be equal amongst terraces, and which could determine the boundaries of the domains.

The domains often appear to grow from step edges themselves. This can be seen in Figure 7.6 as well as Figure 7.9, which clearly shows domains originating from step corners, *i.e.* from dislocation intersections. These would be the most highly stressed regions of the surface. The domains may in fact be a stress relief mechanism initiated by tip contact.

The creation of surface damage that is not apparent in AFM topography is consistent with previous results by Hu *et al.* with mica substrates[18]. In that work, a single scan at a high applied load could produce a monolayer deep hole in the mica sample. A single scan at an intermediate load produced no such hole and no apparent topographic effects. Repeated scans over the same area at these intermediate loads were similar to the first until suddenly the surface ruptured and once again a monolayer deep hole was produced on the surface. Multiple scans at lower loads produced no hole at all, even after

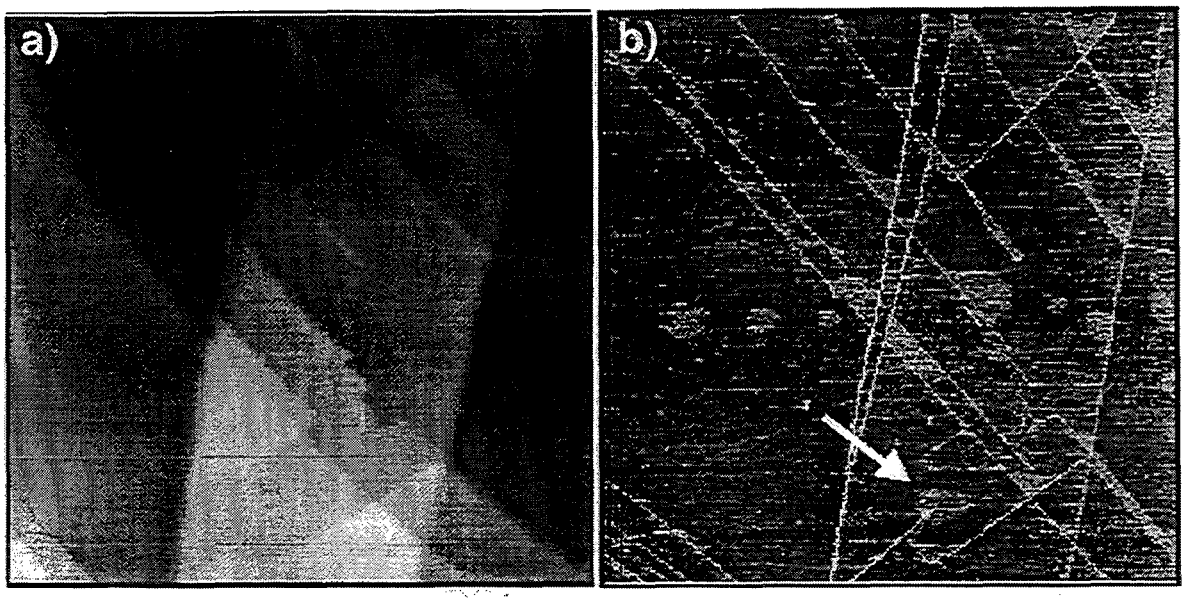

Figure 7.9 (a) Topographic image of a 2.5 × 2.5 μm^2 region of KBr. (b) Subsequent lateral force image. High friction domains grow from step edges as well as corners where steps cross, and sharp kinks in steps (indicated by the arrow). The series of round domains across the middle of the image corresponds to where a series of horizontal line scans were performed prior to acquiring the images.

hundreds of repetitions. This strongly suggests that at the intermediate load regime, defects which were imperceptible in topographic scans must have been accumulating, leading to eventual surface damage on a larger scale. Furthermore, the absence of this effect in the lowest load regime suggests a threshold for defect creation. Mica exhibits strong lateral covalent bonding within a molecular layer, and these layers are bound together by electrostatic forces. To produce a hole, the covalent bonds within a layer must be ruptured. In the present case, we found that domain formation was unavoidable even if the lowest possible loads were utilized. This may not be so surprising since these alkali halides are less strongly bound than the covalently bound species of mica. Furthermore, our tip was relatively sharp, ensuring substantial contact stresses.

Using the JKR contact mechanics theory[19], we can perform rough estimates of the compressive stresses that would be present in the contact zone. These calculations utilize the tip radius measurement described above, and bulk values of the elastic constants for the

tip and sample materials. For example, in the case of KCl with zero externally applied load, we estimate an average contact pressure of 180 MPa, and a maximum contact pressure of 720 MPa at the contact zone center. For KF, the corresponding estimates are 250 MPa average pressure, and 1.0 GPa maximum pressure. The maximum pressures are close to or within the range of the materials' ideal yield strengths (see Table 7.1). Furthermore, short-range adhesion, which is likely in UHV, contributes to high tensile stresses at the contact zone edge[19,20]. Shear stresses due to tip-sample friction will be comparable in magnitude. Surface alteration due to any of these stresses is therefore feasible.

We can also estimate, very roughly, the energy dissipated by friction and compare that to defect formation energies. Using KCl as an example, the average force relaxation observed for a single atomic stick-slip event is 2.0 ± 0.3 nN, measured at zero externally applied load. This corresponds to 5.5 eV of energy dissipated. For lack of a better comparison, the bulk formation energy of a Frenkel defect (vacancy-interstitial pair) is estimated to be in the range of 3.2 - 3.6 eV for a cation interstitial, and 3.4 - 4.4 eV for an anion interstitial[21]. Thus, there is more than enough energy dissipated in a *single* stick-slip event for a Frenkel defect to be created. At zero applied load, the JKR theory predicts a contact area of 16 nm^2, which is about 82 KCl unit cells. If the tip is scanned laterally by one contact radius, enough energy has been dissipated to create 8.3 defects, or roughly 10% of the sites within the contact zone. This is for *one* line scan; an area scan would consist of multiple line scans which could create many defects. Of course, much of the energy could be dissipated through phonon excitation or other ways. Nevertheless, significant defect formation is not out of the question. Therefore, both friction and the substantial stresses present in the contact zone could alter surface and near-surface atoms.

Experimental work by Wilson and Williams[22] demonstrates that surface damage can be assisted by tip-sample contact for the case of an alkali halide. They examined the potassium iodide (KI) surface using AFM while exposing the sample *in-situ* to UV light.

The UV light creates surface and near-surface defects by electronically induced desorption of halogen ions. While the measurements were not carried out in UHV, the relative humidity was kept around 15%, low enough to eliminate most wear effects attributable to humidity. While the UV light created surface damage on its own, regions that were scanned by the tip during UV light exposure showed significantly enhanced damage compared to neighboring regions that were not scanned during UV exposure. The authors therefore concluded that the damage was accelerated by tip-sample contact. It is clear from this example that substantial structural modification was accelerated by tip-sample contact, at a load of around 10 nN.

The theoretical work of Shluger *et al.* concerning the creation of defects by AFM on alkali halides[23,24] is relevant here. These authors simulated the AFM scanning process using a zero-temperature static atomistic technique for a hard, sharp ionic MgO tip scanning a NaCl sample. In their simulations they found that under moderate loading conditions, transfer of ions from sample to tip and creation of Frenkel defects occurred frequently. In their simulation, these processes could be avoided at low loads with an inert tip, but were unavoidable at higher loads and with a less inert (*i.e.* a charged) tip. In addition, these processes frequently reversed, *i.e.* the interstitial atom relaxed back into the vacancy position. However, their simulation involved a very sharp tip (the corner of a $(MgO)_{32}$ cube). More complex behavior would be anticipated for the larger contact area present under experimental conditions. The ease with which defects were created in these simulations suggest that substantial defect formation in actual experimental conditions is plausible.

Interestingly, domain formation was observed only with potassium halide samples, and not with NaCl. In terms of cohesive energy, NaCl is more strongly bound than KCl and KBr, and nearly as strongly bound as KF. Furthermore, the NaCl experiments were carried out with a significantly more blunt tip (~140 nm) than that used for the potassium halide samples, and far more blunt than the single-atom terminated tip used in Shluger *et*

al.'s simulation. Contact stresses are therefore lower with the NaCl experiment. It appears then that the threshold conditions for domain formation were not achieved in the NaCl experiment. It would be interesting to investigate other alkali halides to determine which exhibit this domain formation, and if it is correlated entirely with the binding strength of the material, or if perhaps the chemical identity of the ions is important.

The connected form of the domains on KCl and KBr and their interaction with steps, as well as the uniformity of the friction force on the high friction domains for each material, suggests a uniform nature that involves some kind of lateral interaction within a domain. It is possible that the domains are regions of enhanced surface relaxation, or regions of the surface layer that are slipped or displaced with respect to the layer below. Materials are highly strained in the neighborhood of dislocations. Thus, the electrostatic energy cost of such a rearrangement could be paid for by the reduction of strain which is associated with dislocations. The presence of a surface itself is known to allow relaxation of strain near dislocations[6]. However, it is difficult to propose specific mechanisms since so little is known about defects and dislocation properties at surfaces of ionic materials. At the very least we can state that the domains appear to be structurally, but not chemically distinct from one another, either in their organization or density.

Friction *vs.* load measurements were acquired on all three materials. As we demonstrated in Chapters 5 and 6, friction is proportional to the contact area predicted by continuum mechanics theories, at low loads. However, for the present experiments, no such proportionality was obtained. Furthermore, it was found that the load dependence of friction was generally not reproducible from one measurement to the next. The lack of correlation with continuum mechanics models of elastic contacts suggests that the tip-sample contacts are not elastic in these cases. However, some features of the friction forces were reproducible. An example from the KBr surface is shown in Figure 7.10.

The common feature of all the friction measurements on these materials is that some finite shear force exists even at the lowest loads, and that only a modest increase of friction

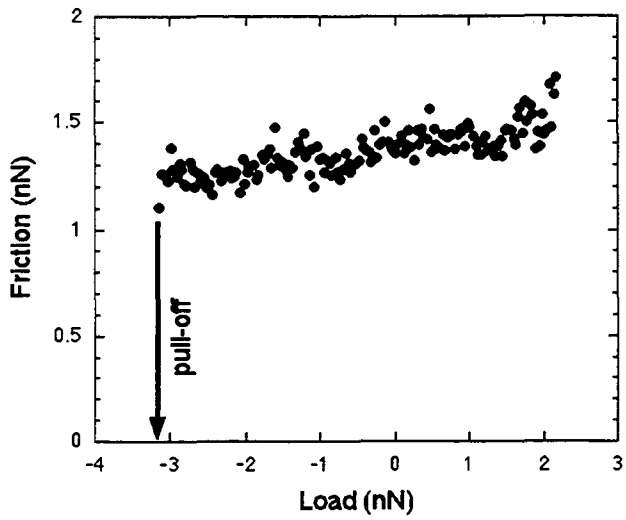

Figure 7.10 Friction *vs.* load plot for KBr within a low load regime. There is a significant finite friction force at the pull-off point, and the friction only has a weak, nearly linear dependence upon load. This is unlike previous measurements of friction *vs.* load on other materials which corresponded to elastic behavior.

with load is observed for the low-load regime. This example shows an apparently linear dependence of friction upon load, although other measurements displayed a small non-linear component. The value of the friction force at the pull-off point varied significantly from one measurement to the next but was typically between 0.3 to 1.5 nN for all three materials. In Chapter 5 we showed that finite friction at low loads in elastic contacts is due to short range adhesion that produces a finite contact area. In this case, however, it may also be related to energy dissipation by surface modification.

Friction *vs.* load measurements can be acquired for higher load ranges and exhibit distinct behavior characteristic of larger scale wear. An example from the KCl surface is shown in Figure 7.11. The experiment begins with the tip out of contact with the sample. At the indicated snap-in point, finite friction is observed which initially increases gradually with load. In this example, above 9 nN the rate of increase becomes substantially greater. Eventually friction actually reduces with increasing load. Upon retraction, significant hysteresis is observed. In Figure 7.11(b) and (c), an image of the scan region reveals the creation of a hole approximately one atomic layer deep , with material piled up at the sides. We believe that the region of steep increase of friction with load is associated with the actual gouging process. The reduction of friction with load at high loads may be associated

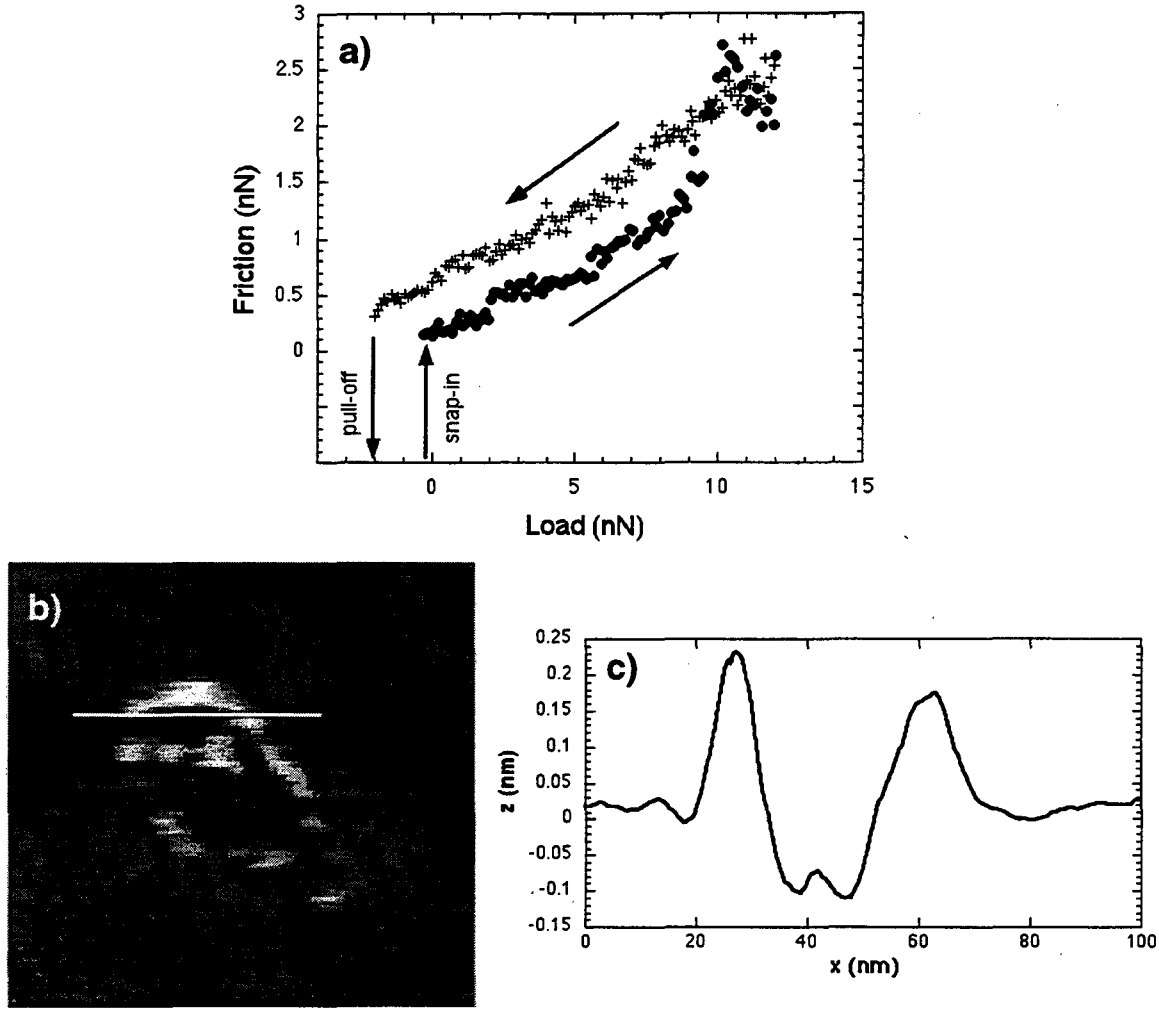

Figure 7.11 (a) Friction *vs.* load plot for KCl for a wide load regime. Friction increases gradually with load until ~5.5 nN where the increase is more rapid. At 9 nN, a sudden increase is followed by a fluctuation of the friction force. Upon retraction, friction does not recover to original values. (b) Topographic image of the region scanned in part (a). A line has been gouged in the sample with material piled up at the sides. (c) A line profile of the gouged area.

with the completion of removal of the first layer of material. These measurements clearly represent a more advanced stage of wear than the domain formation described above.

7.5 Summary

We have measured surface properties of KF, KCl and KBr(001) surfaces in UHV using contact mode AFM. UHV cleavage produces atomically flat terraces with stable monatomic step structures. We have observed a new phenomenon where tip-sample

contact induces higher friction domains.

While the observations are not entirely conclusive regarding the nature of the observed friction domains, the evidence suggests that defect formation is involved. This is an interesting phenomenon to study since it has implications for our understanding of the initial stages of wear and the ability of AFM to measure it. Specifically, these observations indicate that domains of surface or near-surface defects can be created by tip-sample contacts. Furthermore, the presence of defects is manifested in both the magnitude and load dependence of the friction force. This suggests an important and observable relationship between defects and energy dissipation.

Future experiments should attempt to elucidate the mechanism of domain creation and determine their exact structure and properties. This can be accomplished by attempting non-contact force modulation experiments which are capable of resolving individual point defects[9]. This experiment requires high bandwidth fm-demodulation detection circuitry which was not available at the time of these experiments. Furthermore, a wider assortment of alkali halides should be investigated, since domain formation was not observed on NaCl. This may lead to a correlation between the appearance of domains and a specific material property, such as the theoretical yield strength, binding energy, defect formation energy, lattice parameter or some combinations thereof.

Chapter 7 References

[1] A. M. Stoneham, Cryst. Lattice Defects Amorph. Mater. **14,** 173 (1987).

[2] L. Pauling, *The Nature of the Chemical Bond and the Structure of Molecules and Crystals; an Introduction to Modern Structural Chemistry*, 3d ed. (Cornell University Press, Ithaca, N.Y., 1960).

[3] M. P. Tosi, in *Solid State Physics*; *Vol. 16*, edited by F. Seitz and D. Turnbull (Academic Press, New York, 1964).

[4] G. Simmons and H. Wang, *Single Crystal Elastic Constants and Calculated Aggregate Properties: a Handbook*, 2d ed. (M.I.T. Press, Cambridge, Mass., 1971).

[5] A. Kelly, *Strong Solids*, 2nd ed. (Oxford University Press, London, 1973).

[6] M. T. Sprackling, *The Plastic Deformation of Simple Ionic Crystals* (Academic Press, London, 1976).

[7] N. Agraït, G. Rubio, and S. Vieira, Phys. Rev. Lett. **74,** 3995 (1995).

[8] J. B. Pethica and A. P. Sutton, J. Vac. Sci. Technol. A **6,** 2494 (1988).

[9] F. J. Giessibl, Science **267,** 68 (1995).

[10] M. Bammerlin, R. Lüthi, E. Meyer, A. Baratoff, J. Lü, M. Guggisberg, C. Gerber, L. Howald, H. Haefke, and H.-J. Güntherodt, Probe Micrscopy **1,** 3 (1997).

[11] Optovac, North Brookfield, MA.

[12] Prof. M. DeLong, Dept. of Physics, University of Utah.

[13] Sharpened Microlever type E, Park Scientific Instruments, Sunnyvale, CA.

[14] M. Luna, N. A. Melman, F. Rieutord, Q. Dai, D. F. Ogletree, and M. Salmeron, J. Phys. Chem. **submitted** (1997).

[15] R. Lüthi, E. Meyer, H. Haefke, L. Howald, W. Gutmannsbauer, M. Guggisberg, M. Bammerlin, and H.-J. Güntherodt, Surf. Sci. **338,** 247 (1995).

[16] C. D. Frisbie, L. F. Rozsnyai, A. Noy, M. S. Wrighton, and C. M. Lieber, Science **265,** 2071 (1994).

[17] J. N. Israelachvili, *Intermolecular and Surface Forces*, 2nd ed. (Academic Press London, London, 1992).

[18] J. Hu, X.-D. Xiao, D. F. Ogletree, and M. Salmeron, Surf. Sci. **327,** 358 (1995).

[19] K. L. Johnson, K. Kendall, and A. D. Roberts, Proc. Roy. Soc. Lond. A **324,** 301 (1971).

[20] D. Maugis, J. Colloid Interface Sci. **150,** 243 (1992).

[21] D. K. Rowell and M. J. L. Sangster, J. Phys. C (Sol. State Phys.) **14,** 2909 (1981).

[22] R. M. Wilson and R. T. Williams, Nucl. Instrum. Methods Phys. Res. **101,** 122 (1995).

[23] A. L. Shluger, R. T. Williams, and A. L. Rohl, Surf. Sci. **343,** 273 (1995).

[24] A. L. Shluger, A. L. Rohl, R. T. Williams, and R. M. Wilson, Phys. Rev. B **52,** 11398 (1995).

8. Concluding Discussion

This work presented in this thesis began just 7 years after the invention of the AFM. Only a handful of other UHV AFM's existed and few results pertaining to nanotribology had been obtained. The task at hand has been to build both the experimental techniques and the physical understanding of this new field from the ground up. The main accomplishment of this thesis is the demonstration that AFM is capable of obtaining fundamental, quantitative knowledge regarding contact, friction and adhesion at the atomic scale.

Before we summarize the conclusions in detail, we first turn our attention to the greater challenge of how to utilize this newfound atomic scale knowledge at practical length scales.

8.1 Macroscopic Friction: Is There a Connection?

We began this thesis with the statement of Amonton's Law of friction:

$$F_f = \mu \cdot L \tag{8.1}$$

but later showed that for elastic single asperities,

$$F_f = \tau \cdot A \tag{8.2}$$

and since, according to all the contact mechanics theories, A is not linearly proportional to L, these two laws appear to be incompatible. However, they describe different situations. Macroscopic contacts involve rough surfaces with multiple asperities, not a single asperity, and furthermore the interactions may not be completely elastic. If somehow the total contact area is in fact proportional to load, then these two equations become consistent. Can such a connection between these two laws be established? In other words, can we use

our knowledge about how single asperities behave to understand the properties of a collection of asperities?

Bowden and Tabor [1,2] suggested that during contact, asperities *plastically* deform and adhere to one another. The hardness, H, of a material generally determines the resulting plastically deformed contact area at a given load:

$$A = L/H \quad . \tag{8.3}$$

During sliding, these adhering contacts will be sheared. The friction force required to shear the junctions is proportional to the contact size, as in equation (8.2),

$$F_f = \tau \cdot A = \frac{\tau}{H} \cdot L \tag{8.4}$$

where τ here represents the critical shear strength of the adhered junction. From equation (8.4) we regain Amonton's Law of friction and have a form for the friction coefficient:

$$\mu = \tau/H \quad , \tag{8.5}$$

the ratio of the asperity shear strength to the hardness.

Archard pointed out a fundamental objection to this approach[3]. We know that Amonton's Law can hold for surfaces that are rubbed together not just once, but millions of times. If irreversible plastic deformation is taking place at each pass, the expected wear rate would far exceed that which is observed.

Greenwood and Williamson[4] (GW) considered the sum of *elastic* deformations for a collection of asperities that experience a normal load from a flat rigid plane. The statistics of asperity distributions lead to some very important conclusions. Figure 8.1 depicts a surface that resembles one that might be encountered in an engineering application. Note that the vertical scale is roughly 100 times greater than the horizontal scale. GW's approach is to assume that there is a Gaussian distribution of asperity heights (which turns out to be true for many actual surfaces) and that the asperity radii are all equal (which is a fair approximation in many cases as asperity radii are often distributed about some mean

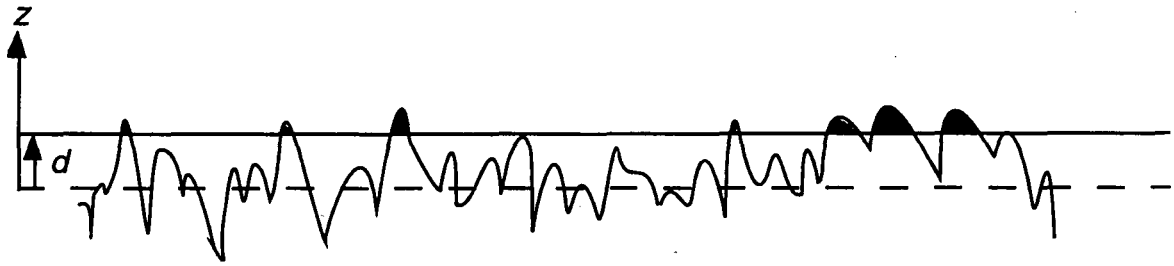

Figure 8.1 Sketch of a rough surface, based upon profilometry data like that shown in Greenwood and Williamson[4], where the vertical scale is roughly 100 times greater than the horizontal scale. *d* represents the distance of approach of an ideal flat rigid surface toward the rough surface.

value). GW uses Hertzian mechanics to calculate the contact area for individual asperities. We reproduce the essentials of the GW model here as it is quite straightforward.

From Figure 8.1, if the separation between the plane and the mean asperity height is *d*, then any asperity of height *z*, above the height *d*, will be compressed by $\delta=z-d$. For the Hertz model, the relations between contact area A_1, load L_1 and elastic deformation δ for one asperity of radius *R* are given by:

$$A_1 = \pi R \delta \tag{8.6}$$

$$L_1 = K R^{1/2} \delta^{3/2} \tag{8.7}$$

where *K* is the usual elastic parameter defined in Chapter 5. The total number of asperities is *N*. Let the asperity height distribution be specified by the function $\phi(z)$, such that there are $N\phi(z)dz$ asperities between *z* and $z+dz$. Then the total area of contact and load are obtained by summing the contributions of each contact from *d* upward:

$$A = N\pi R \int_d^\infty (z-d)\cdot\phi(z)dz \tag{8.8}$$

$$L = NKR^{1/2} \int_d^\infty (z-d)^{3/2}\cdot\phi(z)dz \quad . \tag{8.9}$$

For an exponential asperity height distribution $\phi(z) = e^{-\lambda z}$, the above integrals can be solved and the result is that the contact area is *directly proportional* to the load. Using a more realistic Gaussian height distribution $\phi(z) = \frac{1}{\sigma\sqrt{2\pi}} e^{-z^2/2\sigma^2}$, we can divide the area by

the load and make the integrals non-dimensional, giving:

$$\frac{A}{L} = \frac{\pi R^{1/2}}{K\sigma^{1/2}} \cdot \frac{\int_a^\infty (x-a)e^{-x^2}dx}{\int_a^\infty (x-a)^{3/2}e^{-x^2}dx} = \frac{\pi R^{1/2}}{K\sigma^{1/2}} \cdot I \tag{8.10}$$

where the lower limit of the integral $a=d/\sigma$. Numerical integration reveals that the ratio of the integrals I only varies from about 1.8 to 1.2 over four orders of magnitude of the load (see Figure 8.2), and thus for a Gaussian height distribution, contact area is very nearly proportional to load. This is true even though the individual asperities' contact area increases as $L^{2/3}$. The reason for this is that the main effect of increasing the load is not just to increase the area of the contacts that are already established, but also to produce many more new contacts which have lower heights. As long as an increasing number of new contacts are being formed, the sum total of the area increases in a nearly linear fashion. Experiments have found good agreement with the GW approach for a variety of systems[5].

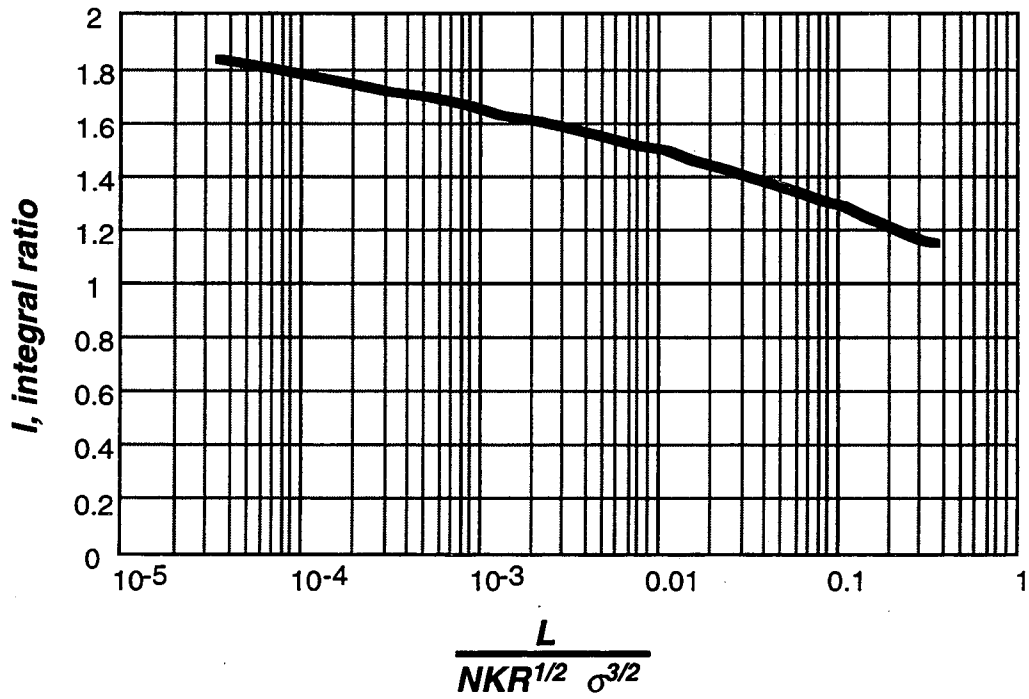

Figure 8.2 The ratio of the integrals, I, in equation (8.10), plotted *vs.* non-dimensional load units on a logarithmic scale. I is nearly constant over four orders of magnitude in the load variable.

Using Hertzian analysis neglects adhesion, so the GW theory has been refined to take into account adhesion between the asperities in both the JKR[6] and DMT[7] regimes.

The GW approach also allows one to calculate the fraction of asperities that will undergo plastic deformation, *i.e.* those for which the pressure has exceed a critical value - the yield stress. Although the *number* of plastically deformed asperities will increase with load, so too will the *total* number of asperities. It turns out that the *fraction* of plastically deformed asperities is independent of load, and depends only upon the elastic modulus E^*, the hardness H, the asperity radius R, and the standard deviation of the asperity height distribution σ. From this, GW defines a non-dimensional quantity called the *plasticity index*, ψ:

$$\psi = \frac{E^*}{H}\sqrt{\frac{\sigma}{R}} \quad . \tag{8.11}$$

ψ=1 roughly corresponds to 1% of the contact area being plastically deformed; the larger ψ, the greater the fraction of the contact that involves inelastic deformations, independent of the load. For ψ<0.6, the contact will be almost entirely elastic, for ψ>1, plastic flow will occur even at the lightest loads. Therefore, material parameters (E^* and H) and surface topography parameters (R and σ) will determine the amount of elasticity in the contact. For example, Greenwood and Williamson measured for a steel roller bearing that σ=0.024 μm and R=150 μm, from which ψ=0.25, well within the elastic regime. For many materials, the fraction of plastically deformed contacts can be rather small. Therefore, knowledge of the frictional properties of elastically deformed single asperities is indeed useful.

In fact, for a mostly elastic contact, we can derive a form for the friction coefficient within the framework of the GW theory. We assume that equation (8.2) holds, *i.e.* that for each asperity, the friction force is proportional to the contact area. Therefore the total friction force will be proportional to the total contact area:

$$F_f = \tau \cdot A = \tau \cdot L \cdot (A/L) = L \cdot \left[\frac{\pi \tau R^{1/2}}{K\sigma^{1/2}} \cdot I \right] \quad . \tag{8.12}$$

If we assume the reasonable value of 1.5 for I, then we have a form for the macroscopic friction coefficient in terms of the single asperity shear strength:

$$\mu = 1.5\pi \frac{\tau}{K}\sqrt{\frac{R}{\sigma}} \quad . \tag{8.13}$$

Therefore, if we knew τ from an AFM measurement, we could predict the friction coefficient for a pair of materials with a given K, R and σ, if the plasticity index indicated we were in a mostly elastic regime. For example, a moderately smooth surface may have $\sqrt{R/\sigma} = 200$.[8] For the Si_3N_4-mica interface we measured in Chapter 5, $\tau/K = 8.9\times10^{-4}$. This would give μ=0.8 .[9]

This is nonetheless a very simplified model. Utilizing it for understanding friction requires some additional considerations. Johnson and co-workers[10] have extended the GW analysis to include frictional sliding. The plasticity index ψ is still a meaningful parameter, but instead of using the hardness H, the asperity's strength is determined by a quantity called the *asperity shakedown pressure,* p_s, which depends upon asperity shape, the yield strength, and the amount of friction between contacting asperities. p_s represents the stress beyond which a sheared asperity will yield, due either to the normal compression or frictional shearing. Thus, the important parameter becomes the "plasticity index in repeated sliding", given by

$$\psi_s = \frac{E^*}{p_s}\sqrt{\frac{\sigma}{R}} \quad . \tag{8.14}$$

Furthermore, the total load does matter for determining the behavior. At very high loads, a large amount of plastic deformation can repeatedly occur. However, for a given value of ψ_s, there is a threshold load below which the interaction will be mostly elastic. Furthermore, many surfaces that initially involve significant plastic deformation will progress toward an elastic steady state because of the increase in asperity size, R, due to the wear. Furthermore, shearing off of high asperities leads to a reduction of the asperity height distribution, σ. From equation (8.14), an increase in R and a decrease in σ means a reduction in ψ_s and hence a more elastic state. More generally, repeated sliding causes

blunting and flattening of the asperities, strain hardening and residual stresses due to plastic deformation, all of which tend to lead toward an elastic steady state. This is called the "shakedown" process and has been observed experimentally.

The threshold load for elastic steady state behavior depends upon the surface topography parameters as well as p_s. Therefore, the asperity shakedown pressure is a critical parameter to evaluate. To calculate p_s, Johnson and co-workers, as well as others, have assumed that the frictional force experienced by the single asperity is given by Amonton's Law, equation (8.1). In light of the results presented here, it would be worthwhile to assume instead that equation (8.2) determines the friction force for a single asperity. This would require knowing τ for the materials of interest. Thus, AFM measurements could provide a critical contribution here. Although AFM tips are much sharper than typical surface asperities, it is possible to use blunter tips with etched wires or attached particles. Furthermore, the fact that continuum mechanics appears to apply even at the nanometer scale may imply that shear strength measurements at the nanometer scale can be extrapolated to larger length scales. This hypothesis is worthy of further investigation.

Therefore, in principle, AFM experiments can provide measurements of τ for a range of materials, sliding conditions and asperity sizes (if indeed a size dependence exists), and from this provide the missing piece of information to allow for prediction of frictional behavior at the macroscopic scale for a wide range of practical situations. The interfacial energy γ could also be important for strongly adhering materials; AFM can measure this quantity as well.

8.2 Summary of Results

We have attempted to understand and quantify the force interactions taking place at nanometer sized contacts. The major accomplishments of the thesis are listed below.

⇒ ***Development of instrumentation for studies of nanotribology.*** A novel home-built ultrahigh vacuum atomic force microscope was implemented. The

instrument allows variable temperature operation, and surface science analysis of sample properties.

⇒ ***Development of techniques for instrument calibration, and tip shape determination.*** We conceived and implemented an experimental calibration method which provides the relative lateral to normal force sensitivity of the system. The method uses the expected geometrical coupling of forces on a tilted surface to determine the sensitivity ratio. The faceted $SrTiO_3(305)$ surface is ideal for this purpose as it provides two well-defined atomically flat planes for the experiment. Empirical calibration is important since there are several uncertain factors which determine the force constants for microfabricated cantilevers. The $SrTiO_3(305)$ sample also allows for acquisition of a cross-sectional tip profile by scanning over the sharp edges where the facets meet.

⇒ ***Demonstration of the generality of atomic-scale stick-slip phenomena, its relation to the origin of "atomic resolution" in topographic images, and consequences for the correct definition of friction.*** Atomic-scale stick-slip friction forces with lattice periodicity were observed with a number of samples and appear to be a general phenomenon of nanometer sized contacts. The apparent topography in atomic-scale images is a consequence of stick-slip motion of the tip in the longitudinal direction. The lateral force amplitude during stick-slip depends upon the contact stiffness and thus varies with load. Therefore, if stick-slip motion is taking place, one must carefully measure the maximum friction force *i.e.* the force at which slip occurs, to obtain a correct measurement of the friction force F_f.

⇒ ***Verification of continuum mechanics at the nanometer scale; proof of the elastic single asperity friction law: $F_f = \tau A$.*** We have observed that Amonton's Law is not valid for an elastic single asperity contact. Rather, using mica(0001) as a substrate in UHV, friction varied with load in proportion to the

area of contact predicted by the JKR theory of elastic adhesive contacts. The area of contact depends upon the tip shape and size, therefore nanotribology studies with AFM *must* characterize the tip shape.

⇒ ***Measurement of fundamental friction and adhesion parameters with AFM.*** Applying the JKR theory allows the determination of the interfacial shear strength τ and the interfacial adhesion energy γ. These should be regarded respectively as the fundamental friction and adhesion parameters of the interface.

⇒ ***Example of a relation between adhesion and friction.*** The shear strength and adhesion energy between Si_3N_4 tips and mica was constant, whereas they varied for Pt-coated tips. The variation was most likely due to a chemical change of the tip surface, possibly from adsorption of potassium ions from the mica surface to the tip. This resulted in an order of magnitude drop in the adhesion energy and a corresponding reduction of the shear strength by a factor of ~4. The relation between adhesion and friction is not understood or explained by any current theory. These experiments provided a set of measurements relating γ and τ for a single system, for which we observe $\tau \propto \gamma^{0.44\pm0.10}$.

⇒ ***Development of the technique and measurements of lateral contact stiffness.*** We have demonstrated that the lateral stiffness of tip-sample contacts can be sensitively measured with AFM. The lateral stiffness provides a measurement that is proportional to the contact radius and the combined shear modulus of the materials. A comparison between friction and stiffness measurements thus allows, experimentally, determination of the relation between friction and contact area. In this fashion we observe that friction is directly proportional to contact area with a load-independent shear strength for three systems: Si_3N_4 tips and mica in air, Si_3N_4 tips and mica in UHV, and Si_3N_4 tips and NaCl(001) in UHV. Humid atmosphere causes water condensation about the contact which in turn changes the surface forces and the resulting tip-sample contact

area.

⇒ ***Indication that bulk elastic constants may not be accurate for nm-size contacts at surfaces.*** Applying contact mechanics models to the stiffness measurement reveals that the apparent shear modulus is much lower than the bulk value for all three systems. This may be due to actual weakening of the elastic response of the materials near their surface, or additionally that refined contact mechanics theories should be utilized for quantitative analysis.

⇒ ***Observed formation of friction domains on potassium halide substrates which may be indicative of atomic-scale wear.*** Frictional properties of KF(001), KCl(001) and KBr(001) samples were studied in UHV with a Si_3N_4 tip. UHV cleavage produces atomically flat terraces with mostly monatomic steps. We observe consistently that tip-sample contact creates domains on the terraces which exhibit higher friction. The domain properties, namely their lateral structure, topographic height, and friction contrast, vary systematically with each type of material. Furthermore, friction varies with load in a fashion that is inconsistent with previous observations with elastic contacts. The most likely hypothesis for this unexpected and unique behavior is that tip-sample contact modifies the surface by rearranging atoms at or near the surface. Further study should attempt to elucidate what appears to be an atomic-scale wear mechanism.

8.3 Future Directions

There are many outstanding issues in the field of nanotribology in general, and several problems which are worthy of attention for this project.

Instrumental issues worth addressing include developing an empirical calibration method for the normal force constant of cantilevers. Also, since the wedge calibration technique works better for lower effective friction coefficients, experiments to determine the optimum experimental environment (low humidity, high humidity, UHV) for the calibration measurements should be carried out. We often encounter blunt tips which

cannot be used with the $SrTiO_3(305)$ sample because of the facet size limit. It would be worthwhile investigating alternative sloped surfaces that can be used with blunt tips.

Further attempts to measure and/or control the tip structure should be carried out. TEM measurements can be used for three-dimensional imaging of the tip apex. *In-situ* deposition of tip coatings, or tip treatments such as sputtering or plasma etching should be attempted to take full advantage of the vacuum environment to ensure a well-determined tip chemistry.

Further work clarifying the applicability of continuum mechanics would be useful. Although the JKR model seems to describe the contact area behavior very well in UHV for a variety of systems, the newer continuum models should be considered. The effect of sample anisotropy, lateral forces, and other corrections may be significant in some cases. Complementary friction and stiffness measurements on well chosen samples are the way to address this. Using adsorbates, molecular layers, or different crystal faces of the same material to change the surface energy would be a way to access a variety of values of μ_T, the adhesion force range parameter defined in Chapter 5. Interesting effects such as the adhesion and shear strength reduction described in Chapter 5 call for related theoretical efforts to help interpret and explain such behavior.

There has not been experimental verification yet that bulk values of elastic constants apply at the nanometer scale for surfaces, and our results suggest that in fact they may not. A force-controlled instrument could measure normal stiffness, to access the Young's modulus E, which could be compared with bulk values, along with G as derived from lateral stiffness measurements. As well, theoretical modeling could help guide the way to resolve this uncertainty. This is important, as uncertainty in the elastic constants could be a barrier to obtaining accurate shear strength measurements.

Contact conductance is also related to contact area, and so measurements with conducting tips and samples are worth of further pursuit. In this respect, it is important to continue work recently begun on this project using Pt(111) and doped diamond substrates

with conductive W_2C tips. Conducting tips offer the further advantage of allowing STM measurements. Furthermore, metal single crystals allow a wide array of adsorbate structures to be explored. The adhesion and friction properties of a series of adsorbate structures could help clarify the relation between adhesion and friction and the role that chemistry and structure plays in determining them. Such studies are also ideally suited for theoretical modeling because the adsorbate structures are well characterized. It would also be interesting to study how friction and adhesion vary due to changes with temperature. For example, vibrational or structural phase transitions of adsorbates could be studied to take advantage of the variable temperature capability of our instrument. Overall, this represents an exciting future direction.

Chapter 8 References

[1] F. P. Bowden and D. Tabor, *Friction and Lubrication of Solids: Part I* (Oxford University Press, 1950).

[2] F. P. Bowden and D. Tabor, *Friction and Lubrication of Solids: Part II* (Oxford University Press, 1964).

[3] J. F. Archard, J. Appl. Phys. **32,** 1420 (1961).

[4] J. A. Greenwood and J. B. P. Williamson, Proc. Roy. Soc. Lond. A **295,** 300 (1966).

[5] Z. Handzel-Powierza, T. Klimczak, and A. Polijaniuk, Wear **154,** 115 (1992).

[6] K. N. G. Fuller and D. Tabor, Proc. Roy. Soc. Lond. A **345,** 327 (1975).

[7] D. Maugis, J. Adhes. Sci. Technol. **10,** 161 (1996).

[8] K. L. Johnson, in *Fundamentals of Friction*, edited by I. L. Singer and H. M. Pollock (Kluwer, Dordrecht, 1992), p. 227.

[9] This is a oversimplified use of the model for this specific example. The GW model assumes the flat plane is rigid and the asperities deform. Here, mica is flat but less stiff than silicon nitride. A "rough" mica surface is complicated to imagine because of its structural anisotropy. We carry out the calculation merely as an example.

[10] A. Kapoor, J. A. Williams, and K. L. Johnson, Wear **175,** 81 (1994).

Ernest Orlando Lawrence Berkeley National Laboratory
One Cyclotron Road | Berkeley, California 94720

Prepared for the U.S. Department of Energy under Contract No. DE-AC03-76SF00098